DIRECT SIMULATION OF PARTICLE-LADEN VISCOUS FLOWS AND THEIR APPLICATIONS

by

Hui Gao

A dissertation submitted to the Faculty of the University of Delaware in partial fulfillment of the requirements for the degree of Doctor of Philosophy in Mechanical Engineering

Spring 2014

ProQuest LLC.
789 East Eisenhower Parkway
P.O. Box 1346
Ann Arbor, MI 48106 - 1346

DIRECT SIMULATION OF PARTICLE-LADEN VISCOUS FLOWS AND THEIR APPLICATIONS

by

Hui Gao

Approved: _____

Suresh G. Advani, Ph.D.
Chair of the Department of Mechanical Engineering

Approved: _____

Babatunde A. Ogunnaike, Ph.D.
Dean of the College of Engineering

Approved: _____

James G. Richards, Ph.D.
Vice Provost for Graduate and Professional Education

I certify that I have read this dissertation and that in my opinion it meets the academic and professional standard required by the University as a dissertation for the degree of Doctor of Philosophy.

Signed: _____

Lian-Ping Wang, Ph.D.
Professor in charge of dissertation

I certify that I have read this dissertation and that in my opinion it meets the academic and professional standard required by the University as a dissertation for the degree of Doctor of Philosophy.

Signed: _____

Suresh G. Advani, Ph.D.
Member of dissertation committee

I certify that I have read this dissertation and that in my opinion it meets the academic and professional standard required by the University as a dissertation for the degree of Doctor of Philosophy.

Signed: _____

Yan Jin, Ph.D.
Member of dissertation committee

I certify that I have read this dissertation and that in my opinion it meets the academic and professional standard required by the University as a dissertation for the degree of Doctor of Philosophy.

Signed: _____

Kausik Sarkar, Ph.D.
Member of dissertation committee

ACKNOWLEDGEMENTS

I would like to express my most sincere gratitude to my advisor, Dr. Lian-Ping Wang, for his understanding nature, infinite patience, and strong support over the past six years. Dr. Wang literally led me through every step of the research process, from literature survey to code development, from data analysis to paper writing and to work presentation. It is under his knowledgeable guidance and rigorous academic training that I gradually developed my own interest and confidence in scientific research, especially in the area of computational fluid dynamics. During the course of my graduate studies, there were numerous times he enlightened me on my subject, corrected my doubts, and inspired me with new ideas. His indefatigable pursuit of scholarship and optimistic attitude towards challenges have been, and will always be, the greatest motivation for me in my path of professional development.

I also want to extend my sincere thanks to Dr. Suresh Advani, Dr. Yan Jin, and Dr. Kausik Sarkar for serving on my committee, reviewing my dissertation, and offering constructive comments and suggestions.

Through the course of my thesis work, I have received numerous help from many of my colleagues and friends, especially from Dr. Bogdan Rosa, from whom I learned a lot ranging from numerical algorithms to the cutting-edge software techniques. His unflinching willingness to help is greatly appreciated. Special thanks to Dr. Hossein Parishani, Ms. Xiaoyan Shi, Ms. Queming Qiu, Dr. Orlando Ayala, Dr. Jie Han, and Dr. Volha Lazouskaya for many stimulating conversations and kind assistance.

I would like to acknowldege the financial support from the National Science Foundation and US Department of Agriculture. I am also grateful for access to computional resources at the National Center for Atmospheric Research (NCAR), and for

the assistance from the staff of Computational and Information Systems Laboratory at NCAR on parallem computing.

Finally, I am deeply grateful to my family, upon whose constant support and encouragement I have relied throughout the years. I owe my loving thanks to my wife, Dr. Hui Li, and my daughter, Yunhan, whose love and support made this effort manageable and worthwhile.

TABLE OF CONTENTS

LIST OF TABLES

LIST OF FIGURES

ABSTRACT

In this dissertation, we conduct direct simulations of particle-laden viscous flows with dual objectives: the first is the implementation and validation of the mesoscopic lattice Boltzmann (LB) approach for particle-laden viscous flows, and the second concerns two specific applications of this approach, namely, turbulent suspension flow and microscale porous media flow with colloid deposition and migration.

The LB approach solves continuum-fluid flows indirectly by discretizing the Boltzmann equation using a minimum set of discrete velocities. It reproduces the incompressible Navier-Stokes equation in the limit of low effective Mach number of the system. Most previous validations of the LB approach concern relatively simple viscous flows. In this study, we apply the LB approach to more complex problems with curved fluid-solid interfaces, and compare directly with a novel hybrid Navier-Stokes based approach (Physalis) developed by Professor Prosperetti's group at Johns Hopkins. We have demonstrated systematically the accuracy and parallel efficiency of the LB approach and showed that the LB approach is particularly effective for simulating fluid-flow systems containing a large number of spherical solid particles.

The study of turbulent suspension flow was motivated by the open question concerning the impact of the presence of finite-size inertial particles on the turbulent carrier flow, and the interaction between the particles. For this purpose, a particle-resolved simulation method was developed based on the multiple-relaxation-time lattice Boltzmann equation (MRT-LBE). The no-slip boundary condition on the moving particle boundaries was handled by a second-order interpolated bounce-back scheme. The mesoscopic particle distribution functions at a newly converted fluid lattice node were constructed by the equilibrium distribution with non-equilibrium correction. An elastic repulsive force model was utilized to prevent particle-particle overlap. The code was

parallelized with MPI and was found to be computationally efficient with an excellent scalability.

The method is first validated using unsteady sedimentation of a single particle and a multi-particle random suspension. It is then applied to a decaying isotropic turbulence laden with particles of Kolmogorov to Taylor microscale size. At a given particle volume fraction, the dynamics of the particle-laden flow is found to depend mainly on the effective particle surface area and particle Stokes number. The presence of finite-size particles enhances viscous dissipation at small scales while reducing kinetic energy at large scales. This is in accordance with related studies. However, the normalized pivot wavenumber is found to depend not only on the particle size, but also on the relative ratio of particle size to flow dissipation range scales as well as the particle-to-fluid density ratio. Moreover, strong modulation is observed within half particle radius near particle surface, and local profiles are are found to be self similar with proper normalization.

The second application pertains to colloid and colloid-facilitated contaminant transport and retention in soil porous media. Specifically, we intend to quantify the colloid deposition mechanism under unfavorable conditions where both the colloid surface and grain surface are negatively charged. This application consists of two components, the simulation of microscopic viscous flow in a three-dimensional porous channel, and the transport of sub-micron colloids in this model geometry. We apply simultaneously the MRT-LBE method and the hybrid Physalis method. The latter handles the no-slip boundary condition by coupling an analytical Stokes expansion valid in a narrow but finite region near a particle surface with the numerical solution outside the particle. The mesoscopic LBM is shown to be superior to the hybrid macroscopic approach, especially when there exist multiple grain-grain and grain-wall contact points.

Colloid transport and deposition were then simulated by a Lagrangian tracking approach, under the combined influence of hydrodynamic forces, Brownian force, and physicochemical forces. With the given solution ionic strength and physicochemical

condition, capture of colloids by the secondary energy minimum (SEM) were demonstrated. The local hydrodynamic retardation is shown to reduce the ability for colloids to move into the SEM, but does not prevent this to occur. Before being captured by the SEM, colloid trajectories are shown to depend on local porosity, flow convergence, and contact points. After capture, the interaction between particle inertia, DLVO forces and local hydrodynamic interaction play a prominent role. These results provide a new level of details on colloid transport and retention that are not easily achievable in physical experiments.

Chapter 1

INTRODUCTION

1.1 Background and Motivation

1.1.1 Particle Suspension in Turbulence

Turbulent flows laden with solid particles, small droplets, and gas microbubbles are ubiquitous in engineering, biological and environmental applications. Examples include fluidized bed reactors, spray atomization, pneumatic conveyors, bubble columns, plankton contact dynamics in ocean water, transport of blood corpuscles in the human body, sediment transport, warm rain process, volcanic ash eruptions, dust storms, and sea sprays. In these applications, particles are usually suspended in a turbulent carrier fluid. The interactions between the dispersed and the carrier fluid phases impact the dynamics of suspended particles (e.g., dispersion, deposition rate, collision rate, settling velocity) and the bulk properties of the multiphase flow (e.g., wall or surface drag, turbulence intensity and structures). Understanding turbulent particle-laden flows can help us better design engineering devices such as coal combustors and better predict natural phenomena such as warm rain and hurricane.

A turbulent particle-laden flow system is more complicated than its single-phase counterpart owing to a broader range of length and time scales and the additional parameters associated with the dispersed phase (Balachandar and Eaton, 2010). To this end, many experimental investgations have been performed to understand turbulence-particle interactions by means of using a reduced set of parameters in the system, especially for the turbulence modifications by particles. Gore and Crowe (1989) reviewed a large number of particle-laden turbulent jet and pipe experiments. They showed that the ratio of the particle diameter to the turbulent integral length scale qualitatively determined the type of turbulence modification, but its quantitative level could

depend on other factors, including particle Stokes number, particle Reynolds number, and mass loading. Paris and Eaton (2001) studied fully developed channel flow laden with copper and glass particles with size near Kolmolgorov length. Their experimental results indicated that turbulence attenuation increased monotonically with particle mass loading. More recently, Eaton (2006) and Tanaka and Eaton (2008) integrated previous particle-laden experiments to generalize the turbulence modification. Eaton (2006) reported that particles with Stokes number of $O(1) \sim O(10)$ led to attenuation of turbulent kinetic energy (TKE), whereas particles with larger Stokes number caused TKE augmentation induced by unsteady particle wakes. Further analysis by Tanaka and Eaton (2008) suggested that physical mechanisms for turbulence augmentation or attenuation could be depicted by a novel non-dimensional number Pa integrating particle Stokes number, Reynolds number based on a representative large scale of turbulence, and the ratio between the Kolmogorov length scale and the representative turbulent large scale. When Pa was small ($Pa < 10^3$), turbulence augmentation occurred due to preferential particle concentration around intense vortical structures. In the intermediate range of $10^3 < Pa < 10^5$, turbulence was attenuated by the presence of particles. Further increases in Pa would again lead to turbulence augmentation as a result of superposition of turbulent wakes.

Although many experimental studies have been conducted, it is still difficult to address clearly the physics of turbulence-particle interactions. For a turbulent flow laden with non-deforming spherical particles, the length scales range from the particle diameter (d_p) and flow Kolmogorov length (η) to the integral length scale (L). When d_p/η is small and the volume fraction (ϕ) of the dispersed phase is low, the response of a particle to the local flow can be well described by an equation of motion (Maxey and Riley, 1983), making it unnecessary to resolve the disturbance flow on the scale of the particle size. Most theoretical understanding for turbulent particle-laden flows has been developed based on these assumptions. Computationally, the condition of $d_p/\eta < 1$ partially justifies the use of point-particle based simulation (Wang *et al.*, 2009).

Over the past two decades, the point-particle model has been employed to discover and quantify a number of important phenomena in turbulent particle-laden flows, including preferential concentration (Squires and Eaton, 1991; Wang and Maxey, 1993), turbulence modulation by inertial particles (Squires and Eaton, 1990; Elghobashi and Truesdell, 1993), particle deposition rate (McLaughlin, 1989; Swailes and Reeks, 1994), and turbulent collision rate of inertial particles (Sundaram and Collins, 1997; Zhou *et al.*, 2001; Ayala *et al.*, 2007; Wang *et al.*, 2009; Jin *et al.*, 2010). However, even for the relative simple case of small particle size, the interactions between the dispersed phase and the carrier phase are difficult to describe in general. For heavy particles whose density (ρ_p) is much larger than the fluid density (ρ_f), the ratio of the particle inertial response time (τ_p) to the flow Kolmogorov time (τ_k), known as the Stokes number, can be expressed as $St \equiv \tau_p/\tau_k = \frac{1}{18}\left(d_p/\eta\right)^2 \rho_p/\rho_f$, implying that particles could interact with a range of flow time scales depending on the relative magnitudes of the density and size ratios.

Many applications entail particle sizes comparable to, or larger than the flow Kolmogorov length (Burton and Eaton, 2005) so that the scales contained in the disturbace flows overlap with the scales of motion in the carrier turbulence. In this situation, the point-particle model is no longer a valid description and the finite-size effect of the dispersed phase must be resolved together with the carrier fluid turbulence. Currently, the only rigorous method is to numerically resolve the disturbance flows around particles, known as the particle-resolved simulation. Due to the requirement of explicit implementation of the no-slip boundary condition on the surface of each particle, the particle-resolved simulation is computationally more demanding than the point-particle model. For this reason, particle-resolved simulation has so far been limited to either low flow Reynolds numbers or to large particle size relative to the Kolmogorov scale.

Several computational methods have been developed to perform particle-resolved simulation. Finite element methods (Hu, 1996; Johnson and Tezduyar, 1999; Hu *et al.*, 2001) employ body-fitted mesh to implement solid particle boundary conditions. The frequent mesh regeneration due to the geometry change as a result of particle motion

is computationally expensive, especially in three-dimensional simulations. Therefore, methods using a fixed and structured grid have received more attention in recent years. The fictitious domain or direct forcing method (Patankar *et al.*, 2000; Glowinski *et al.*, 2001; Wu *et al.*, 2011; Shao *et al.*, 2012) applies a field of Lagrange multipliers to enforce constraints on the particle so that the fluid inside the particle domain is forced to mimic rigid body motion. The immersed boundary method (IBM) (Peskin, 2002; Uhlmann, 2005, 2008) realizes the no-slip boundary condition on particle surface by imposing a localized forcing field. Similarly, the force coupling method (Maxey and Patel, 2001; Yeo *et al.*, 2010) uses smoothed body force field to represent the effects of particles on the fluid phase, in terms of low order force multiple expansion. The hybrid Physalis method (Takagi *et al.*, 2003; Zhang and Prosperetti, 2003, 2005) handles the no-slip boundary condition by coupling an analytical Stokes expansion valid in a narrow but finite region near each particle surface with the numerical solution outside the particle. The pseudo-penalization method (Homann and Bec, 2010) imposes a strong drag to the fluid velocity at the particle location, so that it relaxes quickly to the particle solid-body motion.

In contrast to the above macroscopic CFD approaches based on the Navier-Stokes equations, in the mesoscopic lattice Boltzmann method (LBM) (Aidun *et al.*, 1998; Ladd, 1994a, 1994b; Ten Cate *et al.*, 2004) the fluid field is realized through local moments of a lattice Boltzmann equation on a uniform lattice grid. The no-slip boundary condition can be imposed by using a simple interpolated bounce-back scheme. To reduce force oscillations on the particles, the immersed-boundary-lattice-Boltzmann method (IB-LBM) (Feng and Michaelides, 2004, 2005) has also been developed by replacing the conventional bounce-back scheme with a direct forcing scheme applied on a set of Lagrangian boundary points representing particle surfaces.

The first motivation of this dissertation is to better understand the motion and hydrodynamic interactions of finite-size inertial particles suspended in a turbulent flow. One of the major challenges is to develop an efficient and accurate approach to resolve the disturbance flows around particles suspended in a turbulent carrier fluid.

In this work, we will adopt the lattice Boltzmann method to perform the particle-resolved simulation. The particle-turbulence two-way coupling and particle-particle interactions will be simultaneously considered. Results concerning decaying turbulent flow laden with finite-size particles will be discussed. Several validation cases will also be presented where the results of the LB simulations are compared directly with those from the Physalis approach.

1.1.2 Porous Media Flow and Colloidal Particle Transport

Unlike the first application where fundamental questions of particle-laden turbulence are explored, this second application concerns a specific transport problem of sub-micron sized colloids. The moving particles in the first application are now fixed and used to construct a model porous medium, based on which the complex porous media flows are solved. The colloidal particle transport phenomenon is then examined by tracking colloid's position and its interactions with surrounding flow and granular collectors.

In recent years, colloid retention and transport in the subsurface porous media has received increasing attention due to its great significance in a number of environmental fields, such as waste water treatment, riverbank filtration, bioremediation, and protection of groundwater supplies from colloid and colloid-associated pollutants (Steffan *et al.*, 1999; Ferguson *et al.*, 2003; de Jonge *et al.*, 2004; Tufenkji, 2007). The large surface area of mobile colloids can be an effective means to adsorb or bind pollutants, e.g., organics pesticides, heavy metals, and radio nuclides, which can travel significant distances through soil porous media via colloids transport. In addition, some colloids can themselves be contaminants, such as viruses, bacteria, and protozoa. These colloids may be introduced into the subsurface from various sources including leaking landfills, or land disposal of treated water effluents (Mawdsley, *et al.*, 1995; Smith and Perdek, 2004). The migration of these colloids poses potential risk to contaminate groundwater and hence could be a serious public health concern (Jin and Flury, 2002; Johnson *et al.*, 2007). Moreover, some other natural and industrial processes involving

colloid transport include migration of clay minerals and the consequent nutrient loss in soil fertility (McGechan and Lewis, 2002), infiltration of rain water in urban areas with pollutants from road traffic and building roofs, manufactured nanomaterials (Metreveli and Frimmel, 2005), and effective waste water treatment (Yao *et al.*, 1971). All these important environment impacts necessitate the full understanding of the mechanisms and kinetics of colloidal deposition and mobilization in porous media.

Deposition of colloids onto grain surfaces from a flowing suspension in porous meida involves two sequential steps: transport, which is dominated by convection and diffusion, and deposition, which is controlled by interaction forces between colloids and collector surfaces. The interaction forces include van der Waals attraction and electrostatic double-layer interaction, as described by the Derjaguin-Landau-Verwey-Overbeek (DLVO) theory (Derjaguin and Landau, 1941; Verwey and Overbeek, 1948), which has been extended to include additional forces such as Lewis acid/base and hydrophobic interactions (van Oss, 1994). A DLVO interaction profile is constructed by the total interaction energy as a function of separation distance between a colloid surface and a collector surface. When the interactive surfaces are oppositely charged, both electrostatic and van der Waals forces are attractive thus there is no energy barrier to colloid deposition. This is regarded as the favorable surface condition. However, when the interactive surfaces are like-charged, the electrostatic double-layer force is repulsive and a typical DLVO energy profile is characterized by a deep attraction well (the primary energy minimum) at a very small separation distance, a maximum energy barrier, and a shallow attraction well (the second energy minimum) at a larger separation distance. This is referred to as the unfavorable condition, which is the most prevalent condition in natural subsurface environments.

The classic filtration theory (CFT) has been found to accurately predict colloid retention in granular porous meida when there is no energy barrier to colloid deposition (Rajagopalan and Tien, 1976; Tufenkji and Elimelech, 2004). In this case, colloid retention occurs primarily through strong attachment in the primary energy minimum

(PEM), and the hydrodynamic drag or Brownian force is not strong enough to cause detachment. Therefore, the concentrations of mobile colloids decrease exponentially with distance from the source (Tufenkji and Elimelech, 2004; Li *et al.*, 2004, 2005). Under strongly unfavorable conditions where colloid and collector surfaces are like charged and the energy barrier is high, CFT predicts no deposition because colloids cannot overcome the energy barrier to become attached in the PEM. This is in contradiction with a number of experimental studies, which have demonstrated colloid deposition under such conditions (Elimelech and O'Melia, 1990; Tufenkji and Elimelech, 2004; Bradford *et al.*, 2002, 2006; Li *et al.*, 2004, 2005; Shen *et al.*, 2007).

The significant deviation from CFT has been addressed through several retention mechanisms, among which deposition at secondary energy minimum (SEM) is believed to be one of the major reasons for the failure of CFT. Experiments have shown colloid deposition is reversible when solution ionic strength decreases (Hahn and O'Melia, 2004; Tufenkji and Elimelech, 2005; Shen *et al.*, 2007, 2008), which should not occur for the deposition in PEM. Indeed, colloids are retained in the shallow attractive energy well, i.e., the SEM, and is released back into the bulk suspension due to the reduced or eliminated SEM as a result of reduced solution ionic strength. This is the so called re-entrainment/detachment process. Colloids weakly retained in SEM can also translate along the grain surfaces owing to tangential hydrodynamic drag and finally reside in the flow stagnation region where the fluid drag force is insufficient to drive colloid motion (Johnson and Tong, 2006; Bradford *et al.*, 2007). Under certain solution chemistry conditions, a fraction of the colloids deposited in the SEM can jump over the energy barrier and be deposited in the PEM due to the fluctuations of their internal energy (Franchi and O'Melia, 2003). They can also be released into the bulk solution when the magnitude of the SEM and the Brownian kinetic energy are comparable (Shen *et al.*, 2007).

Another mechanism contributing to the deviation from CFT is straining/wedging. CFT is originated from the Happel sphere-in-cell model (Happel, 1958) represented by

an isolated solid sphere with a uniform layer of liquid film. Hence the trapping of colloids at grain-to-grain contact region (wedging) or at pore throats that are too small to allow passage (straining) are not considered in CFT. Early studies treat straining as a process that only depends on the ratio of colloid diameter to collector diameter, and reported threshold ratio in a wide range from 0.154 (Herzig *et al.*, 1970) to as low as 0.005 (Bradford *et al.*, 2002). More recent work suggests that straining is influenced by both physical and chemical factors. Bradford *et al.* (2007) asserted that colloids retained in the SEM can be transported to straining sites by hydrodynamic torques, and then be further immobilized due to the limitation of size, enhanced DLVO interactions with multiple interfaces and attenuated hydrodynamic effects in regions of low flow velocity. This hypothesis is yet to be corroborated by experimental evidence.

The third reason that contributes to the discrepancies between CFT and experimental observation is surface heterogeneity. While most previous studies assume surface charges for both colloids and collector are averagely distributed, this is not the case in complex natural environment (McCarthy and McKay, 2004). In an overall negative-charged environment, some minor mineral components may be positively charged and thus serve as attachment sites where the energy barrier is reduced or eliminated (Song and Elimelech, 1993, 1994). In addition to charge heterogeneities, physical heterogeneities resulting from surface roughness, irregularly-shaped grains, and pore geometry may also have strong impacts on re-entrainment by altering the local hydrodynamic conditions.

Despite considerable progress made to improve the understanding of colloid transport behaviors, some important issues still remain unclear due to the limitations of experimental setup and theoretical modeling, especially for unfavorable conditions. For example, how would the pore-scale flow geometry, including the grain-to-grain contact region and physcical surface heterogeneity, contribute to colloid retention and re-entrainment? What are the coupled effects of hydrodynamic forces, colloidal interaction forces, and Brownian motion on colloid deposition?

The second motivation of this dissertation is to fill the simulation gap and

build up our ability to predict colloid retention and transport in saturated soil porous media in the presence of energy barrier, complex pore-scale flow geometry, and surface heterogeneities. Again, two numerical methods, the LBM and Physalis, will be applied to the same model geometry for cross-validation. Lagrangian particle-based approach will be adopted to track the trajectory of each colloid. Physicochemical, hydrodynamic, and Brownian forces will be included in the colloids equation of motion. Effects of flow speed, solution ionic strength, and local hydrodynamic interactions will be explored.

1.2 Previous Work

1.2.1 Particle-Resolved Turbulent Flow Simulation

In recent years, there have been a few studies of particle-resolved simulation of turbulent particle-laden flows as summarized in Table 1.1. The interaction of a single fixed or moving particle with a turbulent flow has been studied by several researchers (Burton and Eaton, 2005; Homann and Bec, 2010; Naso and Prosperetti, 2010; Kim and Balachandar, 2012). Using direct-forcing IBM, Xu and Subramaniam (2010) studied flow modulation by a group of fixed particles, and Tenneti *et al.* (2011) examined drag forces on a random cluster of fixed spheres. These studies provided a better understanding on the nature of flow modulation near the surface of the particle due to the finite-size effect that depends on the particle Reynolds number. Using a direct-forcing fictitious domain method, Wu *et al.* (2011) and Shao *et al.* (2012) investigated flow modulation by finite-size particles in a pipe and channel flow.

Ten Cate *et al.* (2004) conducted a particle-resolved simulation of forced turbulent flows laden with solid particles using LBM. The carrier-fluid turbulence was maintained at Taylor microscale Reynolds number $Re_\lambda = 61$ using a spectral forcing scheme. The no-slip boundary condition on the particle surface was implemented by applying a body force field to the fluid domain. A subgrid lubrication force was computed based on relative location and velocities of approaching particles (Nguyen and Ladd, 2002). The simulation considered up to $3,868$ particles, corresponding to volume fractions ranging from 2% to 10%. The density ratio between the solid and

Table 1.1: Particle-resolved simulations of turbulent particle-laden flows.

Chronological	Method	Physical issues studied
Ten Cate *et al.* (2004)	LBM	Turbulent modulation, particle-particle hydrodynamic interaction and collision. Forced.
Burton & Eaton (2005)	Finite volume / overset grid	Turbulent flow on a single fixed particle: dissipation rate and kinetic energy as a function of distance from particle surface; force acting on the particle. Decaying.
Zhang & Prosperetti (2005)	Finite-difference / Stokes flow exp.	Turbulence modulation and force on particle. Decaying.
Uhlmann (2008)	LBM with IBM	Turbulent suspension in a vertical channel.
Yeo *et al.* (2010)	Force coupling method	Turbulent modulation by particles and bubbles; Lagrangian statistics. Forced.
Lucci *et al.* (2010)	Finite-difference with IBM	Turbulent modulation; local variation around particle; energy spectra. Decaying.
Naso & Prosperetti (2010)	Finite-difference / Stokes flow exp.	Turbulent flow on a single fixed particle. Forced.
Homann & Bec (2010)	Pseudo-penalization method	A single neutrally buoyant particle in a forced turbulent flow.

fluid phase ranges from 1.15 to 1.73. The particle diameter is set to 8 grid spacing in the simulations. It was demonstrated that particle-fluid relative motion results in an enhancement of kinetic energy $E(k)$ and energy dissipation rate $\varepsilon(k)$ at large wave numbers and a reduction of both spectra at small wave numbers. Oscillations in $E(k)$

were found at large wave numbers, although they are negligible when compared to the total kinetic energy of the system.

Zhang and Prosperetti (2005) applied the hybrid method Physalis to study decaying particle-laden turbulence. A periodic cubic domain of 64^3 contains 100 spherical particles with radius equal to 39% of the initial Taylor microscale. Particle-fluid density ratio was set to 1.02. Gravity was neglected and particle-particle short range interactions were represented by an elastic model. The Taylor microscale Reynolds number changed from 29 to 14 during the time interval of the simulation. It was reported that, compared with the point-particle model, the finite-size particles decrease the kinetic energy, show less diffusion in terms of mean particle displacement, and exhibit a stronger tendency of clustering.

Uhlmann (2008) considered particulate suspensions in a vertical turbulent channel flow, using the immersed boundary method to treat the solid particles. The incompressible Navier-Stokes equations were solved by a fractional-step scheme on a staggered grid. Up to $4,096$ particles were simulated in a turbulent flow sustained at a bulk flow Reynolds number of $2,700$. The particle diameter was set to approximately 11 wall units, corresponding to a volume fraction of 0.42%. The density ratio varied from 2.2 to 10. It was found that the presence of particles induced large scale streaklike velocity perturbations, although no significant aggregation of particles was observed.

Using the force coupling method, Yeo *et al.* (2010) studied turbulence modulation by finite-size particles and bubbles. The flow was forced at large scales. They demonstrated that the pivot wavenumber characterizing the transition from damped to enhanced energy content is mainly a finite-size effect of particles and that the transition scale is almost independent of the particle to fluid density ratio.

Lucci *et al.* (2010) applied the immersed boundary method to study modulation of decaying turbulence by solid particles ofsize comparable to the Taylor microscale. The carrier flow had an initial Taylor Reynolds number of 75. Density ratio varied from 2.56 to 10.0. Volume fraction of the dispersed phase was 10% or less, and a

maximum number of 6,400 particles were considered in their simulations. They studied turbulence modulation by particles and structure of disturbance flow around the particles.

1.2.2 Pore-Scale Colloid Dynamic Modeling

Due to the low concentration and vanishing Stokes number of colloids, it is generally assumed that in pore-scale colloid dynamic simulation, the fluid flow is independent of the presence of colloids, and the motion of colloid is governed by the viscous flow around it. Consequently, pore-scale dynamic modeling can be decomposed into two parts. The first is the simulation of liquid flow through soil porous media. The second is a method to model or simulate the transport of colloids by the liquid flow and its interaction with grain surfaces. Some recent studies (Bradford *et al.*, 2007; Johnson *et al.*, 2007; Shen *et al.*, 2007) have shown that pore geometry affects local flow distribution through large local variations of flow velocity and shear rate, and can contribute significantly to colloid retention. Therefore, an accurate pore-scale flow simulation in realistic three-dimensional porous media becomes essential for the development of a quantitative pore-scale modeling tool.

Earlier numerical study on soil porous media flow typically employed the unit-cell-based flow representation due to its computational efficiency. Examples include the sphere-in-cell model (Happel 1958; Rajagopalan and Tien, 1976), 2D and 3D constriction tube models (Payatakes *et al.* 1974a, 1974b; Paraskeva *et al.*, 1991; Burganos *et al.*, 1994). These unit-cell models take advantage of symmetry properties of flow passage and make use of either the available analytical creepingf flow solution or numerical solution of the viscous flow in simple model geometries. But they only provide a phenomenological representation of soil pore-scale geometry without consideration of grain-grain contact and grain surface irregularities. Cushing and Lawler (1998) considered grain-grain contact in a unit cell representing densely packed regular array of spheres and solved the creeping fluid flow using an approximate Galerkin's method

(Snyder and Stewart, 1966). They then studied colloid attachment efficiency by solving trajectories of colloids. While their model clearly demonstrated colloid deposition in the presence of an energy barrier, the attachment efficiency was found to be insensitive to the presence or absence of the energy barrier, which was in direct contradiction with experimental evidence and theoretical expectation. They attributed this to the random nature of the grain packing not represented in their unit cell model. Johnson *et al.* (2007) adopted the same unit-cell approach to solve the pore-scale flow and a trajectory approach for colloids; they confirmed colloid retention in flow stagnation zones and wedging in grain-to-grain contacts. They also indicated the need to solve viscous flows through pore domains rendered from actual porous media, in order for such approach to become a useful quantitative tool.

In addition to the pore-scale viscous flow simulation, the colloids transport modeling is of concern as well. It can be performed in either an Eulerian or a Lagrangian fashion. The Eulerian approach considers the distribution of particle concentration as a mean-field variable over space and time (Bradford and Toride, 2007; Bradford *et al.*, 2007). This approach applied to particle deposition yields an extended advection-dispersion equation with source/sink terms that parameterize the effects of colloid-surface interactions. The specification of these source/sink terms involves modeling assumptions, e.g., constant deposition and release rate coefficients, that may not be applicable to unfavorable conditions (Bradford and Toride, 2007).

The Lagrangian approach focuses on a single colloid and tracks its position and velocity over time according to Newton's second law. The colloid's equation of motion may include physicochemical, hydrodynamic, Brownian and body forces and torques. The physicochemical forces typically include contributions from the electrostatic, Lifshitz-van der Waals, and Lewis acid/base interactions (van Oss 1994). The hydrodynamic forces may include Stokes drag, added mass, and fluid acceleration force. The hydrodynamic forces can be modified by a grain surface, nearby presence of other colloids, and local flow shear (Rajagopalan and Tien, 1976; Kim and Karrila, 1991).

While the Lagrangian approach is computationally more expensive than the Eulerian approach, it provides a more direct mechanistic description of microscopic colloid transport that can be helpful for elucidating the relevant processes. Furthermore, the discrete nature of the Lagrangian approach makes it much more feasible to include complex interactions with heterogeneous grain surface properties. For these reasons, most previous mechanistic modeling studies adopted the Lagrangian trajectory approach.

1.3 Dissertation Layout

The rest of the dissertation is organized into four chapters. A brief summary of each is given as follows.

The main contribution of this work is the development and implementation of the lattice Boltzmann method (LBM) and the hybrid Physalis method, and their applications to the study of particle-resolved turbulent flow, as well as porous media flow. In Chapter 2, we shall first review the development and formulation of these two methods in detail, and then demonstrate their cabability in simulating an unsteady particle-resolved flow, i.e., the gravitational settling of two spherical particles in a square channel. The well-documented "drafting, kissing, and tumbling" process is reproduced by both methods. The quantative agreement of the results cross-validates the implementation of the two methods.

In Chapter 3, we simultaneously apply the two methods to solve the viscous flows in porous media represented by a channel packed with spherical grain particles. Detailed comparison reveals better accuracy of LBM in simulating the 3D pore-scale flows with multiple grain-grain and grain-wall contact points. The well-resolved pore-scale flow is then employed in the simulation of colloid transport and retention under unfavorable conditions using a Lagrangian trajectory approach. Results demonstrate the capture of colloids by the secondary energy minimum. The effects of colloid-grain surface local hydrodynamic interaction will be discussed.

In Chapter 4, we focus on the particle-resolved simulation for turbulent flow

laden with finite-size particles. The multiple-relaxation-time lattice Boltzmann equation (MRT-LBE) is implemented under the framework of MPI parallelization. Issues addressed includes the no-slip boundary condition on the moving particle boundaries, construction of particle distribution functions at newly converted fluid lattice nodes, and particle-related MPI implementation details in order to boost the computational efficiency. The method is first validated using unsteady sedimentation of a single particle and then a multi-particle random suspension, followed by a further verification for the case of decaying turbulence laden with a single fixed particle. It is then applied to a decaying isotropic turbulence laden with large loading of particles of Kolmogorov to Taylor microscale sizes. Turbulent modulation due to the presence of finite-size inertial particles is found to be in accordance with related studies. The simulation results also suggest the dependence of the pivot wavenumber on the particle size, the ratio of particle size to flow dissipation range scales, as well as the particle-to-fluid density ratio. In addition, local profiles relative to particle surface are examined to shed light on the strong modulation occurring near particle surface.

Finally, in Chapter 5, we present a summary of major conclusions and provide recommendations for future work.

Chapter 2

SIMULATION METHODS: THE LATTICE BOLTZMANN METHOD AND THE PHYSALIS APPROACH

For particle-laden flows of practical interest, analytical solutions are typically not available due to the complex geometries involved. In this work, we will simultaneously apply two numerical methods to perform direct simulations for viscous flows laden with finite size particles. In this way the simulations can be cross-validated in the absence of analytical solutions. The two methods adopted here are the lattice Boltzmann method (LBM) based on the mesoscopic lattice Boltzmann equation (LBE), and the macroscopic continuum-based hybrid method, namely, Physalis. In this chapter, we will first review the LB method, starting from its origin in the lattice gas automata, followed by the development of the single-relexation-time (SRT) LBE model, and then the more recent multiple-relaxation-time (MRT) LBE model. Due to its superior stability and accuracy relative to SRT LBE, the MRT LBE model is adopted in our LB simulation. Details of the theory and numerical implementation of the model are provided, which is essential for developing the MRT LBE solver. Next, we will review the Navier-Stokes based Physalis method. This hybrid method couples the local spectral representation near the particle boundary with the numerical solution obtained on the rest of the domain. Three major components, including the construction of the analytical solution, the second-order projection method for the numerical solver, and the coupling procedure are discussed in detail to give a complete understanding of this approach and its numerical implementation. Finally, we will demonstrate these methods by simulating the sedimentation of two spherical particles in a square channel. The LBM and Physalis results are in good agreement, which validates our implementation of the two methods.

2.1 Lattice Boltzmann Method

2.1.1 Single-Relexation-Time LBE

Historically, the lattice Boltzmann method originated from the lattice gas automata (LGA), a discrete particle kinetics utilizing a discrete lattice and discrete time. In the LGA model, a set of Boolean variables $n_i(\mathbf{x}, t)(i = 1, \cdots, N)$ is defined on a regular lattice to describe particle occupation at site $\mathbf{x}$ and time t. The evolution equation of the LGA is

$$n_i(\mathbf{x} + \mathbf{e}_i, t + 1) = n_i(\mathbf{x}, t) + \Omega_i(n(\mathbf{x}, t)), \qquad i = 1, \cdots, N \tag{2.1}$$

where $\mathbf{e}_i$ is the local particle velocity, and Ω_i is the collision operator which represents presence or absense of $n_i(\mathbf{x}, t)$ due to collision. The evolution of the system consists of two steps: streaming and collision. At each time step, each particle moves to the nearest node in the direction of its velocity. When particles arrives at a node, they interact and change their velocity directions according to scattering rules which conserve mass, momentum, and energy locally. Frisch *et al.* (1986) and d'Humières *et al.* (1986) have shown that Navier-Stokes equations can be recovered from this model, and the Galilean invariance is restored as well. The use of Boolean variables in Eq. (2.1), however, introduces statistical noise in the LGA model, and large lattice regions over long times of simulation must be averaged to obtain the results.

To overcome the noisy behavior of LGA, McNamara and Zanetti (1988) replaced the Boolean variables n_i with single-particle distribution functions (real variables) $f_i = \langle n_i \rangle$, where $\langle\rangle$ denotes an ensemble average. The discrete kinetic equation for the particle distribution is similar to the kinetic equation in LGA in Eq. (2.1),

$$f_i(\mathbf{x} + \mathbf{e}_i \delta t, t + \delta t) = f_i(\mathbf{x}, t) + \Omega_i(f(\mathbf{x}, t)), \qquad i = 1, \cdots, N \tag{2.2}$$

where f_i is the particle distribution function along the ith direction, Ω_i is the collision operator which represents the rate of change of f_i resulting from collision. Note that

Ω_i depends only on local distribution function and is required to satisfy mass and momentum conservation at each lattice

$$\sum_{i=1}^{N} \Omega_i = 0, \qquad \sum_{i=1}^{N} \Omega_i \mathbf{e}_i = 0. \tag{2.3}$$

The collision operator in Eq. (2.2) is nonlinear, which implies that excessive memory and computational cost are required when calculating the term. Higuera and Jiménez (1989) simplified the LBE model by assuming the distribution is close to the local equilibrium state, thus the collision operator can be expressed in a quasilinear form,

$$\Omega_i(f) = -A_{ij}(f_j - f_j^{eq}) \tag{2.4}$$

where the distribution function f_i is expanded into equilibrium component f_i^{eq} and nonequilibrium part f_i^{neq}, A_{ij} is the quasilinear scattering matrix.

A further simplified collision operator was proposed by Higuera *et al.* (1989). In this approach, a particular simple linearized collision operator is designed using a single relaxation time τ towards the local equilibrium. The relaxation term is known as the Bhatnagar-Gross-Krook (BGK) collision operator (Bhatnagar *et al.*, 1954), and the correspondent LBE is referred to as the lattice BGK (LBGK) equation,

$$f_i(\mathbf{x} + \mathbf{e}_i \delta t, t + \delta t) = f_i(\mathbf{x}, t) - \frac{f_i - f_i^{eq}}{\tau} \tag{2.5}$$

The LBGK model is noise-free and has Galileian invariance with the velocity independent of pressure. Navier-Stokes equations are obtained from this model at the second order of approximation with an appropriate equilibrium distribution (Qian *et al.*, 1992; Chen *et al.*, 1992). The discrete equilibrium distribution function f_i^{eq} is inspired by the Maxwell-Boltzmann equilibrium function,

$$f_i^{eq} = \frac{\rho}{(2\pi RT)^{D_0/2}} \exp\left(-\frac{(\mathbf{e}_i - \mathbf{u})^2}{2RT}\right) \tag{2.6}$$

where D_0, R, T, ρ, and $\mathbf{u}$ are the dimension of space, gas constant, temperature, macroscopic density and velocity, respectively. Assuming the fluid velocity $\mathbf{u}$ is a small

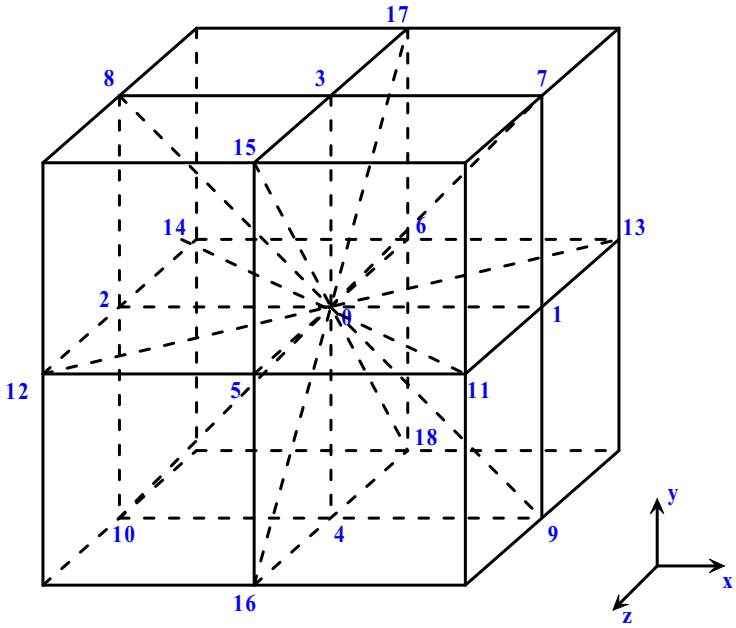

Figure 2.1: Schematic for the D3Q19 lattice model.

parameter compared with the sound speed, Eq. (2.6) can be approximated up to a second-order Taylor series,

$$f_i^{eq} = \frac{\rho}{(2\pi RT)^{D_0/2}} \exp\left(-\frac{\mathbf{e}_i^2}{2RT}\right)\left[1 + \frac{(\mathbf{e}_i \cdot \mathbf{u})}{RT} + \frac{(\mathbf{e}_i \cdot \mathbf{u})^2}{2(RT)^2} - \frac{\mathbf{u}^2}{2RT}\right] \tag{2.7}$$

He and Luo (1997a,b) defined the LBE sound speed $c_s \equiv \sqrt{RT}$. With the particle velocity $\mathbf{e}_i$ and fluid velocity $\mathbf{u}$ being normalized by $\sqrt{3RT} = c \equiv \delta_x/\delta_t$, where δ_x and δ_t are lattice spacing and time, respectively, $c_s = c/\sqrt{3} = 1/\sqrt{3}$. Eq. (2.7) can then be written as

$$f_i^{eq} = w_i \rho \left[1 + 3(\mathbf{e}_i \cdot \mathbf{u}) + \frac{9(\mathbf{e}_i \cdot \mathbf{u})^2}{2} - \frac{3\mathbf{u}^2}{2}\right] \tag{2.8}$$

where the weight $w_i = \exp(-\frac{3}{2}\mathbf{e}_i{}^2)/(2\pi/3)^{D_0/2}$ can be evaluated by Gaussian-type quadrature (He and Luo, 1997a). For the D3Q19 lattice applied in this thesis (Figure 2.1), the weighting coefficients are determined as $w_0 = 1/3$, $w_1 = \cdots = w_6 = 1/18$, and $w_7 = \cdots = w_{18} = 1/36$.

The relaxation time τ is a parameter characterizing the constitutive behavior of the fluid at a microscopic level. For incompressible isothermal flows, it is connected with the macroscopic kinematic viscosity of the fluid according to

$$\nu = c_s^2 \delta_t (\tau - \frac{1}{2}) = \frac{2\tau - 1}{6} \tag{2.9}$$

The macroscopic variables, ρ, $\mathbf{u}$ and T are the microscopic velocity moments of the particle distribution function f_i:

$$\rho = \sum_{i=1}^{N} f_i, \qquad \rho \mathbf{u} = \sum_{i=1}^{N} f_i \mathbf{e}_i, \qquad \rho\varepsilon = \frac{1}{2} \sum_{i=1}^{N} f_i (\mathbf{e}_i - \mathbf{u})^2 \tag{2.10}$$

with ε denotes the kinetic energy $\varepsilon = \dfrac{D_0}{2} RT = \dfrac{D_0}{2} N_A k_B T$, where N_A and k_B are the Avogadro's number and the Boltzmann constant, respectively. Pressure is related to the density by the equation of state

$$p = c_s^2 \rho \tag{2.11}$$

Although the LBE model was originally derived from the LGA model, it has also been shown that the LBE can be obtained from the continuum Boltzmann equation for discrete velocities by using a small Mach number expansion. The details are described in He and Luo (1997).

The numerical implementation of the LBE method are realized in a two-step stream-and-collide procedure as follows.

1. Collision:
   - Calculate the macroscopic flow variables using Eq. (2.10).
   - Determine the equilibrium distribution functions using Eq. (2.8).
   - Compute the intermediate distribution function for each lattice velocity direction at each site
   $$f_i^*(\mathbf{x}, t) = f_i(\mathbf{x}, t) + \Omega_i(f(\mathbf{x}, t)), \qquad i = 1, \cdots, N$$
   - Modify f_i^* for boundary nodes according to the boundary conditions.
2. Streaming:
   - Particle distribution functions are simply advected in the direction of corresponding discrete velocities, towards the neighbor lattice nodes
   $$f_i(\mathbf{x} + \mathbf{e}_i \delta t, t + \delta t) = f_i^*(\mathbf{x}, t), \qquad i = 1, \cdots, N$$

2.1.2 Multiple-Relexation-Time LBE

The single-relexation-time lattice BGK equation in Eq. (2.5) has become the most popular lattice Boltzmann model due to its extreme simplicity. However, the use of a single relaxation parameter also introduces some obvious defects of the LBGK model, such as a fixed Prandtl number ($Pr = 1$) and reduced numerical stability at large Reynolds number. In contrast, the multiple-relaxation-time (MRT) LBE, also referred to as the generalized LBE, allows different relaxation times to be individually tuned for different moments of the discrete velocity set. Consequently, the MRT LBE model is much more stable than its LBGK counterpart, and the Prandtl number can be arbitrary if MRT LBE simulations of thermal flows are desired.

The evolution of particle distribution function (Eq. (2.5)) can be rewritten in a concise vector form for the generalized LBE model (d'Humières, 1992; d'Humières *et al.*, 2002)

$$|f(\mathbf{x}+\mathbf{e}_i\delta t, t+\delta t)\rangle - |f(\mathbf{x},t)\rangle = -\mathbf{S}\left[|f(\mathbf{x},t)\rangle - |f^{eq}(\mathbf{x},t)\rangle\right] \tag{2.12}$$

where $\mathbf{S}$ is the collision matrix, Dirac notation ket $|\cdot\rangle$ is used to denote column vector,

$$\begin{aligned}
|f(\mathbf{x},t)\rangle &\equiv (f_0(\mathbf{x},t), f_1(\mathbf{x},t), \cdots, f_N(\mathbf{x},t))^T, \\
|f^{eq}(\mathbf{x},t)\rangle &\equiv (f_0^{eq}(\mathbf{x},t), f_1^{eq}(\mathbf{x},t), \cdots, f_N^{eq}(\mathbf{x},t))^T, \\
|f(\mathbf{x}+\mathbf{e}_i\delta t, t+\delta t)\rangle &\equiv (f_0(\mathbf{x}+\mathbf{e}_0\delta t, t+\delta t), \cdots, f_N(\mathbf{x}+\mathbf{e}_N\delta t, t+\delta t))^T,
\end{aligned}$$

and the superscript 'T' denotes the transpose operator. Note that the LBGK model is a special case of the generalized LBE, in which the collision matrix $\mathbf{S} = \mathbf{I}/\tau$, where $\mathbf{I}$ is the identity matrix, and τ is the single relaxation time, i.e., the $(N+1)$ relaxation times are all equal for LBGK model.

d'Humières *et al.* (2002) have shown that the collision matrix $\mathbf{S}$ is designed based on its eigenvector matrix $\mathbf{M}$ and a diagonal matrix $\hat{\mathbf{S}}$ consisting of corresponding eigenvalues, namely,

$$\mathbf{S} = \mathbf{M}^{-1} \cdot \hat{\mathbf{S}} \cdot \mathbf{M} \tag{2.13}$$

The transformation matrix $\mathbf{M}$ consists of orthogonal basis set constructed by orthogonalizing the polynomials of the column vectors $\{|e_x\rangle, |e_y\rangle, |e_z\rangle\}$ by standard Gram-Schmidt procedure. The velocity space spanned by $|f\rangle \equiv (f_0, f_1, \cdots, f_N)^T$ can then be related to the moment space spanned by $|m\rangle \equiv (m_0, m_1, \cdots, m_N)^T$ by a linear mapping:

$$|m\rangle = \mathbf{M}|f\rangle, \quad \text{and} \quad |f\rangle = \mathbf{M}^{-1}|m\rangle. \tag{2.14}$$

Combining Eq. (2.12) to Eq. (2.14), the evolution equation of the MRT LBE becomes

$$|f(\mathbf{x} + \mathbf{e}_i\delta t, t + \delta t)\rangle - |f(\mathbf{x}, t)\rangle = -\mathbf{M}^{-1}\hat{\mathbf{S}}\left[|m(\mathbf{x}, t)\rangle - |m^{eq}(\mathbf{x}, t)\rangle\right] \tag{2.15}$$

Note that in Eq. (2.15), the advection process is naturally executed in the discrete velocity space, while the collision process is accomplished in the moment space. The reason in favor of using the moment representation is due to the fact that various physical process in fluids can be approximately described by coupling of different modes of the collision operator, which are directly related to the moments. Since the MRT LBE allows the independent control of each mode, this mechanism provides an effective way to incorporate the flow physics into the LBE models in the context of kinetic theory.

For the D3Q19 lattice model used in this dissertation (Figure 2.1), the transformation matrix is given by

$$\mathbf{M} = (|\rho\rangle, |e\rangle, |\varepsilon\rangle, |j_x\rangle, |q_x\rangle, |j_y\rangle, |q_y\rangle, |j_z\rangle, |q_z\rangle, |3p_{xx}\rangle, |3\pi_{xx}\rangle, |p_{ww}\rangle, |\pi_{ww}\rangle, |p_{xy}\rangle, |p_{yz}\rangle, |p_{xz}\rangle, |m_x\rangle, |m_y\rangle, |m_z\rangle)^T =$$

$$\begin{pmatrix}
1 & 1 & 1 & 1 & 1 & 1 & 1 & 1 & 1 & 1 & 1 & 1 & 1 & 1 & 1 & 1 & 1 & 1 & 1 \\
-30 & -11 & -11 & -11 & -11 & -11 & -11 & 8 & 8 & 8 & 8 & 8 & 8 & 8 & 8 & 8 & 8 & 8 & 8 \\
12 & -4 & -4 & -4 & -4 & -4 & -4 & 1 & 1 & 1 & 1 & 1 & 1 & 1 & 1 & 1 & 1 & 1 & 1 \\
0 & 1 & -1 & 0 & 0 & 0 & 0 & 1 & -1 & 1 & -1 & 1 & -1 & 1 & -1 & 0 & 0 & 0 & 0 \\
0 & -4 & 4 & 0 & 0 & 0 & 0 & 1 & -1 & 1 & -1 & 1 & -1 & 1 & -1 & 0 & 0 & 0 & 0 \\
0 & 0 & 0 & 1 & -1 & 0 & 0 & 1 & 1 & -1 & -1 & 0 & 0 & 0 & 0 & 1 & -1 & 1 & -1 \\
0 & 0 & 0 & -4 & 4 & 0 & 0 & 1 & 1 & -1 & -1 & 0 & 0 & 0 & 0 & 1 & -1 & 1 & -1 \\
0 & 0 & 0 & 0 & 0 & 1 & -1 & 0 & 0 & 0 & 0 & 1 & 1 & -1 & -1 & 1 & 1 & -1 & -1 \\
0 & 0 & 0 & 0 & 0 & -4 & 4 & 0 & 0 & 0 & 0 & 1 & 1 & -1 & -1 & 1 & 1 & -1 & -1 \\
0 & 2 & 2 & -1 & -1 & -1 & -1 & 1 & 1 & 1 & 1 & 1 & 1 & 1 & 1 & -2 & -2 & -2 & -2 \\
0 & -4 & -4 & 2 & 2 & 2 & 2 & 1 & 1 & 1 & 1 & 1 & 1 & 1 & 1 & -2 & -2 & -2 & -2 \\
0 & 0 & 0 & 1 & 1 & -1 & -1 & 1 & 1 & 1 & 1 & -1 & -1 & -1 & -1 & 0 & 0 & 0 & 0 \\
0 & 0 & 0 & -2 & -2 & 2 & 2 & 1 & 1 & 1 & 1 & -1 & -1 & -1 & -1 & 0 & 0 & 0 & 0 \\
0 & 0 & 0 & 0 & 0 & 0 & 0 & 1 & -1 & -1 & 1 & 0 & 0 & 0 & 0 & 0 & 0 & 0 & 0 \\
0 & 0 & 0 & 0 & 0 & 0 & 0 & 0 & 0 & 0 & 0 & 0 & 0 & 0 & 0 & 1 & -1 & -1 & 1 \\
0 & 0 & 0 & 0 & 0 & 0 & 0 & 0 & 0 & 0 & 0 & 1 & -1 & -1 & 1 & 0 & 0 & 0 & 0 \\
0 & 0 & 0 & 0 & 0 & 0 & 0 & 1 & -1 & 1 & -1 & -1 & 1 & -1 & 1 & 0 & 0 & 0 & 0 \\
0 & 0 & 0 & 0 & 0 & 0 & 0 & -1 & -1 & 1 & 1 & 0 & 0 & 0 & 0 & 1 & -1 & 1 & -1 \\
0 & 0 & 0 & 0 & 0 & 0 & 0 & 0 & 0 & 0 & 0 & 1 & 1 & -1 & -1 & -1 & -1 & 1 & 1
\end{pmatrix} \tag{2.16}$$

Note that the row vectors in $\mathbf{M}$ (Eq. (2.16)) have explicit physical significance related to the moments of $\{f_i | i = 0, 1, \cdots, 18\}$, as shown in Table 2.1. The 19 moments can be categorized into two groups: the hydrodynamic moments that are locally conserved in the collision process (e.g., the mass density ρ and momentum $\mathbf{J} \equiv \{j_x, j_y, j_z\}$ for

Table 2.1: The physical significances related to the moments of $\{f_i\}$ in D3Q19 model.

Order	Quantity	Moment
0	Mass density:	$\rho = \langle \rho \vert f \rangle = \langle f \vert \rho \rangle$
2	Kinetic energy:	$e = \langle e \vert f \rangle = \langle f \vert e \rangle$
4	Kinetic energy square:	$\varepsilon = \langle \varepsilon \vert f \rangle = \langle f \vert \varepsilon \rangle$
1	Momentum:	$j_{x,y,z} = \langle j_{x,y,z} \vert f \rangle = \langle f \vert j_{x,y,z} \rangle$
3	Energy flux:	$q_{x,y,z} = \langle q_{x,y,z} \vert f \rangle = \langle f \vert q_{x,y,z} \rangle$
2	Diagonal viscous stress:	$p_{xx,yy,zz} = \langle p_{xx,yy,zz} \vert f \rangle = \langle f \vert p_{xx,yy,zz} \rangle$
2	Diagonal viscous stress:	$p_{ww} = p_{yy} - p_{zz}, p_{xx} + p_{yy} + p_{zz} = 0$
2	Off-diagonal viscous stress:	$p_{xy,yz,xz} = \langle p_{xy,yz,xz} \vert f \rangle = \langle f \vert p_{xy,yz,xz} \rangle$
4	Same symmetry as dianonal stress:	$\pi_{xx,ww} = \langle \pi_{xx,ww} \vert f \rangle = \langle f \vert \pi_{xx,ww} \rangle$
3	Parts of a third rank tensor:	$m_{x,y,z} = \langle m_{x,y,z} \vert f \rangle = \langle f \vert m_{x,y,z} \rangle$

isothermal flows), and the kinetic moments not conserved in the collision process. Accordingly, the equilibria of the moments can be separated into two groups as well: $\rho^{eq} = \rho$ and $\mathbf{J}^{eq} = \mathbf{J}$ for conserved moments, and functions of ρ, $\mathbf{J}$, and $\|\mathbf{J}\|^2$ for non-conserved moments. The details are described in d'Humières *et al.* (2002).

The diagonal eigenvalue matrix $\hat{\mathbf{S}}$ is defined as

$$\hat{\mathbf{S}} \equiv \mathrm{diag}(s_0, s_1, \cdots, s_{18}) \tag{2.17}$$

where the eigenvalues $\{s_i\}$ are the inverse of the relaxation times towards equilibria of their corresponding moments. For the conserved moments of density and momentum, $m_i^{eq} = m_i$, thus $s_0 = s_3 = s_5 = s_7 = 0$. For viscous stress moments, the relaxation times are related to kinematic viscosity ν as $s_9 = s_{11} = s_{13} = s_{14} = s_{15} = 2/(6\nu + 1)$. The rest of the relaxation times can be found by optimizing the isotropy and Galilean invariance of the model through linear analysis (Lallemand and Luo, 2000; d'Humières *et al.*, 2002), which gives $s_1 = 1.19$, $s_2 = s_{10} = 1.4$, $s_4 = 1.2$ and $s_{16} = 1.98$.

It should be stressed that MRT lattice Boltzmann equation allows the maximum freedom in constructing the non-conserved kinetic moments, as well as maximum number of adjustable relaxation times. An immediate consequence of using MRT LBE

instead of the LBGK model is a significant improvement in numerical stability, as demonstrated in d'Humières *et al.* (2002).

The numerical implementation of the generalized lattice Boltzmann equation involves a stream-and-collide procedure similar to that for the LBGK model. The difference lies in need of the projection from velocity space $|f\rangle$ to the moment space $|m\rangle$, and *vice versa*, as follows:

- Project $|f\rangle$ to $|m\rangle$ by $|f\rangle = \mathbf{M}^{-1}|m\rangle$.
- Compute equilibria of the moments $|m^{eq}\rangle$ following d'Humières *et al.* (2002).
- Perform collision step in moment space using multiple relaxation parameter

$$|\Delta m\rangle \equiv \hat{\mathbf{S}}\left[|m\rangle - |m^{eq}\rangle\right]$$

- Project $|m\rangle$ back to $|f\rangle$ by $|m\rangle = \mathbf{M}|f\rangle$, and perform advection step in velocity space

$$|f(\mathbf{x} + \mathbf{e}_i\delta t, t + \delta t)\rangle = |f(\mathbf{x}, t)\rangle + \mathbf{M}^{-1}|\Delta m\rangle.$$

With proper coding optimization techniques, the computational efficiency of the MRT LBE model can be fairly close to that of the LBGK method. d'Humières *et al.* (2002) have shown the overhead due to the projection between the velocity and moment space accounts for about 15% computational time of the LBGK algorithm.

2.1.3 No-Slip Boundary Conditions in the LBM

LBM is ideal for simulating fluid flows in complex geometries, such as flow through porous media and particle suspensions. This is partly due to the simple implementation of the no-slip velocity conditions at wall boundaries by using the bounce-back scheme. This scheme evolved from the boundary conditions of lattice gas and has been used in many particle-laden flow simulations to couple the freely-moving particles to the carrier fluid (Ladd, 1994a,b; Aidun *et al.*, 1998).

The bounce-back scheme means when a particle distribution streams to a wall node, the particle distribution scatters back to the node it came from. This operation is efficient in handling the scenario when a node locates near a boundary, with some

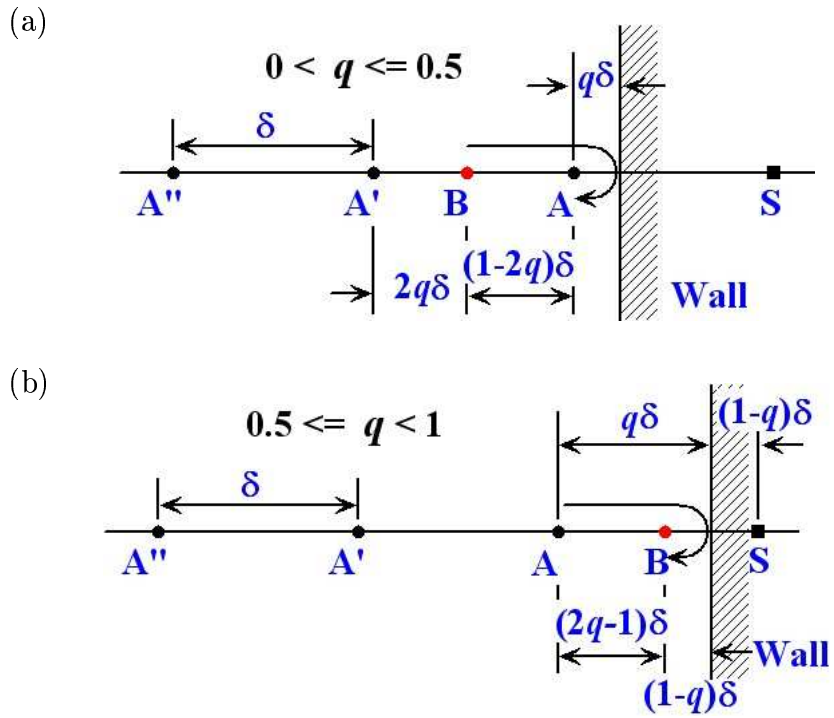

Figure 2.2: Schematics for the implementation of bounce-back scheme based on the boundary-cutting location on the link: (a) interpolation performed before streaming step when the percentage of the link outside the wall satisfies $q \leq 0.5$; (b) interpolation done after streaming when $q > 0.5$. Adapted from Lallemand and Luo (2003a).

of its neighboring nodes lie outside the flow domain. For example, in Figure 2.2, the distribution function of node A is supposed to be streamed from node S located inside wall after advection step, i.e., $f_{\bar{\alpha}}(A, t + \delta t) = \hat{f}_{\bar{\alpha}}(S, t)$. Here subscript α and $\bar{\alpha}$ denote the discrete velocity direction moving into and away from the solid wall, f and $\hat{f}$ refer to particle distribution function before and after streaming step, respectively. In our implementation, however, the LBE evolution only applies to the fluid nodes where the particle distribution functions are defined. No distribution function is defined for solid lattice node lying within the solid region, thus $\hat{f}_{\bar{\alpha}}(S)$ does not exist. This obstacle can be overcome by applying the bounce-back scheme as follows.

For the lattice node A near a particle surface, the relative boundary-cutting location on the link moving into the wall surface can be identified, namely, the percentage q of a link located outside the surface. Two scenarios are handled seperately in terms

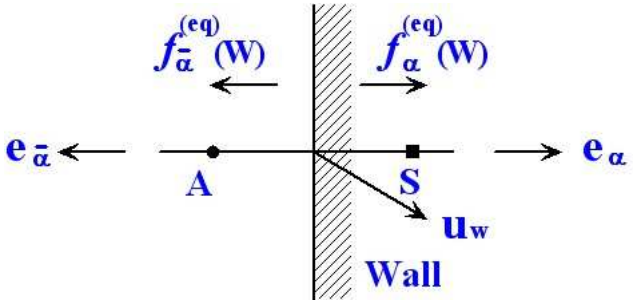

Figure 2.3: Schematic for the bounce-back scheme with moving wall.

of the q value to achieve better numerical stabiity (Lallemand and Luo, 2003a). When $q \leq 0.5$, the interpolated bounce-back is performed before streaming, as shown in Figure 2.2(a), where $f_{\bar{\alpha}}(A, t+\delta t) = \hat{f}_{\alpha}(B,t)$ can be obtained by first and second-order interpolation, respectively,

$$\begin{aligned} f_{\bar{\alpha}}(A) &= \hat{f}_{\alpha}(B) \\ &= \begin{cases} 2q\hat{f}_{\alpha}(A) + (1-2q)\hat{f}_{\alpha}(A'), & \text{2-point} \\ q(2q+1)\hat{f}_{\alpha}(A) + (1-2q)(1+2q)\hat{f}_{\alpha}(A') - q(1-2q)\hat{f}_{\alpha}(A''), & \text{3-point} \end{cases} \end{aligned} \tag{2.18}$$

When $q > 0.5$, the interpolated bounce-back is done after streaming, as shown in Figure 2.2(b). Note that in this case, bounce-back gives $f_{\bar{\alpha}}(B, t+\delta t) = \hat{f}_{\alpha}(A,t)$, and streaming step gives $f_{\bar{\alpha}}(A', t+\delta t) = \hat{f}_{\bar{\alpha}}(A,t)$, and $f_{\bar{\alpha}}(A'', t+\delta t) = \hat{f}_{\bar{\alpha}}(A',t)$. The interpolation method yields

$$f_{\bar{\alpha}}(A) = \begin{cases} \dfrac{1}{2q}\hat{f}_{\alpha}(A) + \dfrac{(2q-1)}{2q} f_{\bar{\alpha}}(A'), & \text{2-point} \\ \dfrac{1}{q(2q+1)}\hat{f}_{\alpha}(A) + \dfrac{(2q-1)}{q} f_{\bar{\alpha}}(A') - \dfrac{(2q-1)}{(2q+1)} f_{\bar{\alpha}}(A''), & \text{3-point} \end{cases} \tag{2.19}$$

Furthermore, when the wall boundary is in motion, an extra term should be considered to account for the additional momentum change due to the moving wall, as illustrated in Figure 2.3. In this case, the equilibrium function on the wall node is similar to that given by Eq. (2.8),

$$f_{\alpha}^{eq}(W) = w_i \rho \left[1 + 3(\mathbf{e}_{\alpha} \cdot \mathbf{u}_w) + \frac{9}{2}(\mathbf{e}_{\alpha} \cdot \mathbf{u}_w)^2 - \frac{3}{2}(\mathbf{u}_w \cdot \mathbf{u}_w) \right] \tag{2.20}$$

where u_w is the wall velocity. The moment change due to the moving wall can then be counted as

$$f_{out} - f_{in} = f_{\bar{\alpha}}^{eq}(W) - f_{\alpha}^{eq}(W) = -6w_i\rho(\mathbf{e}_\alpha \cdot \mathbf{u}_w) \tag{2.21}$$

When $q \leq 0.5$, the term $-6w_i\rho(\mathbf{e}_\alpha \cdot \mathbf{u}_w)$ can be directly added to Eq. (2.18); when $q > 0.5$, prior to being applied to Eq. (2.19), this term is reduced by a factor of $\frac{1}{2q}$ and $\frac{1}{q(2q+1)}$ for the first and second-order interpolation, respectively.

With $f_{\bar{\alpha}}(A)$ readily obtained, the hydrodynamic force $\mathbf{F}_{hydro}$ acting on a solid particle emerged in the fluid is calculated by summing up the loss of fluid momentum on all the links across the surface of the particle, namely,

$$\begin{aligned}
&\mathbf{F}_{hydro} \times \delta t \\
=&\text{loss of momentum of fluid} \\
=&\text{momentum before streaming - momentum after streaming} \\
=&\sum_{\text{all boundary links}} \left[\hat{f}_\alpha(\mathbf{x}, t)\mathbf{e}_\alpha - f_{\bar{\alpha}}(\mathbf{x}, t+\delta t)\mathbf{e}_{\bar{\alpha}}\right] \\
=&\sum_{\text{all boundary links}} \left[\hat{f}_\alpha(\mathbf{x}, t) + f_{\bar{\alpha}}(\mathbf{x}, t+\delta t)\right]\mathbf{e}_\alpha
\end{aligned} \tag{2.22}$$

This ensures the exact balance between the moment loss of the continuous fluid phase and the moment gain of the dispersed paticle phase, so that the total momentum of the particle-fluid system is conserved.

2.2 The Physalis Method

To validate the mesoscopic lattice Boltzmann approach and compare it with traditional Navier-Stokes based computational methods, we also developed independently a code using a macroscopic hybrid method proposed by Prof. Prosperetti and co-workers (Takagi *et al.*, 2003; Zhang and Prosperetti, 2003, 2005). The method was named *Physalis* (Takagi *et al.*, 2003). Physalis combines a numerical discrete representation of the Navier-Stokes viscous flow around particles and an analytical representation imbedded near the surface of each particle.

The basic idea behind Physalis is as follows. Because of the no-slip boundary conditions on its surface, a solid particle induces a specific local flow structure that could be used to linearize the Navier-Stokes equations in the neighborhood of the particle surface. The fluid velocity, pressure, and vorticity near the particle surface can be expressed analytically using series solutions of Stokes flow equations. As a result, the geometric surface of the particle can be replaced by a Stokes flow solution valid in a narrow but finite region near the surface, known as the cage region.

When the cage region is set up, there are three main components in the Physalis method. The first component is an analytical representation of the flow within the cage region. This is obtained by the method of separation of variables applied to Stokes flow equations. The general form in 2D is given in Zhang and Prosperetti (2003) and in 3D is found in Zhang and Prosperetti (2005) and Gao and Wang(2007). As the regular mesh extends to the interior of the particle surface, the velocity cage essentially defines an internal boundary for the viscous flow where the Stokes solution is employed to specify the boundary conditions there.

The second component is the numerical method for Navier-Stokes equations on a regular staggered mesh (the flow solver). The second-order project method (Brown *et al.*, 2001) is used. The intermediate velocity in the fractional step procedure is solved by a factorization method (Kim and Moin, 1985), while the Poisson equation for the projection step is solved by a combination of transformation and tridiagonal inversion.

The most essential component is the coupling between the numerical solution on the regular mesh and the Stokes solution in the cage region. This coupling is achieved by an iterative procedure in which (a) the numerical solution is used to refine the coefficients in the Stokes flow representation and in turn (b) the numerical solution is refined by an updated boundary conditions at the velocity cage from the refined Stokes flow.

An important advantage of this hybrid method is that the force and torque acting on the particle can be calculated directly from the Stokes solution, avoiding often tedious numerical integration of local viscous force on the particle surface that is

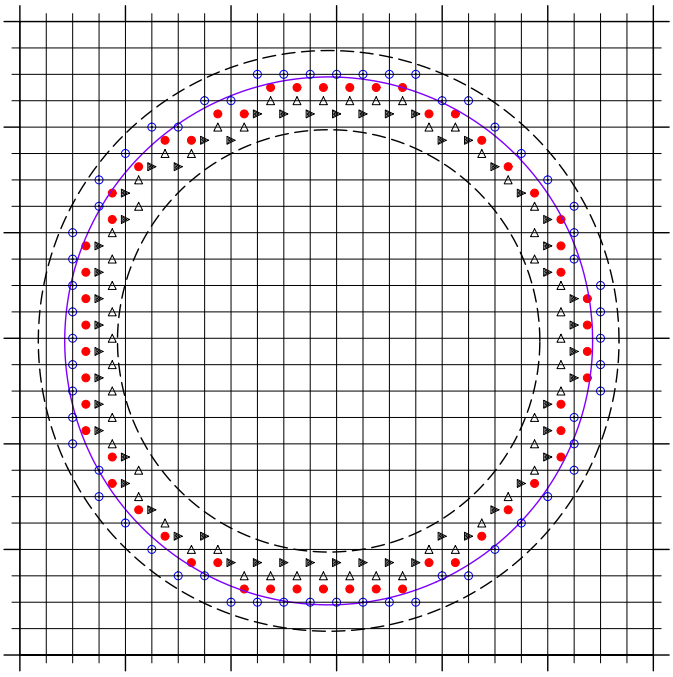

Figure 2.4: The cage used to represent a two-diemnsional glass bead in Physalis. Solid circles denote pressure cage nodes, open circles are vorticity cage nodes, filled triangles are u-velocity cage nodes, and open triangles are v-velocity cage nodes. The thick line denotes the glass bead surface. The two dash circles roughly indicate the scope of the cage region.

necessary for other non-hybrid numerical methods.

2.2.1 Cage Construction

The proper specification of the cage region and cage nodes requires a rather laborious effort, especially in three dimensions. Three types of cage nodes are defined, as shown in Figure 2.4 for 2D and Figure 2.5 for 3D: the pressure cage nodes located at cell centers, the velocity cage nodes at the centers of cell faces, and vorticity cage nodes at the centers of cell edges. The procedure for constructing the cage nodes and cage boundary is as follows.

First, the grid cell closest to the center of the glass bead is identified. A cubic

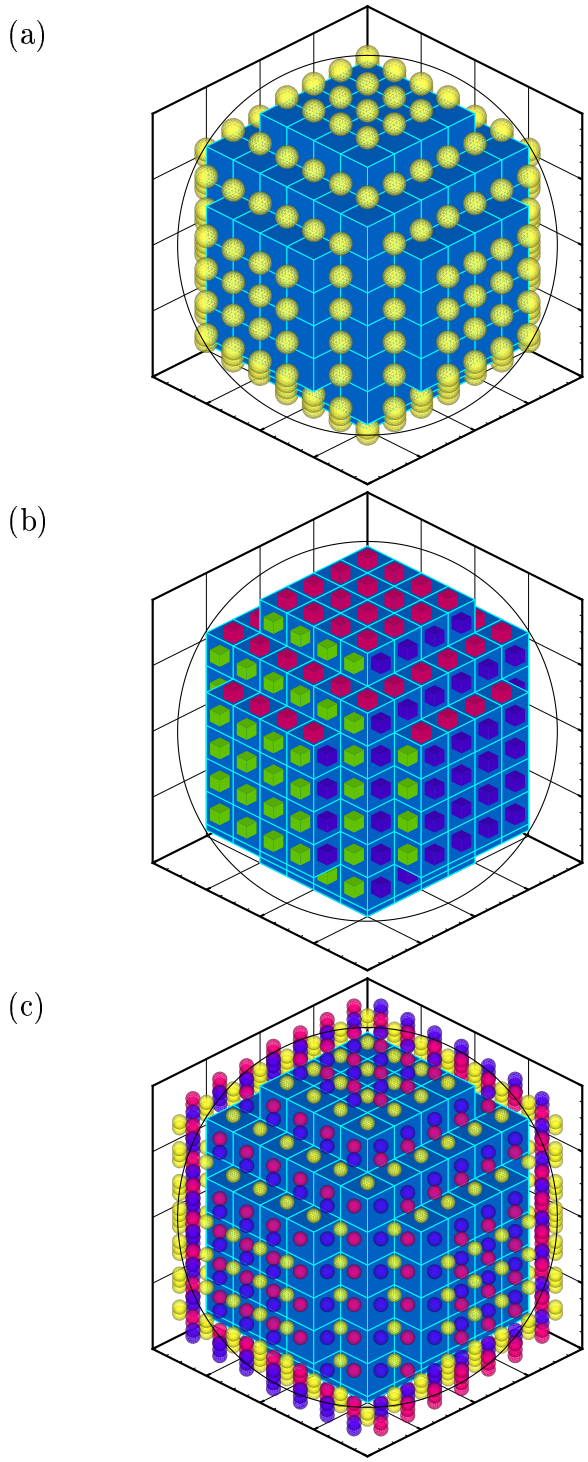

Figure 2.5: Illustration of various cage nodes for a spherical glass bead centered at (8,8,8) with radius equal to 5. (a) pressure cage nodes are marked as yellow spheres; (b) green, blue, and red cubes mark the location of velocity cage nodes in x, y, z directions, respectively; (c) red, blue, and yellow spheres mark the location of vorticity cage nodes in x, y, z directions, respectively. Blue membrane represents the internal velocity boundary for all cases.

box centered at this cell is built with a lateral length of $d_{bead} + 4\Delta x$, where d_{bead} is the diameter of the glass bead, and Δx is the grid spacing. The extra length of $4\Delta x$ is to ensure that all potential cage nodes around the bead's surface are contained in the box.

Second, all the nodes in the box are examined in terms of their center distance to the acutal surface of a glass bead. The pressure cage nodes are identified as the cells whose centers are immediately inside the actual surface of the glass bead, but have at least one adjacent cell outside the surface. Care were taken to pick only a minimum set of such cells as pressure cage nodes, so that a connected interior boundary can be formed by connecting interior cell faces of these connected cells. The spherical glass bead surface is then replaced by the cage interior surface, in other words, the fluid region is virtually extended into a glass bead to the cage interior boundary.

Third, the velocity cage nodes for all three velocity components are determined by using a combination of the boundary faces and cell surfaces that are normal to the interior boundary and immediately inside the interior boundary. These velocity cage nodes allow all fluid velocity nodes inside the extended fluid region to set up proper finite-difference equations according to the Navier-Stokes equation.

Finally, the vorticity cage nodes are defined on all the edges of the pressure cage cells that are not located on the interior cage boundary. By this construction procedure, the pressure and vorticity cages nodes are typically within one grid spacing from the physical surface of the glass bead.

While this procedure is described in Zhang and Prosperetti (2005), it took us a long time to set up the cage properly and validate the locations of the different types of cage nodes, in order to make sure that there is no hole in the cage region and there is no unnecessary redundancy.

2.2.2 Stokes Solution in the Particle Rest Frame

In this work, we consider viscous flows containing several spherical particles with translational velocity $\mathbf{w}(t)$ and angular velocity $\mathbf{\Omega}(t)$. The flow velocity $\mathbf{U}$ in the

inertial frame is related to its counterpart $\mathbf{u}$ in the non-inertial particle rest frame as

$$\mathbf{U} = \mathbf{u} + \mathbf{w} + \boldsymbol{\Omega} \times \mathbf{r} \tag{2.23}$$

where $\mathbf{r}$ is the position relative to the particle center. By applying Eq. (2.23), the momentum equation in the particle rest frame can be written as

$$\rho \left[\frac{\partial \mathbf{u}}{\partial t} + (\mathbf{u} \cdot \nabla)\mathbf{u} + 2\boldsymbol{\Omega} \times \mathbf{u} \right] = -\nabla p + \mu \nabla^2 \mathbf{u} + \rho \mathbf{g} - \rho \left[\dot{\mathbf{w}} + \dot{\boldsymbol{\Omega}} \times \mathbf{r} + \boldsymbol{\Omega} \times (\boldsymbol{\Omega} \times \mathbf{r}) \right] \tag{2.24}$$

where ρ and μ are the fluid density and viscosity, respectively, p is the pressure, $\mathbf{g}$ is the body force. The supercript '$\cdot$' denotes Lagrangian time derivative following the particle.

With the change of variables

$$\mathbf{u} = \tilde{\mathbf{u}} + \frac{r^5 - a^5}{10\nu r^3} \dot{\boldsymbol{\Omega}} \times \mathbf{r}, \qquad p = \tilde{p} + \frac{1}{2}\rho(\boldsymbol{\Omega} \times \mathbf{r})^2 + \rho(\mathbf{g} - \dot{\mathbf{w}}) \cdot \mathbf{r} \tag{2.25}$$

where $r = \|\mathbf{r}\|$, ν is the kinematic viscosity, and a is the particle radius, Eq. (2.24) then takes the form

$$\rho \left[\frac{\partial \mathbf{u}}{\partial t} + (\mathbf{u} \cdot \nabla)\mathbf{u} + 2\boldsymbol{\Omega} \times \mathbf{u} \right] = -\nabla \tilde{p} + \mu \nabla^2 \tilde{\mathbf{u}} \tag{2.26}$$

It is noted that $\mathbf{u} = 0$ on the particle surface. Therefore, by continuity, $\mathbf{u}$ is a small quantity near the particle surface, thus there exists a region near the particle where the left-hand side of Eq. (2.26) is small, such that it approximates the Stokes equation

$$-\nabla \tilde{p} + \mu \nabla^2 \tilde{\mathbf{u}} = 0, \qquad \nabla \cdot \tilde{\mathbf{u}} = 0 \tag{2.27}$$

As Reynolds number increases, the region contracts where Eq. (2.27) represents a good approximation to Eq. (2.26), but for any finite Reynolds number, the region is nonvanishing.

In presence of no-slip boundary on the particle surface, the solution of Eq. (2.27) in 3D can be found in Zhang and Prosperetti (2005). However, their paper contains several typos which have been corrected in our recent paper (Gao and Wang, 2007). It is

readily shown that the series solutions of Stokes equations consists of two components: the regular solid spherical harmonics and their corresponding singular harmonics. The regular harmonics represent the incident flow and the singular ones represent the disturbance induced by the particle. The final form of pressure, velocity , and vorticity field are expressed in spherical coordinates centered at the particle center, with dimensionless coefficients P_{nm}, $\tilde{P}_{nm}$, Φ_{nm},$\tilde{\Phi}_{nm}$,X_{nm},$\tilde{X}_{nm}$, and associated Legendre functions P_n^m. Detailed formulae for $\tilde{p}$, $\tilde{\mathbf{u}}$, and $\tilde{\omega}$ are given in Appendix A.

It is noted that the force and torque acting on each particle can be found directly from the low-order dimensionless coefficients associated with the Stokes solution. In the inertial frame, the hydrodynamic force and torque on the particle are written as

$$\mathbf{F}_{hd} = \rho v(\dot{\mathbf{w}} - \mathbf{g}) + \pi\mu\nu(P_{11} + 6\Phi_{11}, \tilde{P}_{11} + 6\tilde{\Phi}_{11}, P_{10} + 6\Phi_{10}), \tag{2.28}$$

$$\mathbf{L}_{hd} = \rho v a^2 \dot{\mathbf{\Omega}} + 8\pi\mu\nu a(X_{11}, \tilde{X}_{11}, X_{10}), \tag{2.29}$$

where v is the volume of the particle. In this way, one avoids the difficulty of high-order extrapolations to obtain the stress distribution on the particle surface that is typically encountered with other numerical methods.

2.2.3 Coupling Procedure

With the local flow structure expressed by the analytical solution of the Stokes equations, it can now be used to transfer the no-slip condition from the particle surface to the adjacent grid nodes. In this way, the physical boundary of the particle, which usually represents a complex geometry to the underlying regular mesh, is relplaced by a simpler boundary consisting of grid nodes. The non-local effect of the presence of particles on the flow fields is then imposed by matching the local analytical solution to the global numerical solution in an iterative manner.

The coupling procedure between the local and global fields is as follows. Suppose a provisional estimate of velocity and pressure fields is available, e.g., from the results obtained at previous time step, the auxiliary fields $\tilde{p}$ and $\tilde{\mathbf{u}}$ defined in Eq. (2.25) can be

calculated. The vorticity field is then found by discretizing $\tilde{\omega} = \nabla \times \tilde{\mathbf{u}}$ on a standard staggered grid arrangement.

Next, the provisional values of $\tilde{p}$ and $\tilde{\omega}$ are matched to the analytic expression (as shown Appendix A) on the cage nodes, yielding a linear system for the coefficients $(P_{nm}, \tilde{P}_{nm})$, $(\Phi_{nm}, \tilde{\Phi}_{nm})$, and $(X_{nm}, \tilde{X}_{nm})$. Truncation of the series solution to a finite number of order $n = N_c$ retains a total of $3N_c(N_c + 2) + 1$ coefficients, while there are about $4 \times (4\pi a^2/\Delta x^2)$ pressure and vorticity cage nodes, where a is the particle radius and Δx the grid spacing. Therefore, the matching operation gives rise to a linear system of approximately $4 \times (4\pi a^2/\Delta x^2)$ equations and $3N_c(N_c + 2) + 1$ unknowns. This rectangular matrix system with many more rows than columns is solved in a least square sense by applying the singular value decomposition algorithm.

Using the values of coefficients determined at previous step, one can now compute the provisional velocity $\tilde{\mathbf{u}}$ from the analytic formula (see Appendix A) at the velocity cage nodes, and subsequently find the values of $\mathbf{u}$ in the particle rest frame and $\mathbf{U}$ in the inertial frame from Eq. (2.25) and Eq. (2.23), respectively. The full Navier-Stokes equations is then solved on the finite-difference grid over the entire domain, with the new velocity field $\mathbf{U}$ imposed as boundary conditions on the velocity cage nodes of each particle. After that, the pressure and velocity field resulting from the flow solver can be used to determine the new provisional values of $\tilde{p}$ and $\tilde{\omega}$, which starts another iteration as above-mentioned. This procedure repeats until convergence is achieved.

It is noted that a fast flow solver is applied in the iterative procedure over the entire grid, without differentiating the fields outside and inside the cages. Thus the resultant flow field can be decomposed into two parts: one is the velocity field outside the cage, which is desired; the other is inside the cage, which is driven by the imposed velocity boundary conditions on the cage nodes. Although the two parts share the common velocity on the cage nodes, the inside solution is completely irrelated to the outside one, so that it can be disregarded. The final flow field is given by the finite difference solution outside the cages and the analytic representation in the thin region

between the actual particle surface and their surrounding cage.

2.2.4 Numerical Solution and Flow Solver

As described in the previous section, during each time step t^n, the analytic solution is reconciled to the finite difference solution in an iterative procedure, so that the non-local effect of the particle is embodied in the global field. The numerical solution is obtained by adopting a second-order projection method (Brown *et al.*, 2001) which is modified to suit our present purposes.

Using a two-step time-advancement scheme, the Navier-Stokes equations for the incompressible viscous flows can be written as

$$\frac{\mathbf{u}^* - \mathbf{u}^n}{\Delta t} = -\left(\frac{\nabla p}{\rho}\right)^k + \left(\frac{3}{2}\mathbf{H}^k - \frac{1}{2}\mathbf{H}^{n-1}\right) + \frac{\nu}{2}\left(\nabla^2\mathbf{u}^n + \nabla^2\mathbf{u}^*\right), \tag{2.30}$$

$$\frac{\mathbf{u}^{k+1} - \mathbf{u}^*}{\Delta t} = -\nabla\phi^{k+1} \tag{2.31}$$

with

$$\nabla \cdot \mathbf{u}^{k+1} = 0. \tag{2.32}$$

where $\mathbf{H} = (\mathbf{u} \cdot \nabla)\mathbf{u}$ is the convective term, ϕ is a scalar related to pressure, and superscript k is the counter for iteration. Here we use the second-order explicit Adams-Bashforth scheme for the convective term, and the second-order implicit Crank-Nicholson scheme for the viscous term. All the spatial derivatives are approximated with second-order central differences on a staggered grid. Specifically, at the cage nodes, the velocity obtained from the analytic solution are imposed directly on $\mathbf{u}^*$ using the most recently updated values of the coefficients.

Following the fractional step method by Kim and Moin (1985), Eq. (2.30) can be rewritten as

$$(1 - A_1 - A_2 - A_3)(\mathbf{u}^* - \mathbf{u}^n) = -\left(\frac{\nabla p}{\rho}\right)^k \Delta t + \frac{\Delta t}{2}\left(3\mathbf{H}^k - \mathbf{H}^{n-1}\right) + 2(A_1 + A_2 + A_3)\mathbf{u}^n \tag{2.33}$$

where $A_1 = (\nu\Delta t/2)(\delta^2/\delta x_1^2)$, $A_2 = (\nu\Delta t/2)(\delta^2/\delta x_2^2)$, $A_3 = (\nu\Delta t/2)(\delta^2/\delta x_3^2)$. Performing factorization on the left-hand side of Eq. (2.33) gives

$$(1-A_1)(1-A_2)(1-A_3)(\mathbf{u}^*-\mathbf{u}^n) = -\left(\frac{\nabla p}{\rho}\right)^k \Delta t + \frac{\Delta t}{2}\left(3\mathbf{H}^k - \mathbf{H}^{n-1}\right) + 2(A_1+A_2+A_3)\mathbf{u}^n \tag{2.34}$$

which represents an $\mathcal{O}(\Delta t^3)$ approximation of Eq. (2.33). However, Eq. (2.34) requires inversions of tridiagonal matrices rather than inversion of a large sparse matrix, as in the case of Eq. (2.33). In this way the computational efficiency is significantly increased.

With the intermediate velocity $\mathbf{u}^*$ readily obtained from Eq. (2.34), Eq. (2.31) and (2.32) can be solved as a coupled system for $\mathbf{u}^{k+1}$ and ϕ^{k+1}, which satisfies

$$\nabla^2\phi^{k+1} = \frac{\nabla\cdot\mathbf{u}^*}{\Delta t} \tag{2.35}$$

Note that at the interior boundary on the cage nodes, the zero-normal-gradient condition is required, namely,

$$\mathbf{n}_c\cdot\nabla\phi^{k+1} = 0, \tag{2.36}$$

where $\mathbf{n}_c$ is the unit normal pointing outward from the cage. To enforce Eq. (2.36), a deferred-correction term is added to the right-hand side of Eq. (2.35). For instance, at a velocity cage node in the $x-$direction, Eq. (2.35) is modified as

$$\frac{1}{\Delta x}\left(\frac{\phi^{k+1}_{i+1,j,k}-\phi^{k+1}_{i,j,k}}{\Delta x} - \frac{\phi^{k+1}_{i,j,k}-\phi^{k+1}_{i-1,j,k}}{\Delta x}\right) + \cdots = \frac{\nabla\cdot\mathbf{u}^*}{\Delta t} + \frac{\phi^k_{i+1,j,k}-\phi^k_{i,j,k}}{(\Delta x)^2}, \tag{2.37}$$

where the dots in the left-hand side stand for the remaining terms of the discretized Laplacian. At convergence, the extra term $(\phi^k_{i+1,j,k}-\phi^k_{i,j,k})/(\Delta x)^2$ in the right-hand side cancels the term $(\phi^{k+1}_{i+1,j,k}-\phi^{k+1}_{i,j,k})/(\Delta x)^2$ in the left-hand side. In this way the Laplacian form is maintained over the entire domain, without the necessity of singling out the cage nodes as interior boundaries. This feature enables the use of a fast Poisson solver combining transformation and tridiagonal inversion for Eq. (2.35).

At the end of the iteration, the pressure is given by

$$\left(\frac{p}{\rho}\right)^{k+1} = \left(\frac{p}{\rho}\right)^k + \phi^{k+1} - \frac{\nu\Delta t}{2}\nabla^2\phi, \tag{2.38}$$

and the velocity is calculated as

$$\mathbf{u}^{k+1} = \mathbf{u}^* - \Delta t \nabla \phi^{k+1}. \tag{2.39}$$

After convergence, the position $\mathbf{y}$, translational velocity $\mathbf{w}$, and angular velocity $\mathbf{\Omega}$ of each particle are updated from

$$\mathbf{w}^{n+1} = \mathbf{w}^n + \frac{\Delta t}{2m}\left(\mathbf{F}_{hd}^{n+1} + \mathbf{F}_{hd}^{n} + \mathbf{F}_{ext}^{n+1} + \mathbf{F}_{ext}^{n}\right), \tag{2.40}$$

$$\mathbf{y}^{n+1} = \mathbf{y}^n + \frac{\Delta t}{2}\left(\mathbf{w}^{n+1} + \mathbf{w}^{n}\right), \tag{2.41}$$

$$\mathbf{\Omega}^{n+1} = \mathbf{\Omega}^n + \frac{\Delta t}{2I}\left(\mathbf{L}_{hd}^{n+1} + \mathbf{L}_{hd}^{n} + \mathbf{L}_{ext}^{n+1} + \mathbf{L}_{ext}^{n}\right), \tag{2.42}$$

where m and I are the particle mass and moment of inertia, $\mathbf{F}_{ext}$ and $\mathbf{L}_{ext}$ are the external force and couple other than their hydrodynamic counterparts, respectively.

2.3 Cross-Validation: Settling of Two Spherical Particles

In this section, we present results from simulations involving gravitational sedimentation of two spherical particles using both the MRT LBE model and the Physalis method. The purpose is to demonstrate the two methods' capability in simulating particle-resolved viscous flows, and to cross-validate our implementation of the two codes.

Here we consider two solid particles that are allowed to fall along the centerline of a square channel under gravity. Similar problems have been studied intensively by several researchers (Glowinski *et al.*, 1999, 2001; Patankar *et al.*, 2000; Singh *et al.*, 2000, 2003; Zhang and Prosperetti, 2003; Apte *et al.*, 2009) and the concomitant "drafting, kissing, and tumbling" phenomenon is well-documented. In our simulation, the channel has equal width and height $W = H = 12a$, and length $L = 80a$. The particles have a radius of $a = 1mm$ and are released at distances $76a$ and $72a$ above the bottom of the domain. Initially, the lower particle is located exactly on the centerline of the channel, while the higher one slightly deviates from the centerline with a distance

of $10^{-2}a$ in the $x-$direction. This setup is to disturb the symmetric flow under low Reynolds number, and thus to prompt the particles to drift away from each other during sedimentation. The liquid density and kinematic viscosity are $\rho_l = 1000kg/m^3$ and $\nu_l = 1.0 \times 10^{-6}m^2/s$, and the particle density $\rho_p = 1010kg/m^3$. Gravitational accelaration is $g = 9.8m/s^2$ in the $y-$direction. In both LBM and Physalis simulation, the particle diameter is set to $2a/\Delta x = 20$. No-slip boundary conditions are imposed on all the side walls of the channel and on the particle surfaces. Neumann bondary conditions are set at top and bottom of the domain, specifying zero velocity derivatives in $y-$direction.

When the two particles are in close contact, the physical lubrication forces between the particles are under-estimated due to lack of resolution of the flow. In order to prevent the particles from overlapping, a pair-wise repulsive force is introduced acting on the ith particle due to its interaction with jth particle (Glowinski *et al.*, 2001; Feng and Michaelides, 2005):

$$\mathbf{F}_{ij} = \begin{cases} 0, & r_{ij} > 2a + \zeta \\ \dfrac{c_{ij}}{\varepsilon_p}\left(\dfrac{r_{ij} - 2a - \zeta}{\zeta}\right)^2 \left(\dfrac{\mathbf{r}_{ij}}{r_{ij}}\right), & r_{ij} \leq 2a + \zeta \end{cases} \tag{2.43}$$

where $r_{ij} = \|\mathbf{y}_i - \mathbf{y}_j\|$ is the distance between the particle centers, ζ is the thickness of a buffer zone within which the model repulsive force becomes active, c_{ij} is a force scale, and ε_p is a stiffness parameter. In this work, ζ is set as two grid (lattice) spacing, and ε_p is set to be small enough to prevent particle collision.

Figure 2.6 shows the particle position and angular displacement at different times, and Figure 2.7 illustrates the velocity vectors near the particles on a plane-cut through the particle centers at corresponding time moments. The "drafting, kissing, and tumbling" phenomenon is clearly visible. The higher particle gets caught in the low pressure wake of the lower particle, thus accelerates and catches up with the lower one (drafting). The two particles then fall with nearly the same velocity (kissing) until they tumble and separate due to the unstable nature of the flow.

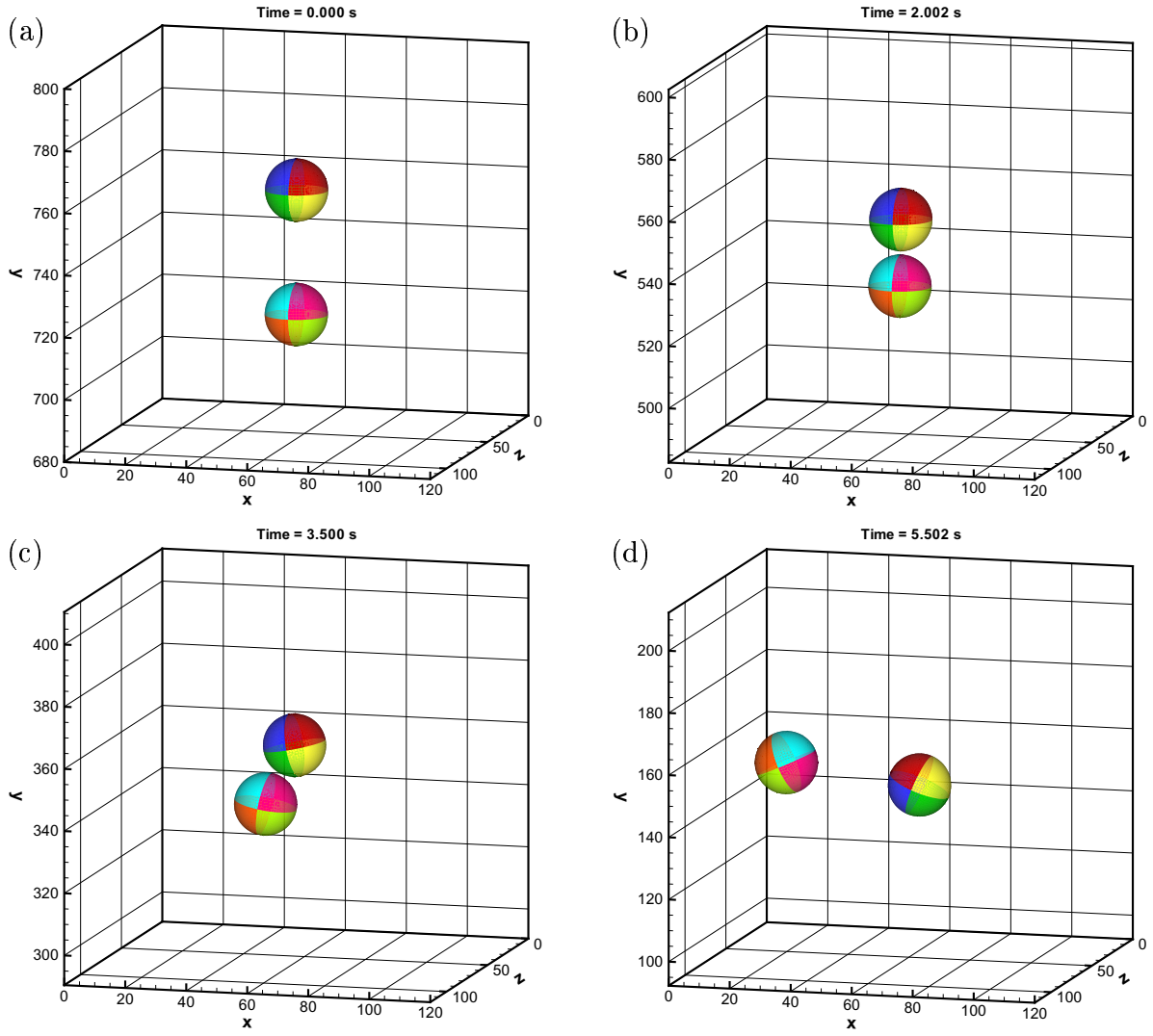

Figure 2.6: Snapshots of particle location and angular displacement of the two settling spheres at times (a) $t = 0.0s$, (b) $t = 2.0s$, (c) $t = 3.5s$, and (d) $t = 5.5s$.

Figure 2.8 shows the time evolution of the translational velocities and center location for each particle. The results from LBM are in good agreement with those from Physalis method. This cross-validates our particle-resolved simulation codes developed from the two fundamentally different methods. Qualitative agreement is also achieved by comparing present results with those reported by Glowinski *et al.* (2001), though some quantitative differences are observed. This can be addressed as follows. Ideally, the two falling particles would remain aligned and indefinitely approach each

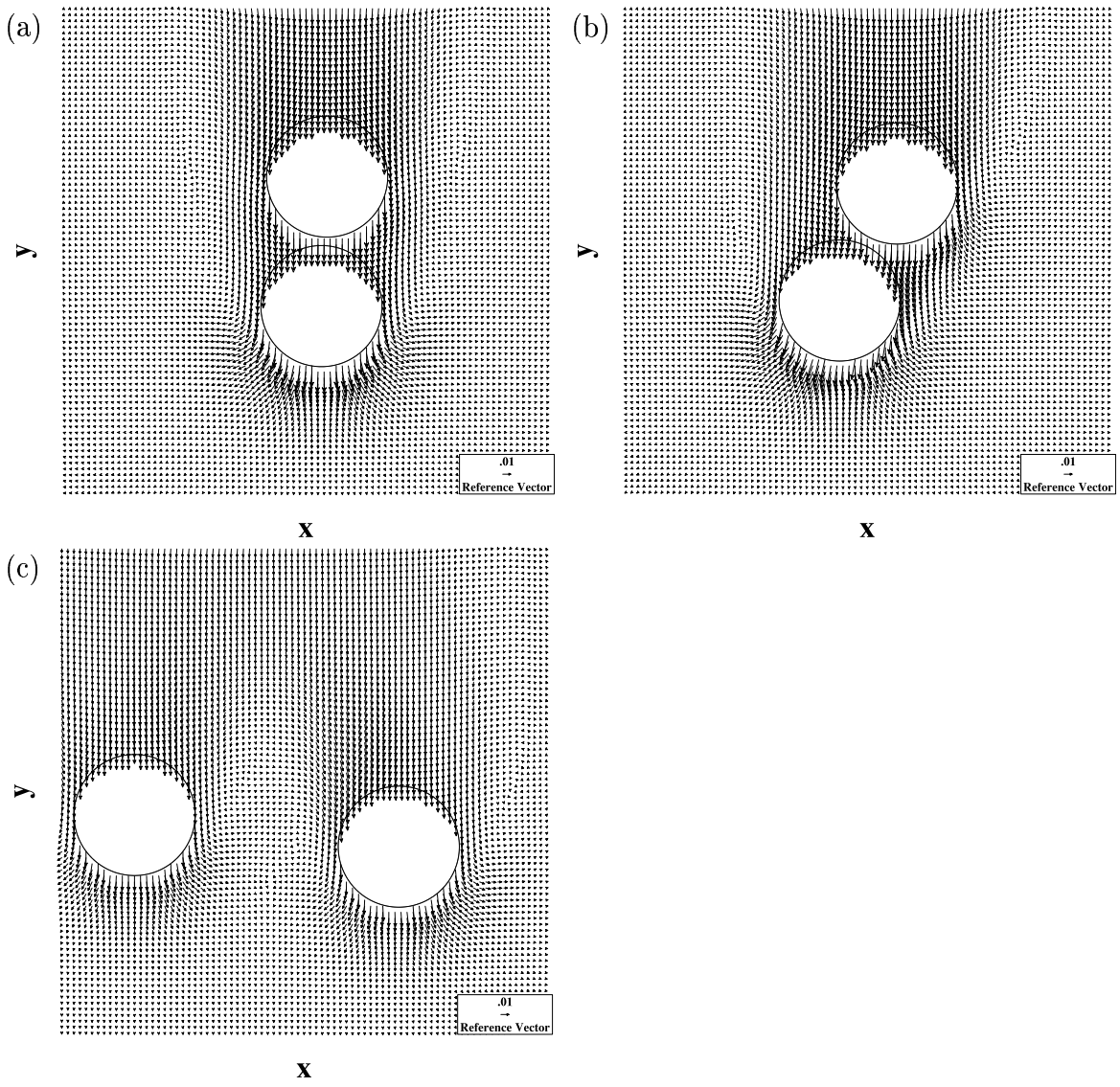

Figure 2.7: Snapshots of velocity vectors near the particles on a plane-cut through the centers of the two settling spheres at times (a) $t = 2.0s$, (b) $t = 3.5s$, and (c) $t = 5.5s$.

other without ever touching, if mathematically smooth particles and infinite numerical precision are applied. In the numerical simulation, however, due to the finite time step, it is necessary to introduce an artificial repulsive force to prevent the particle collision. Depending on how the repulsion force is specified and on the details of the numerics, the results may vary widely. In other words, the motion of the spheres and the "drafting, kissing, tumbling" process are sensitive to the collision model and the

numerical disturbance present in the simulation method.

Another point worth notifying is that LBM appears less susceptible to numerical perturbations compared with Physalis method, as shown in Figure 2.8(c) and (f). As desired, LBM results show that particle traverse velocity in $z-$direction is very close to zero, consequently the particle center location remains unchanged in $z-$direction. In contrast, the Physalis results in $z-$direction depart from the desired values with discernible magnitude, though the difference is still negligible if compared with the values in $x-$ and $y-$directions. The better accuracy in LBM can be partly attributed the local treatment of moment change between the fluid and particle, which is not only simpler in implementation but also more accurate than the global treatment in Physalis via coupling the analytic Stokes solution around particle surface with the numerical solution resolved in rest of the fluid domain.

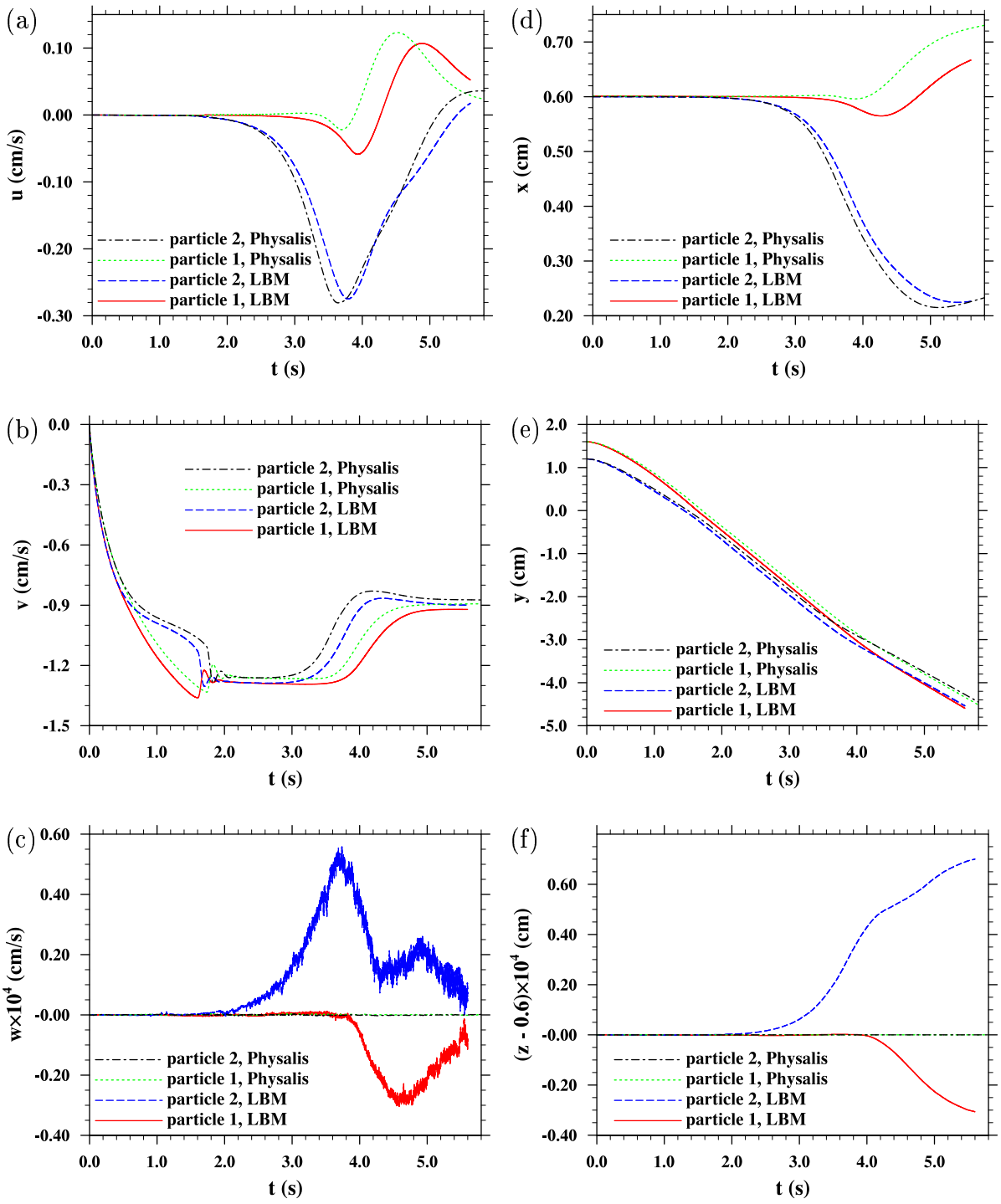

Figure 2.8: Temporal evolution of particle velocity and location by both LBM and Physalis method: (a,b,c) velocity component in $x-$, $y-$, and $z-$direction, respectively; (d,e,f) particle center location in $x-$, $y-$, and $z-$direction, respectively. Note the seemingly large difference in $z-$direction is indeed negligible as the magnitude of the difference is extremely small compared with that in the other directions.

Chapter 3

THREE-DIMENSIONAL MICROSCALE FLOW SIMULATION AND COLLOID TRANSPORT MODELING IN SATURATED SOIL POROUS MEDIA

Transport of sub-micron colloid particles in soil porous media has been mostly studied numerically with unit-cell-based grain-scale geometries. In this chapter, we develop a more general approach by combining a multiple-grain pore-scale flow simulation with Lagrangian tracking of individual colloids. First, two numerical methods are applied simultaneously to solve viscous flows in a channel partially or fully packed with spherical grain particles, this allows cross-validation of the numerical methods for considered model geometries. It is demonstrated that the mesoscopic lattice Boltzmann approach can more accurately simulate three-dimensional pore-scale flows with multiple grain-grain and grain-wall contact points. Colloid transport is simulated under the combined influence of hydrodynamic forces, Brownian force, and physicochemical forces. Preliminary results demonstrate the capture of colloids by the secondary energy minimum (SEM) well. The local hydrodynamic retardation is shown to reduce the ability for colloids to move into the SEM well, but does not prevent this. Trajectories before and after the capture are also discussed.

3.1 Introduction

The attachment of colloids on grain surface and retention of colloids in small soil pores and their subsequent release when the solution or hydrodynamic conditions change determine the distribution and penetration of colloids in groundwater, and are important topics to groundwater contamination and remediation treatments. Most previous studies on colloid retention and transport address issues such as breakthrough

curves at the macroscopic column scale. Research in recent years at the soil grain scale reveals that the retention and release depend on the competing effects of physicochemical and hydrodynamic forces acting on the colloids (Bradford *et al.*, 2007; Johnson *et al.*, 2007; Shen *et al.*, 2007), indicating a need to better understand and model pore-scale flow in realistic three-dimensional (3D) porous media, particularly under unfavorable conditions as commonly encountered in natural porous media. Additionally, pore geometry affects local flow distribution and can contribute significantly to colloid retention. Important 3D flow features such as large local variations of flow velocity magnitude, direction, and shear rate depend on both grain-grain relative configuration and grain surface heterogeneity.

While the overall objective of our research is to develop an integrated experimental and computational approach focusing on pore-scale processes related to colloid transport (Gao *et al.*, 2008; Qiu *et al.*, 2012), here we focus on developing a computational method to simulate the interaction of colloids with pore-scale flow and grain surfaces under various physicochemical and hydrodynamic conditions. In general, there are two components to pore-scale computational modeling: simulation of liquid flow and simulation of transport of colloids by the liquid flow and interactions of colloid with grain surfaces. The second part could be performed in either an Eulerian or a Lagrangian fashion.

Limited by its mean-field nature, the Eulerian approach requires a closure assumption of the driving source/sink terms in the advection-dispersion equation, thus may not be applicable to unfavorable conditions. In contrast, the Lagrangian approach focuses on a single colloid and tracks its position and velocity over time, providing a more direct mechanistic description of microscopic colloid transport. The equation of motion for colloids can be easily modified to include colloidal force and other forces that act over a vast range of characteristic lengths, which makes it much more feasible to include complex interactions with grain surface. Therefore, most mechanistic modeling studies adopt the Lagrangian trajectory approach.

Under the Lagrangian trajectory approach, unit-cell-based flow representation

were typically employed to solve the liquid flow in porous media due to its computational efficiency. However, this approach does not take full account of grain-grain contact and grain surface irregularities. Previous studies have indicated the need to solve viscous flows through pore domains rendered from actual porous media, in order for such approach to become a useful quantitative tool.

Here we intend to study colloid transport and retention involving multiple grain-grain and grain-wall contacts in a model porous channel. To accurately simulate the pore-scale viscous flow, both the mesoscopic lattice Boltzmann method (LBM) and a Navier-Stokes-based hybrid method (i.e., Physalis) (Zhang and Prosperetti, 2005; Gao and Wang, 2007) are applied to the same 3D flow configurations. The first part of this study concerns inter-comparison of simulated 3D viscous flows in a channel. This extends the previous unit-cell flow representations. Simultaneous applications of two numerical methods provide a cross-validation step for simulating flows in the considered model geometry. Such inter-comparison has been performed recently for 2D pore-scale viscous flows by Gao *et al.* (2008).

We then present a preliminary study of colloid transport in a simulated porous channel packed with 25 spherical grain particles (or glass beads). A preliminary study in 2D without considering local hydrodynamic interaction showed that the retention rate of colloids depends on both the mean flow speed and solution ionic strength (Gao*et al.*, 2008). Here we will extend our previous work to include local hydrodynamic interactions and 3D flow effects to more realistically model colloid transport and retention.

3.2 Flow Simulation

In this section, we first briefly introduce the two numerical methods for solving viscous flows in complex geometries. Several benchmark cases are then used to compare the results from the two methods. The general problem to be solved is flow through a three-dimensional channel with fixed spherical grain particles occupying part of the channel.

3.2.1 The Mesoscopic Lattice Boltzmann Approach

The mesoscopic approach is based on a lattice Boltzmann equation with the multiple-relaxation-time (MRT) collision model using 19 discrete particle velocities in three dimensions (*i.e.*, the D3Q19 model), as described in detail in d'Humières *et al.* (2002) and Chapter 2 of this dissertation. In the MRT-LBM, the evolution equation for the discrete particle density distribution function, f_i, for $i = 0,\ 1,\ 2, \ldots, 18$, is written as

$$f_i(\mathbf{x} + \mathbf{e}_i\delta_t, t + \delta_t) = f_i(\mathbf{x}, t) - M_{ij}^{-1} S_{jk} \left[m_k - m_k^{(\mathrm{eq})} \right] + \psi_i(\mathbf{x}, t), \tag{3.1}$$

where the collision operation is performed in a properly defined moment space through the transform matrix M_{ij} of rank 19×19, namely,

$$m_i = M_{ij} f_j, \qquad f_i = M_{ij}^{-1} m_j. \tag{3.2}$$

The detail of the transform matrix M_{ij} is given in Eq. (2.16). By construction, the inverse matrix M^{-1} can be easily obtained by the transpose of M_{ij} with a renormalization as the product of M_{ij} and its transpose yields a diagonal matrix. In Eq. (3.1), ψ_i is a prescribed forcing field designed to model the driving pressure gradient or body force. In this work, ψ_i is specified as $\psi_i(\mathbf{x}, t) = \mathbf{e}_i \cdot \mathbf{F}_B/10$, where $\mathbf{F}_B$ is the macroscopic force per unit volume acting on the fluid. This forcing implementation is rather simple and does not explicitly consider the potential lattice effects associated with forcing, which has been described in Guo *et al.* (2002). Since the forcing field is a constant pressure gradient, there is no lattice effect (Wang and Afsharpoya, 2006). The correct specification of the forcing function in the mesoscopic space for a general non-uniform time-dependent physical-space forcing has been discussed in detail in Wang *et al.* (2013). The 19 discrete velocities in the D3Q19 model are ordered as

$$\mathbf{e}_i = \begin{cases} (0,0,0), & i = 0, \\ (\pm 1,0,0), (0,\pm 1,0), (0,0,\pm 1), & i = 1 \text{ to } 6, \\ (\pm 1,\pm 1,0), (\pm 1,0,\pm 1), (0,\pm 1,\pm 1), & i = 7 \text{ to } 18. \end{cases} \tag{3.3}$$

Specifically, the moment vector m_i contains four conserved elements, the density fluctuation $\delta\rho = \rho - \rho_0 = m_0$ and the flow momentum $(\rho_0 u_x, \rho_0 u_y, \rho_0 u_z) = (m_3, m_5, m_7)$. These conserved moments and the pressure field are calculated from f_i as

$$\delta\rho = \sum_i f_i, \;\; \rho_0 \mathbf{u} = \sum_i f_i \mathbf{e}_i, \;\; p = \delta\rho c_s^2, \tag{3.4}$$

where $\mathbf{u}$ is macroscopic fluid velocity, the sound speed c_s is $1/\sqrt{3}$, and the mean density ρ_0 is set to 1.0. The use of the density fluctuation instead of the total density in the above reduces the round-off error. The equilibria of all the non-conserved moments are related to $\delta\rho$ and $\rho_0\mathbf{u}$ (d'Humières *et al.* 2002). The diagonal matrix $S = diag(s_0, s_1, ..., s_{18})$ specifies the relaxation rates of the non-conserved moments towards their respective equilibrium. The specific values used here are $s_0 = s_3 = s_5 = s_7 = 0$, $s_1 = 1.19$, $s_2 = s_{10} = s_{12} = 1.4$, $s_4 = s_6 = s_8 = 1.2$, $s_{16} = s_{17} = s_{18} = 1.98$, $s_9 = s_{11} = s_{13} = s_{14} = s_{15} = 1/(3\nu + 0.5)$, where ν is the kinematic fluid viscosity. Other details of the MRT-LBM model can be found in Chapter 2. It should be noted that the previous single-relaxation-time LBGK model is recovered when all the relaxation rates are set to a same value. Recently, Ginzburg *et al.* (2008a and 2008b) have developed a two-relaxation-time (TRT) LBM approach that is more efficient and suitable for viscous flow through porous media. This TRT-LBM could be used to find suitable choice of the various relaxation rates. The MRT-LBM has been shown to improve numerical stability at higher flow Reynolds numbers (d'Humières *et al.*, 2002). In our previous 2D pore-scale flow simulations (Gao *et al.*, 2008), we found that MRT-LBM yields a more robust steady-state viscous flow solution for a wider range of relaxation parameter (or viscosity setting), when compared to the usual LBGK collision model.

A uniform cubic lattice is used to cover the computational domain. The straight channel walls are located in the middle of lattice links so a second-order accuracy is achieved with a simple mid-link bounce-back implementation. The inlet and outlet are also located half way on the lattice links to facilitate the implementation of the periodic boundary condition in the bulk flow direction.

The key implementation issue here is the treatment of solid particle surfaces. For each lattice node near a particle surface, we identify all links moving into the surface and their relative boundary-cutting location, namely, the percentage (q) of a link located outside the surface. Since particles are fixed, this information is pre-processed before the flow evolution. Before the streaming step, the missing population is properly interpolated in terms of q and two populations lying before and after the path of the missing population (Lallemand and Luo, 2003a; Yu *et al.*, 2003). For results in this paper, we used the first-order interpolation based on two known populations, and found that the results are quite similar to the second-order interpolation based on three nodes (Lallemand and Luo, 2003a). The above simple interpolated bounce-back treatment represents a great advantage of LBM over traditional CFD approach. It handles complex boundary geometry using local lattice-link operations. All lattice nodes lying within the solid particles (including the fluid-solid interface) are excluded from LBE evolution, their velocities are simply set to the values according to solid body translation and rotation, for the purpose of field energy spectrum or to zero for the visualizations of the fluid flow. As a validation check, the total mass for the fluid nodes (excluding the fluid-solid interface nodes) is computed and found to essentially remain constant as time is advanced.

Another issue with the bounce-back interpolation is that two fluid lattice nodes may not be available when glass beads are in contact with one another or with channel walls. In this case, a simple one-node bounce back is used instead. This does not cause much problem as the fluid velocity near a contact point in such a case is typically very small.

3.2.2 The Macroscopic Hybrid Approach: Physalis

To validate the mesoscopic LBM-MRT method, the same flow problems are also solved by a macroscopic Navier-Stokes-based hybrid approach (*i.e.*, Physalis) developed by Prof. Prosperetti and co-workers (Zhang and Prosperetti, 2003, 2005). The basic idea for Physalis is to combine an analytical Stokes flow representation valid near the

surface of each spherical glass bead and the finite-difference numerical solution on the computational grid. Because of the no-slip boundary conditions on the surface, a glass bead induces a specific local flow structure that could be used to linearize the Navier-Stokes equations in the neighborhood of the glass-bead surface. The fluid velocity, pressure, and vorticity near the particle surface can be expressed analytically using series solutions of Stokes flow equations. As a result, the geometric surface of the particle can be replaced by a Stokes flow solution valid in a narrow but finite region near the surface, known as the cage region.

The proper specification of the cage region and cage nodes requires considerable effort, especially for the 3D case. Here we shall briefly describe the major elements of the procedure. More details can be referred to Chapter 2. For the cage region, three types of cage nodes are defined, including the pressure cage nodes, velocity cage nodes, and vorticity cage nodes. The pressure cage nodes are first defined at cell centers by identifying all cells whose centers are immediately inside the actual surface of a glass bead. A minimum set of such connected cells form the pressure cage nodes. Meanwhile, an interior boundary is specified by connecting interior cell faces of these connected cells. The spherical glass-bead surface is then replaced by the cage interior surface. Second, the velocity cage nodes for all three velocity components are determined at centers of cell faces by using a combination of the boundary faces and cell surfaces that are normal to the interior boundary and immediately inside the interior boundary. Finally, the vorticity cage nodes are defined on all the centers of the cell edges of the pressure cage nodes that are not located on the interior cage boundary.

The fact that the pressure cage nodes are located completely inside the glass bead has the advantage of handling physical contact of two or more glass beads or contact of a glass bead with a channel wall. Care is taken to make sure that no pressure or vorticity cage nodes from one glass bead are located in the interior of another glass bead or channel wall. Since currently a separate analytical Stokes flow must be constructed for each glass-bead surface, the method is not ideal for solving flow in a porous channel packed with many glass beads.

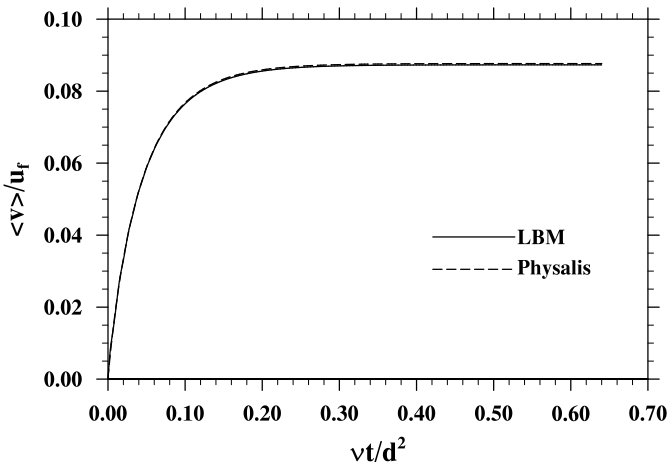

Figure 3.1: The time evolution of mean velocity in the y direction, normalized by u_f, for $s = 9$.

Upon construction of the cage region, three major components are involved in the Physalis methods. These are (1) the analytical representation of the flow within the cage region, (2) the numerical solution outside the cage region, and (3) the coupling of the two. More details can be found in Chapter 2 on the analytical solution, the numerical flow solver, and their coupling procedure.

Overall, from the viewpoint of computer code implementation, the treatment of glass-bead surfaces in this macroscopic hybrid method is much more complex than the local interpolated bounce-back scheme in the LBM. As will be demonstrated in the next section, the accuracy of Physalis is deteriorated when many glass beads are in contact with one another or with channel walls.

3.2.3 Inter-Comparison of the Two Approaches: Viscous Flows in a 3D Porous Channel

Our first goal is to ensure that the viscous flow in a 3D porous channel is accurately solved. This is achieved by establishing a good quantitative comparison between the results from LBM and Physalis. The inter-comparison of the two numerical methods includes the mean flow rate, local velocity profiles, as well as forces and torques acting on glass beads.

To proceed in a systematic manner, we consider three geometric settings below. In all cases, the y direction is the mean flow direction with a periodic length L so the computation domain covers $0 \leq y \leq L$. The channel cross-section has a width H in the x direction and a height W in the z direction. so $0 \leq x \leq H$ and $0 \leq z \leq W$. The body force $\mathbf{F}_B$ per unit volume used to drive the flow is expressed as $8\mu u_f/W^2$, where μ is the fluid dynamic viscosity and u_f is a characteristic fluid velocity if there were no glass beads in the channel.

3.2.3.1 Single Glass Bead in a Square Channel

The first general case involves a single fixed glass bead in the square channel of radius R. In terms of the grid spacing δ, $H = 100\delta$, $L = 80\delta$, $W = 80\delta$, and $R = 25\delta$. The center of the glass bead is located at $x = 42\delta$, $y = 40\delta$, and $Z = R + s\delta$, where s is a nearest gap distance between the glass-bead surface and the channel wall normalized by δ.

The Reynolds number based on u_f is $Du_f/\nu = 2.5$ ($D = 2R$), but the Reynolds number based on the actual steady-state mean speed $\langle \mathrm{v} \rangle$ is about one order of magnitude smaller. The overall porosity in this case is 0.898.

Figure 3.1 compares the simulated mean speed $\langle \mathrm{v} \rangle$ in the y direction, normalized by u_f, as a function of the dimensionless time $\nu t/D^2$, for $s = 9$. The steady-state values of $\langle \mathrm{v} \rangle / u_f$ are 0.08730 and 0.08766, for LBM and Physalis, respectively. In this case, the relative difference between the predicted mean flux is only 0.4%. We then reduce s to 3 and 0, the relative difference between the predicted mean flux becomes 0.37% and 0.35%, respectively. Therefore, regardless whether the glass bead touches the channel wall or not, the predicted mean flow speeds by LBM and Physalis are almost identical.

Since it is assumed that the fluid is at rest at $t = 0$, the body force then accelerates the flow. At the same time, the channel walls and the glass bead create viscous resistance to the flow. The time it takes for the flow to reach to the steady state would be on the order of $\langle \mathrm{v}_\infty \rangle / (F_B/\rho_0) = 0.125(W/D)^2(\langle \mathrm{v}_\infty \rangle / u_f)(D^2/\nu) = 0.02794 D^2/\nu$,

where $\langle v_\infty \rangle$ is the steady-state mean flow speed. The actual e-folding time based on Figure 3.1 is about $1.7 \times 0.02794 D^2/\nu$.

Figure 3.2 shows the y-component velocity profiles at $z = 33.5\delta$ and three y locations. The line in Figure 3.2(b) cuts through the glass bead and the surface locations of the glass bead are marked by the two horizontal lines. Since the z location is very close to the center of the glass bead, the blocking effect of the glass beads is shown at all three y locations. LBM and Physalis yield essentially the same velocity profile at each location.

Next we compare the force and torque acting on the glass bead in Table 3.1 for $s = 3$ and Table 3.2 for $s = 0$. The force on a glass bead is calculated by summing particle momentum changes along all boundary interaction lattice links, while torque is computed by summing the cross products of surface location vector and local momentum change, again along all lattice links. The detail for force and torque calculation can be found, for example, in Yu *et al.* (2003).The force components have been normalized by the net body force $\mathcal{F}_B = [LHW - 4\pi R^3/3]|\mathbf{F}_B|/\rho_0$, and the torque components by $\mathcal{F}_B R$. For $s = 3$, results from the two methods agree very well (to within 1% relative error), except for torque component in the y direction (Table 3.1). The y torque component is two to three orders of magnitude smaller than the other torque components, thus it is not surprising to observe a large relative error. For $s = 0$, again results from the two methods agree very well (Table 3.2), except for the torque component in the y direction (17.6% relative error) and the force component in the z direction (4.2% relative error). This implies that the force in the wall normal direction may not be treated accurately as $s \to 0$, due to a strong pressure gradient in the local region near the contact point between the glass bead and the channel wall, when the glass bead touches the channel wall. Overall, LBM seems to be more accurate when the glass bead touches a channel wall. As another consistency check, we observe the following overall force balance at the steady state

$$\mathcal{F}_{\mathrm{GB}} + \mathcal{F}_{\mathrm{CW}} = \frac{\mathbf{F}_B}{\rho_0}\left[LHW - \frac{4\pi R^3}{3}\right], \tag{3.5}$$

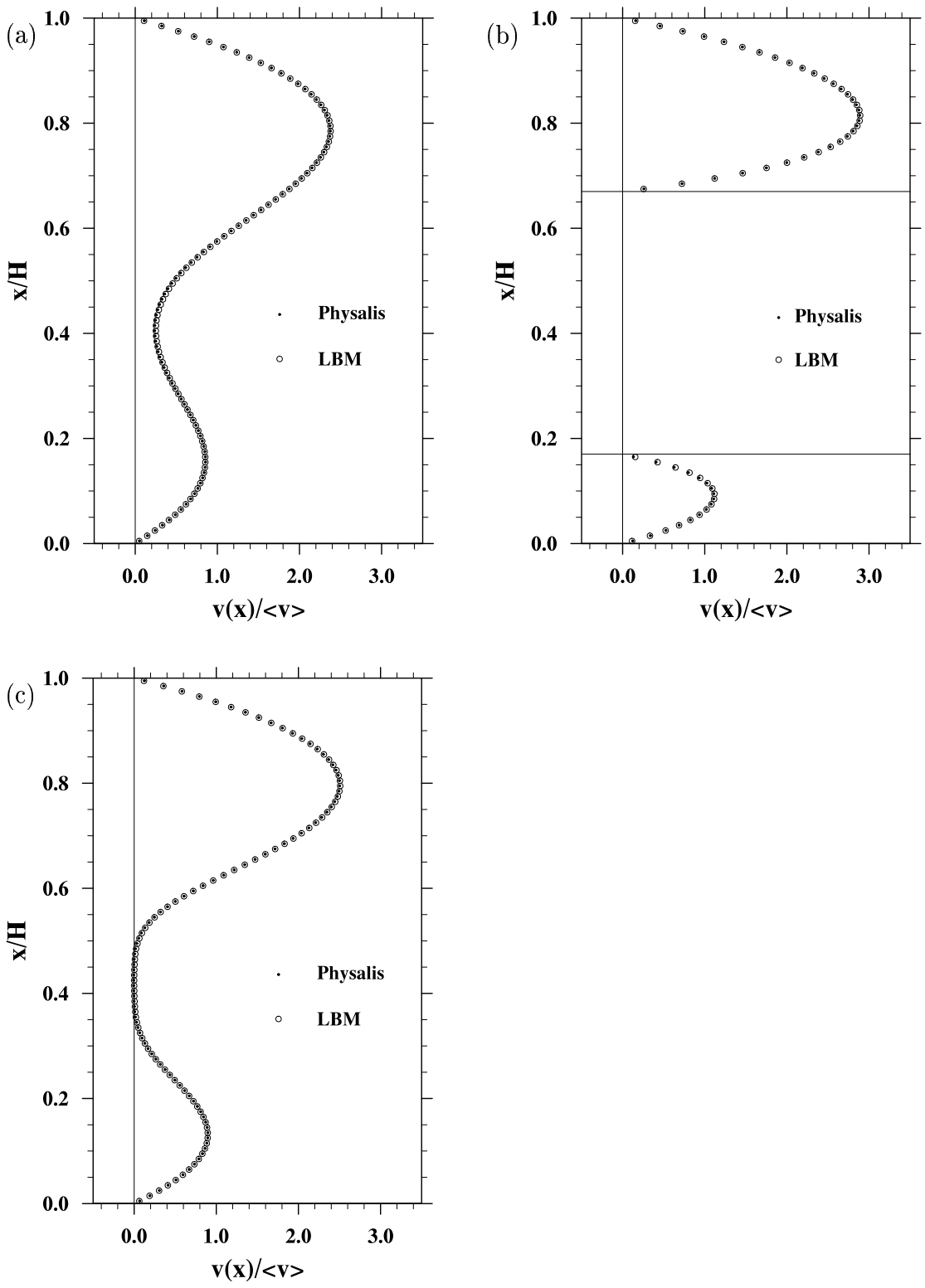

Figure 3.2: Streamwise velocity profiles at $z = 33.5\delta$ and (a) $y = 0.5\delta$, (b) $y = 39.5\delta$, and (c) $y = 65.5\delta$.

Table 3.1: Normalized force and torque acting on the glass bead (Case 1, s=3).

	$\langle v \rangle / u_f$	F_x	F_y	F_z	T_x	T_y	T_z
LBM	9.9308 $\times 10^{-2}$	1.2552 $\times 10^{-3}$	3.6952 $\times 10^{-1}$	1.3902 $\times 10^{-3}$	-6.5705 $\times 10^{-2}$	1.1633 $\times 10^{-4}$	2.5717 $\times 10^{-2}$
Physalis	9.9678 $\times 10^{-2}$	1.2486 $\times 10^{-3}$	3.7104 $\times 10^{-1}$	1.3908 $\times 10^{-3}$	-6.6119 $\times 10^{-2}$	1.3762 $\times 10^{-4}$	2.5892 $\times 10^{-2}$
R.E. (%)	0.37	0.53	0.41	0.05	0.64	18.3	0.68

Table 3.2: Normalized force and torque acting on the glass bead (Case 1, s=0).

	$\langle v \rangle / u_f$	F_x	F_y	F_z	T_x	T_y	T_z
LBM	1.0811 $\times 10^{-1}$	1.2265 $\times 10^{-3}$	3.6510 $\times 10^{-1}$	2.5210 $\times 10^{-3}$	-8.2583 $\times 10^{-2}$	1.4397 $\times 10^{-4}$	2.4909 $\times 10^{-2}$
Physalis	1.0848 $\times 10^{-1}$	1.2190 $\times 10^{-3}$	3.6534 $\times 10^{-1}$	2.6265 $\times 10^{-3}$	-8.4009 $\times 10^{-2}$	1.6940 $\times 10^{-4}$	2.5053 $\times 10^{-2}$
R.E. (%)	0.35	0.61	0.07	4.18	1.73	17.6	0.58

where the two terms on the left hand side are force acting on the glass bead and force acting on the four channel walls, respectively; and the right hand side denotes the net body force, $\mathcal{F}_B$, acting on the fluid. The above balance was indeed observed in each method for each s value.

3.2.3.2 Case 2: Two Beads in a Square Channel

Here we consider a case with two glass beads which both touch the channel walls and also touch each other in the plane $y = 0.5L$. The channel dimensions and glass-bead radius are identical to Case 1, the centers of the two glass beads are $(0.25H, 0.5L, 0.3125W)$ and $(0.65H, 0.5L, 0.6875W)$. The porosity for this case is 0.7955. Figure 3.3 compares the time evolution of the normalized mean flow speed for this case. At the steady state, LBM and Physalis predict the value of $\langle \mathrm{v} \rangle / u_f$ to

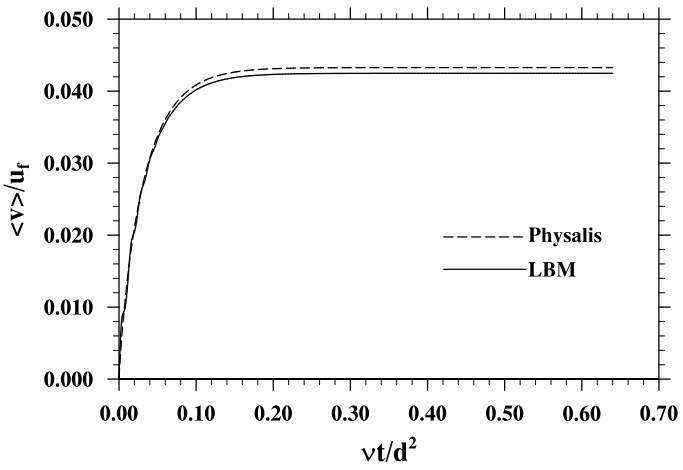

Figure 3.3: The time evolution of the mean velocity in the y direction for the case with two glass beads. The results from LBM and Physalis have a relative error of 1.87%.

be 0.04248 and 0.04328, respectively, with Physalis giving a mean speed 1.87% larger than that of LBM. Again, the transition time to the steady state is on the order of $\langle \mathrm{v}_\infty \rangle / (F_B/\rho_0) = 0.125(W/D)^2(\langle \mathrm{v}_\infty \rangle / u_f)(D^2/\nu) = 0.01359 D^2/\nu$. The actual e-fold time based on Figure 3.3 is about $2.4 \times 0.01359 D^2/\nu$. Note that the factor 2.4 here is larger than the corresponding factor 1.7 in Case 1, due to a more complex porous geometry in the channel.

In Figure 3.4 we compare the y component velocity profiles on three lines along the x direction. The glass-bead surfaces are marked with horizontal lines and only the velocity profiles in the fluid region is plotted. Overall, the velocity profiles agree well quantitatively, although some minor differences are visible in Figure 3.4.

The total forces acting on glass beads and on channel walls are compiled in Table 3.3, and the sum is compared with the net body force. The last two columns of Table 3.3 are the relative error (defined as the difference between Physalis and LBM results, normalized by the LBM result) and the normalized error (defined as the force difference between Physalis and LBM, normalized by the net body force). The normalized error is less than 2%, indicating a reasonable comparison between the two methods. In LBM, overall balance as shown in Eq. (3.5) is observed precisely

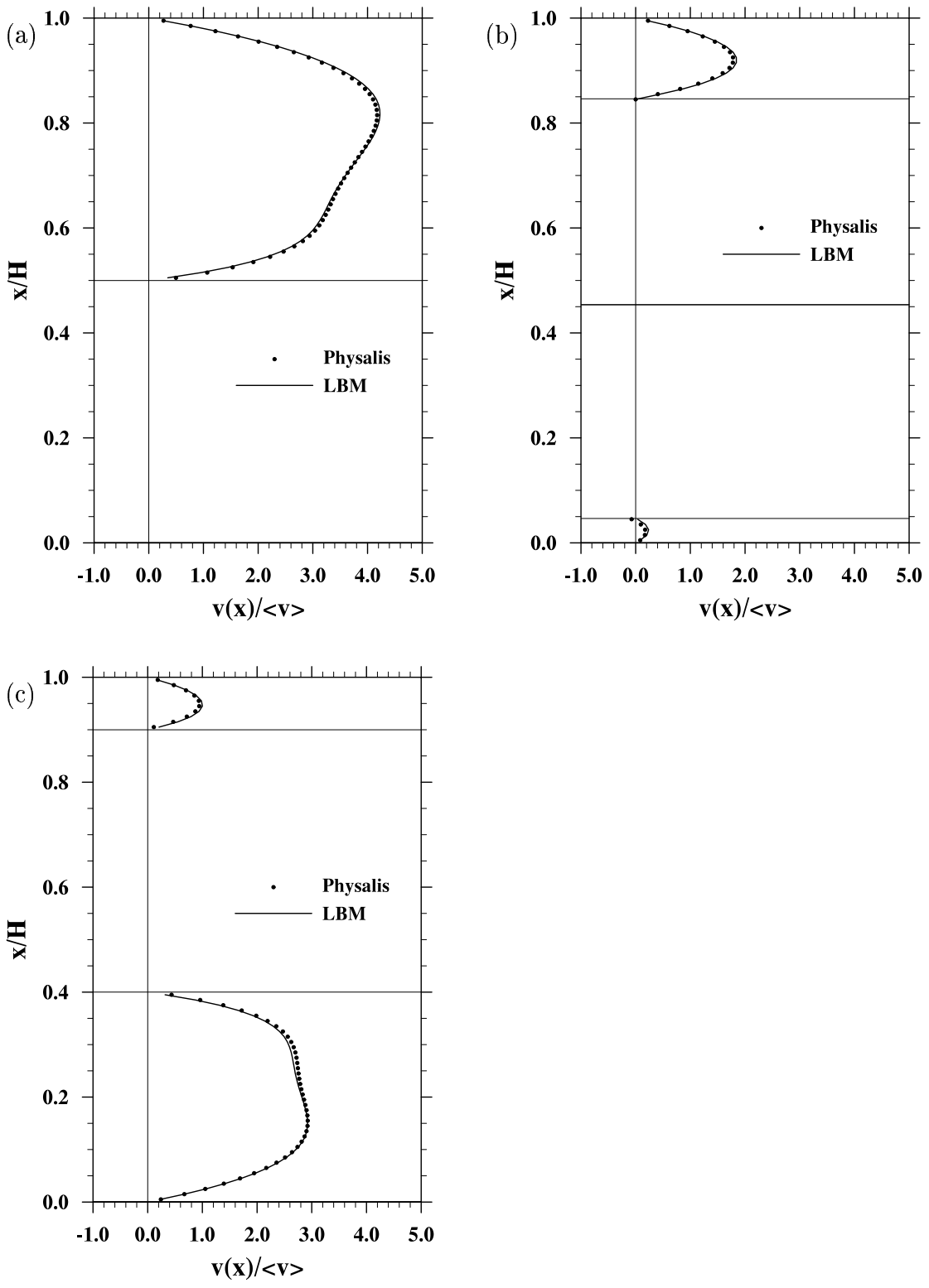

Figure 3.4: Streamwise velocity profiles for Case 2 at $y = 39.5\delta$ and (a) $z = 24.5\delta$, (b) $z = 39.5\delta$, and (c) $z = 54.5\delta$. The lines show the results from LBM and symbols are the results from Physalis.

Table 3.3: Normalized forces and balance for Case 2. All forces are normalized by the net body force.

	LBM	Physalis	R.E. (%)	N.E. (%)
$\mathcal{F}_{GB}$:				
x	4.5587×10^{-4}	4.2787×10^{-4}	6.2	2.8×10^{-3}
y	5.6642×10^{-1}	5.8297×10^{-1}	2.9	1.7
z	-3.7450×10^{-4}	-3.7915×10^{-4}	1.3	4.7×10^{-4}
$\mathcal{F}_{CW}$:				
x	-4.5587×10^{-4}	-4.0881×10^{-4}	10.3	4.7×10^{-3}
y	4.3239×10^{-1}	4.3184×10^{-1}	0.13	5.5×10^{-2}
z	3.7451×10^{-4}	3.8574×10^{-4}	3.0	1.1×10^{-3}
$\mathcal{F}_{GB}+\mathcal{F}_{CW}$:				
x	0.000	1.91×10^{-5}	–	1.91×10^{-3}
y	0.9988	1.0148	1.6	1.6
z	0.00	6.59×10^{-6}	–	6.59×10^{-4}
$\mathcal{F}_{B}$:				
x	0.0	0.0	–	–
y	1.0	1.0	–	–
z	0.0	0.0	–	–

(Table 3.3). In Physalis, the sum of forces acting on the beads and walls is found to be 1.015 times the net body force, namely, there is a 1.5% relative error in Physalis on force balance. This suggests that LBM code is superior to the current version of Physalis code. This is likely due to the following reasons: (1) the coupling of Stokes flows and the numerical flow in Physalis becomes less accurate when there are particle-particle and particle-wall contacts; (2) since the force calculation in LBM is based on precise local momentum exchanges between the mesoscopic particles and a solid surface, the integral force balance follows more naturally in LBM.

3.2.3.3 Case 3: 25 Beads in a Square Channel

In the last inter-comparison case, 25 glass beads are placed in the channel. The front and side views of the 25 glass beads relative to the channel are shown in Figure 3.5. In this case, $L = 70\delta$, $H = W = 160\delta$, and $R = 20\delta$. Sixteen glass beads

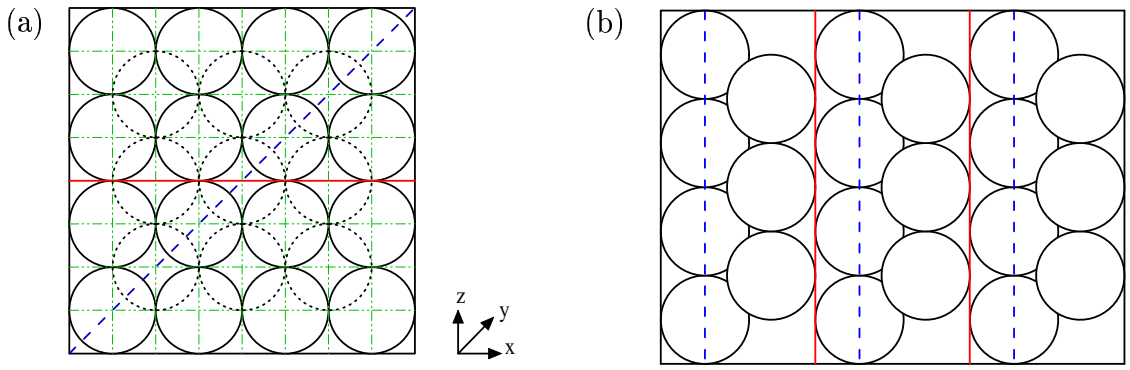

Figure 3.5: Geometric configuration of 25 glass beads in 3D channel: (a) front $(x-z)$ view; (b) side $(y-z)$ view. This configuration is densely packed in the center of the cell, but not closely packed at the inlet and outlet.

are located at $y = 20\delta$ and nine are at $y = 50\delta$. The porosity for this case is 0.5325. Again the flow is forced by a body force in the y direction with $F_B = 8\mu u_f/W^2$.

In both LBM and Physalis, $\nu = 1/9$ and $u_f = 0.2$. The simulated steady-state mean speed is $0.000521u_f$ in LBM, so the Reynolds number based on the mean speed and the diameter of the glass bead is $D\langle \mathrm{v} \rangle/\nu = 0.03733$. In the Physalis simulation, the simulated steady-state mean speed is $0.000589u_f$. Therefore, the mean flux in Physalis is 13.1% larger than the value in LBM. The reason for the larger flux in Physalis is partly due to the poor representation of no-slip boundary condition, as shown below.

Figure 3.6 shows the velocity profiles for x and y components at $y = 0$ and $z = 0.5W$. Since this is a center cut at the inlet plane, by symmetry the z-component velocity is zero. On this particular line, there are three contact points ($x/W = 0.25, 0.50,$ and 0.75) which are marked by the three horizontal lines. Both $x-$ and $y-$ velocity components are zero at these contact points. Figure 3.6(b) shows clearly that LBM does better than Physalis in satisfying the no-slip boundary condition at the contact points. The y component velocity is larger than zero everywhere on the selected line, but the x component velocity takes both positive and negative value as the fluid finds its path through the gap regions in between the glass beads. LBM and Physalis give qualitatively similar profiles, both showing very complex velocity distributions. There

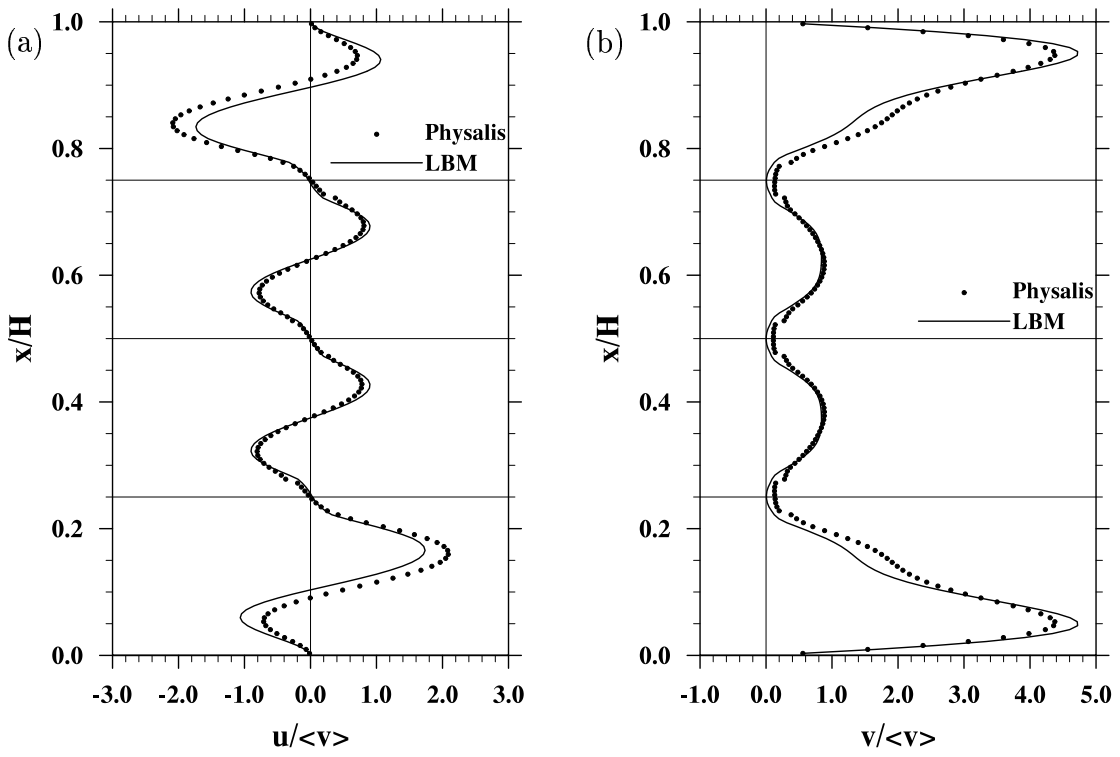

Figure 3.6: Velocity profiles at $y = 0$ and $z = 0.5W$: (a) u profile, (b) v profile. LBM simulation gives exact zero w velocity on the same line (not shown here), while Physalis yields a slightly non-zero value with magnitude below $0.6u_f \times 10^{-6}$.

are some quantitative differences between the LBM and Physalis results. The maximum $y-$ component velocity is found near the channel wall as the local porosity is larger due to the unfilled space in the 9-bead layer.

The velocity distributions along a diagonal line ($x = z$) at the inlet plane are shown in Figure 3.7. This time there are 7 glass-bead contact points as marked by the 7 horizontal lines. The LBM simulation gives zero value for all the three velocity components at the 7 contact points, but the y-component velocity in Physalis at the contact points (computed by interpolating from the numerical grid, not from the analytical Stokes flow) are not exactly zero. Due to the symmetry, the x-component and z-component velocity should have an identical profile. The LBM results meet this symmetry requirement, but the Physalis results do not meet this condition (not shown

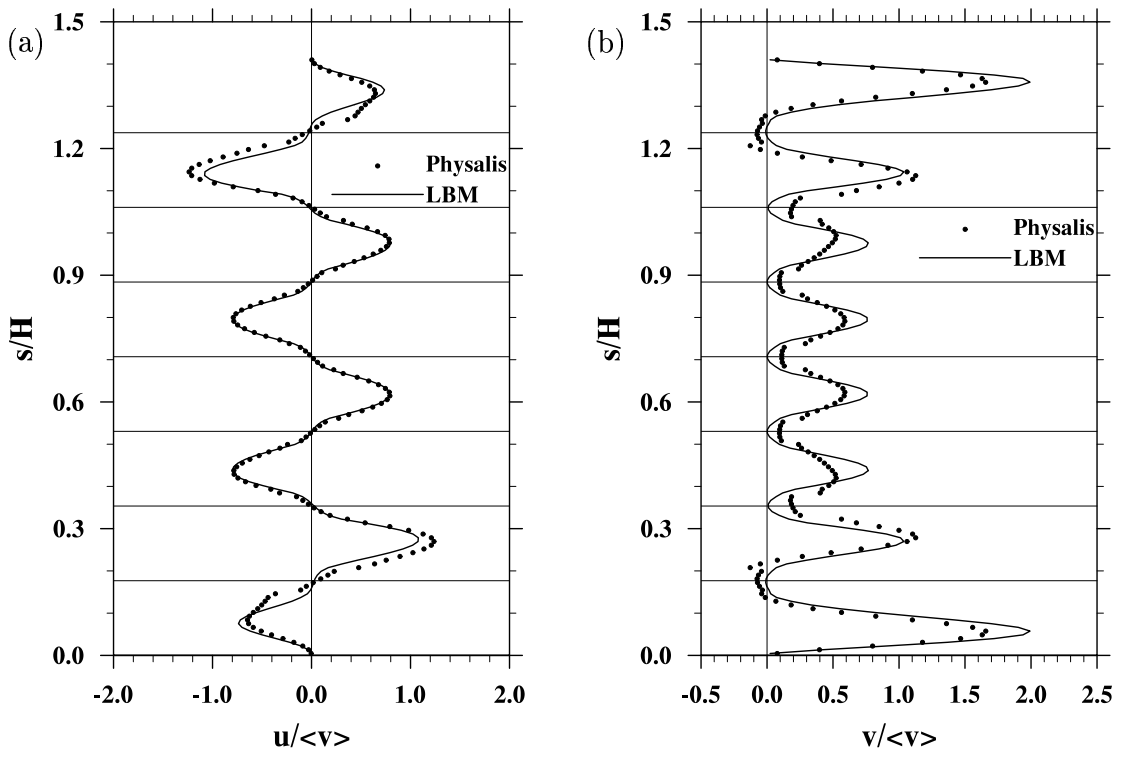

Figure 3.7: Velocity profiles at $y = 0$ and along the diagonal line $z = x$: (a) u profile, (b) v profile.

here). These observations plus a convergence test with varying mesh resolutions indicate that again LBM is better in handling viscous flow through a porous passage with many solid-solid contact points.

In summary, while LBM and Physalis yield almost identical results for a porous channel with one glass bead, the accuracy of Physalis appears to deteriorate as the number of glass beads (and contact points) is increased. In general, the local treatment of the no-slip boundary condition in LBM (interpolated bounce back) is not only simpler but also more accurate than the whole-particle treatment in Physalis (via analytical Stokes flow solution on each glass bead). It may be possible that a higher mesh resolution is required for Physalis to accurately capture the very nonuniform flows in between the glass beads. In the following, the LBM flow is used when the transport of colloids is studied.

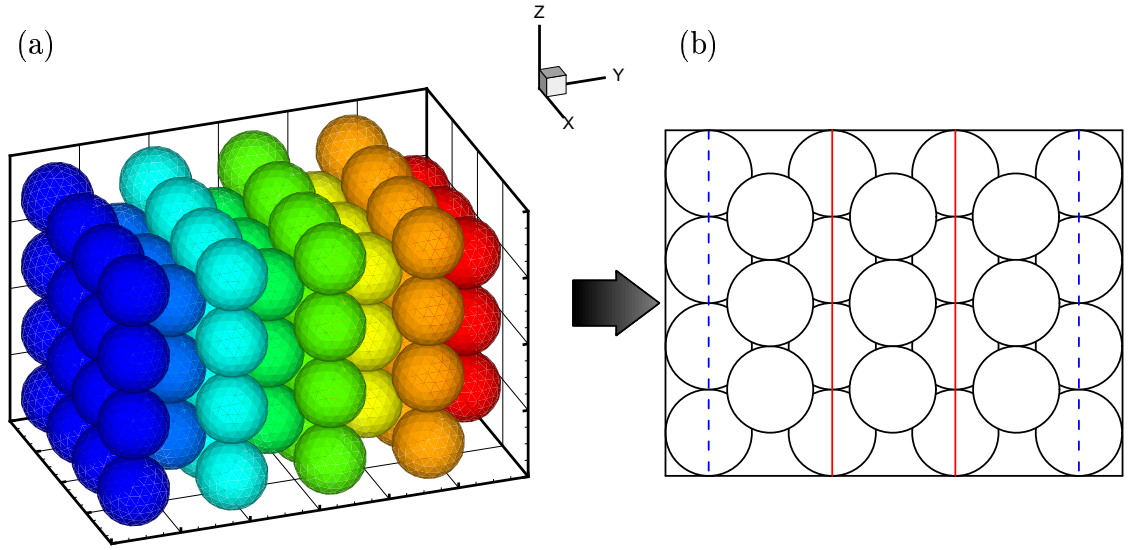

Figure 3.8: A dense cubic packing of glass beads in a square channel used for preliminary colloidal transport study: (a) 3D view; (b) side view.

3.3 Transport of Colloids

Now we consider a 3D porous medium flow through a square channel densely packed with spherical glass beads, as shown in Figure 3.8. The glass beads were used in our parallel microscopic visualization (Qiu *et al.*, 2012).

The geometry is similar to Case 3 discussed in the last section, except that now even at the inlet and outlet the glass beads are packed. The flow simulation covers a region from the center of 25-bead layer to the center of the next 25 beads layer, as shown by the two red solid lines in Figure 3.8(b). The mesh resolution are set as: $H = W = 160\delta = 800\ \mu m$, $L = 57\delta = 285\ \mu m$, and $R = 20\delta = 100\ \mu m$, where the mesh spacing is 5 μm (Table 3.4). The 16-bead layer is centered at $y = 0$ and the 9-bead layer at $y = 142.5\ \mu m$. The nearest center-to-center distance between a bead in the 9-bead layer and a bead in the 16-bead layer is $\sqrt{142.5^2 + (100\sqrt{2})^2} = 200.764\ \mu m$, so there is a tiny gap of 0.764 μm. Since this gap is much smaller than the grid spacing (5 μm) and is not resolved numerically, we may view that all beads are in contact with the nearby beads. The colloid diameter is 1 μm.

The mean flow speed $\langle \mathrm{v} \rangle \equiv U_s$, defined as the flux over the channel cross

Table 3.4: Physical parameters and their values in the 3D numerical simulation.

	Symbol	Physical value	Numerical value
water density	ρ	1000 kg/m^3	1
water viscosity	μ	0.001 $kg/(m \cdot s)$	0.128
grid spacing	dx, dy	5 μm	1
channel width (/height)	H	800 μm	160
periodicity length	L	285 μm	57
glass bead radius	R	100 μm	20
colloid radius	a_c	0.5 μm	0.1
velocity used in setting F_{B}	U_c	10800 m/day	0.08
mean speed realized	U_s	3.52 m/day	2.608×10^{-5}
porosity	ϵ	0.426	0.426
nominal flow speed	U_s/ϵ	8.263 m/day	6.122×10^{-5}
colloid density	ρ_c	1055 kg/m^3	1.055
time step	dt	3.2×10^{-7} s	0.1
mass of colloid (actual)	m_c	5.524×10^{-16} kg	4.42×10^{-3}
mass of colloid (assumed)	m_c^*	6.033×10^{-12} kg	48.264
response time (actual)	τ_c	5.86×10^{-8} s	1.831×10^{-2}
response time (assumed)	τ_c^*	6.4×10^{-4} s	200
unit length		1.0 m	2.0×10^5
unit mass		1.0 kg	8.0×10^{12}
unit time		1.0 s	3.125×10^5
unit velocity		1.0 m/s	0.64
unit force		1.0 N	1.6384×10^7

sectional area is 40.75 $\mu m/s$, which is designed to match a value of about 40 $\mu m/s$ in our parallel experimental microscope visualization (Qiu *et al.*, 2012). The ratio of $\langle \mathrm{v} \rangle / u_f$ was found to be 3.26×10^{-4}. The flow Reynolds number based on this mean speed and glass-bead diameter is 0.00815. The porosity ϵ of the channel is 0.4259. The nominal flow speed, U_s/ϵ is about 8.26 m/day. Other parameters of the flow simulations are shown in Table 3.4.

3.3.1 Equation of Motion for Colloids

Colloids are randomly injected into the flow at the inlet plane (y=0 plane) with initial velocity equal to the local flow velocity, and at a rate of about 260 colloids per second to simulate a number concentration of about 10^4 colloids per mm^3 water solution. The velocity and location of each colloid are obtained by numerically integrating the equation of motion of the form

$$m_c \frac{d\mathbf{V}(t)}{dt} = \mathbf{F}^{\mathrm{drag}} + \mathbf{F}^{\mathrm{fa}} + \mathbf{F}^{\mathrm{am}} + \mathbf{F}^{\mathrm{b}} + \mathbf{F}^{\mathrm{g}} + \mathbf{F}^{\mathrm{B}} + \mathbf{F}^{\mathrm{c}}, \tag{3.6}$$

$$\frac{d\mathbf{Y}(t)}{dt} = \mathbf{V}(t) \tag{3.7}$$

where $\mathbf{V}(t)$ is the instantaneous (Lagrangian) velocity of the colloid, $m_c \equiv 4\pi\rho_c a_c^3/3$ is the mass of the colloid, ρ_c is the material density of the colloid, and a_c is the radius of the colloid. The hydrodynamic forces include the quasi-steady drag force $\mathbf{F}^{\mathrm{drag}}$, the fluid acceleration force $\mathbf{F}^{\mathrm{fa}}$, the added mass $\mathbf{F}^{\mathrm{am}}$, and the buoyancy force $\mathbf{F}^{\mathrm{b}}$. $\mathbf{F}^{\mathrm{g}}$ is the gravitational body force. $\mathbf{F}^{\mathrm{B}}$ is a random force designed to simulate Brownian motion of the colloid due to local thermal fluctuations of solvent molecules. Finally, $\mathbf{F}^{\mathrm{c}}$ represents interaction forces of the colloid with the glass (grain and wall) surface or other deposited colloids. An original derivation of the equation of motion can be found in Maxey and Riley (1983). The deviations relevant to the present application are explained below.

When a colloid is not close to a surface, the drag is the quasi-steady Stokes drag. However, when the distance between a colloid and a glass surface is on the order of colloid diameter, the drag force will be modified as a result of colloid-surface local hydrodynamic interaction (Spielman 1977; Johnson *et al.*, 2007). Under the Stokes flow assumption, the flow field around a colloid near a surface can be solved. The net result of the colloid-surface hydrodynamic interaction is usually represented by a correction factor to the Stokes drag. It is convenient to consider these corrections in the directions normal and tangential to the surface separately. In the normal direction,

the drag force may be written as

$$\mathbf{F}_n^{\text{drag}} = \zeta \left(f_2 \mathbf{u}_n - \frac{\mathbf{V}_n}{f_1} \right) \tag{3.8}$$

where $\zeta \equiv 6\pi\mu a_c$, μ is the solvent viscosity, $\mathbf{u}_n = (\mathbf{u} \cdot \hat{\mathbf{n}})\,\hat{\mathbf{n}}$, $\mathbf{V}_n = (\mathbf{V} \cdot \hat{\mathbf{n}})\,\hat{\mathbf{n}}$, $\mathbf{u}(\mathbf{x}, t)$ is the Eulerian solvent velocity at the instantaneous location of the colloid, $\hat{\mathbf{n}}$ is the unit normal vector pointing from the center of the nearest glass bead to the center of the colloid.

In the tangential direction, the drag force is

$$\mathbf{F}_t^{\text{drag}} = \frac{\zeta}{f_4} \left(f_3 \mathbf{u}_t - \mathbf{V}_t \right) \tag{3.9}$$

where $\mathbf{u}_t = \mathbf{u} - \mathbf{u}_n$, $\mathbf{V}_t = \mathbf{V} - \mathbf{V}_n$.

The correction factors f_i are functions of $\bar{h}$, the gap distance, normalized by colloid radius, between the colloid surface and its nearest solid surface (Spielman 1977; Johnson *et al.*, 2007):

$$f_1\left(\bar{h}\right) = 1.0 - 0.443\exp\left(-1.299\bar{h}\right) - 0.5568\exp\left(-0.32\bar{h}^{0.75}\right) \tag{3.10}$$

$$f_2\left(\bar{h}\right) = 1.0 + 1.455\exp\left(-1.2596\bar{h}\right) + 0.7951\exp\left(-0.56\bar{h}^{0.50}\right) \tag{3.11}$$

$$f_3\left(\bar{h}\right) = 1.0 - 0.487\exp\left(-5.423\bar{h}\right) - 0.5905\exp\left(-37.83\bar{h}^{0.50}\right) \tag{3.12}$$

$$f_4\left(\bar{h}\right) = 1.0 - 0.35\exp\left(-0.25\bar{h}\right) - 0.40\exp\left(-10.0\bar{h}\right) \tag{3.13}$$

These factors all reduce to 1 when $\bar{h}$ is larger than 3, and the Stokes drag is recovered.

The tangential direction is determined according to the sum of all tangential forces acting on the colloid, namely,

$$\hat{\mathbf{t}} = \frac{\sum \mathbf{F} - \sum \mathbf{F}_n}{\left|\sum \mathbf{F} - \sum \mathbf{F}_n\right|} \tag{3.14}$$

The fluid acceleration force is the force due to the background moving fluid and is given as

$$\mathbf{F}^{\mathrm{fa}} = m_f \frac{d\mathbf{u}}{dt} \tag{3.15}$$

where $m_f \equiv 4\pi\rho_f a_c^3/3$, ρ_f is the density of the fluid, and $d\mathbf{u}/dt$ is the fluid Lagrangian acceleration.

The added mass is a force due to the relative acceleration and is expressed as

$$\mathbf{F}^{\mathrm{am}} = -\frac{1}{2} m_f \left(\frac{d\mathbf{V}}{dt} - \frac{d\mathbf{u}}{dt} \right) \tag{3.16}$$

The buoyancy force and body force together is given as

$$\mathbf{F}^{\mathrm{bg}} = \mathbf{F}^{\mathrm{b}} + \mathbf{F}^{\mathrm{g}} = m_c (1 - \frac{\rho_w}{\rho_c}) \mathbf{g} \tag{3.17}$$

where ρ_w is the solvent density and $\mathbf{g}$ is the gravitational acceleration.

The Brownian force is specified as $\mathbf{F}^{\mathrm{B}} = (F_1^{\mathrm{B}}, F_2^{\mathrm{B}}, F_3^{\mathrm{B}})$, where each component F_i^{B} is an independent Gaussian random variable of zero mean and the following standard deviation

$$\sigma_{F_i^{\mathrm{B}}} = \sqrt{\frac{2\zeta kT}{dt}}, \tag{3.18}$$

where dt is the time step size, T is the temperature (assumed to be 293 K), $k = 1.38 \times 10^{-23}\ J/K$ is the Boltzmann constant. When a simple explicit Euler scheme is applied, the Brownian force would generate the desired mean square value (kT/m_c) of velocity fluctuation in each direction (Elimelech *et al.*, 1995). The ratio of the Brownian force to the drag force is estimated to be $\sqrt{2\tau_c kT/(m_c U_s^2 dt)} \approx 2.84$, implying that the Brownian effect is as important as the drag force in transporting the colloidal particles. The above treatment for the Brownian motion is based on a stochastic (Langevin equation) model. It should be noted that an alternative method would be to directly introduce fluctuating hydrodynamics (Landau and Lifshitz, 1959) within the lattice Boltzmann equation, known as the fluctuating lattice Boltzmann equation. This has been formulated in Ladd (1993, 1994a, 1994b) and Dünweg *et al.* (2007) and shown to yield correct thermal fluctuations. We adopted the particle-based Langevin

equation approach since the pore-scale flow in the absence of thermal fluctuations was assumed to be steady and was solved first by MRT-LBM. It is important to note that in this work the disturbance flows near colloids are not directly resolved. The motion of colloids was then integrated via a modeled equation of motion, using a large number of time steps with a small time step size. A small time step size is necessary in view of a small inertial response time of colloid and rapid changes of hydrodynamic drag and electrostatic interaction force when a colloid is approaching a grain surface. On the other hand, the fluctuating lattice Boltzmann equation would require a simultaneous evolution of the pore-scale flow with thermal fluctuations and the motion of colloids without Brownian force. This could be computationally more expensive if a small time step size has to be used.

While the drag force and the Brownian force are active in all regions of the flow domain, the colloidal interaction force is only relevant when a colloid is very close to a solid surface or another deposited colloid. It consists of the electrostatic, Lifshitz-van der Waals, and Lewis acid/base interaction forces (van Oss 1994),

$$F^{\mathrm{c}} = F^{\mathrm{EDL}} + F^{\mathrm{LW}} + F^{\mathrm{AB}}, \tag{3.19}$$

where all interaction forces are assumed to act in the direction normal to a surface, with a positive value indicating a repulsive force and negative an attractive force. The formulation of these forces is primarily based on the Derjaguin-Landau-Verwey-Overbeek (DLVO) interaction potential (Derjaguin and Landau, 1941; Verwey and Overbeek, 1948). The electrostatic double layer (EDL) force results from the interaction of a charged particle with the ions in the liquid medium. For colloid-glass surface interaction, the EDL force may be written as (Hogg *et al.*, 1966; Qiu *et al.*, 2012)

$$F^{\mathrm{EDL,cg}} = \frac{a_c \kappa}{1 - \exp(-2\kappa h)} \times \left[\alpha_1 \exp(-\kappa h) - \alpha_2 \exp(-2\kappa h)\right], \tag{3.20}$$

where h is the minimum gap between the colloid and a glass surface (the distance from the center of the colloid to the surface minus a_c), κ is the inverse Debye-Huckel screening length which depends on the solution ionic strength. Here we shall only

consider an ionic strength at 100 mM in NaCl electrolyte solution, and in this case $1/\kappa = 0.963\ nm$. The coefficients α_1 and α_2 are related to the surface potentials of the glass surface (-69.74 mV) and colloid (-76.99 mV) as well as the dielectric constant of the medium (Qiu *et al.*, 2012). The surface potentials are computed based on the measured ζ-potentials (-41.31 mV and -45.56 mV, respectively (Qiu *et al.*, 2012). For the electrolyte solution used in this study (Qiu *et al.*, 2012), $\alpha_1 = 4.648 \times 10^{-11}\ N$ and $\alpha_2 = 4.671 \times 10^{-11}\ N$. With the above parameters, the EDL force is repulsive and $F^{\mathrm{EDL}}/(\zeta U_s) > 1$ when $h/a_c < 0.02$ (Figure 3.9). For the case of colloid-colloid interaction at 100 mM ionic strength, the EDL force is computed by (Elimelech *et al.*, 1995)

$$F^{\mathrm{EDL,cc}} = (1.847 \times 10^{-11}\ N) a_c \kappa \exp(-\kappa h), \tag{3.21}$$

where h is the minimum gap between the two approaching colloids.

The attractive Lifshitz-van der Waals (LW) interaction accounts for intermolecular interaction including London dispersion, Keesom dipole-dipole, and Debye induction. For the purpose of this paper, the LW force can be written as (van Oss, 1994; Qiu *et al.*, 2012)

$$F^{\mathrm{LW}} = -\beta a_c \left(\frac{h_0}{h}\right)^2, \tag{3.22}$$

where h_0 is an equilibrium distance used to model the occurrence of physical contact and is set to 0.157 nm (Elimelech *et al.*, 1995). The constant β has been determined to be 0.0434 J/m^2 for colloid-surface interaction and 0.0469 J/m^2 for colloid-colloid interaction, based on the thermodynamic parameters of colloids, glass, and the liquid solution.

The Lewis acid/base (AB) force originates from the bonding reaction of a Lewis acid and a Lewis base. It can be expressed as (van Oss, 1994; Qiu *et al.*, 2012)

$$F^{\mathrm{AB}} = -\gamma \frac{h_0 a_c}{\chi} \exp\left(\frac{h_0 - h}{\chi}\right), \tag{3.23}$$

where $\chi = 0.6\ nm$ is the water decay length (van Oss 1994), the constant γ is determined, using the relevant electron-accepter and electron-donor parameters, to be

$-0.0322\ J/m^2$ and $-0.170\ J/m^2$ for colloid-surface and colloid-colloid interactions, respectively.

The numerical method for integrating the equation of motion follows our 2D simulations (Gao *et al.*, 2008; Qiu *et al.*, 2012), namely, a fourth-order Adams-Bashforth scheme for colloid equation of motion excluding the Brownian force term, and Euler scheme for the Brownian force. Then the colloid location is updated by a fourth-order Adams-Moulton scheme. The time step size used to integrate the colloid equation of motion is $dt = 3.2 \times 10^{-7}\ s$, thus one colloid is injected at the inlet every $12,000$ time steps. A total of 12 million time steps were calculated by the code, during this period $1,000$ colloids were injected and the injected fluid volume covers roughly 1.29 periodic lengths.

From Table 3.4, it is also noted that the flow time scale is on the order of $\tau_f = a_c/U_s = 0.0123$ s, therefore the Stokes number is $St = \tau_c/\tau_f = 4.764 \times 10^{-6}$, where $\tau_c = 2\rho_c a_c^2/(9\mu)$ is the inertial response time of a colloid. To reduce the stiffness of the colloid equation of motion, an adjusted colloid inertial response time τ_c^* was used (Table 3.4), leading to $St^* = \tau_c^*/\tau_f = 0.05203$ but still maintaining $St << 1$. A colloid is assumed to have deposited if the gap distance between the colloid surface and grain surface is less than $0.157nm$ (Qiu *et al.*, 2012).

3.3.2 Results on Colloid Trajectories and Retention

Here some preliminary results on transport and retention of colloids in 3D porous channel are discussed. Our main interest is to understand if and how a colloid will deposit on a solid surface (glass-bead surface and channel wall) when it is being transported through the porous flow passage.

Two runs (Table 3.5) were performed to isolate the effect of local hydrodynamic interactions. In Run 1 the hydrodynamic interactions were turned off by setting all the correction factors (f_1 to f_4) to one. In Run 2, Eq.'s (3.10) to (3.13) were used. The comparison of the two runs allows us to understand the role of local hydrodynamic interactions on colloid retention.

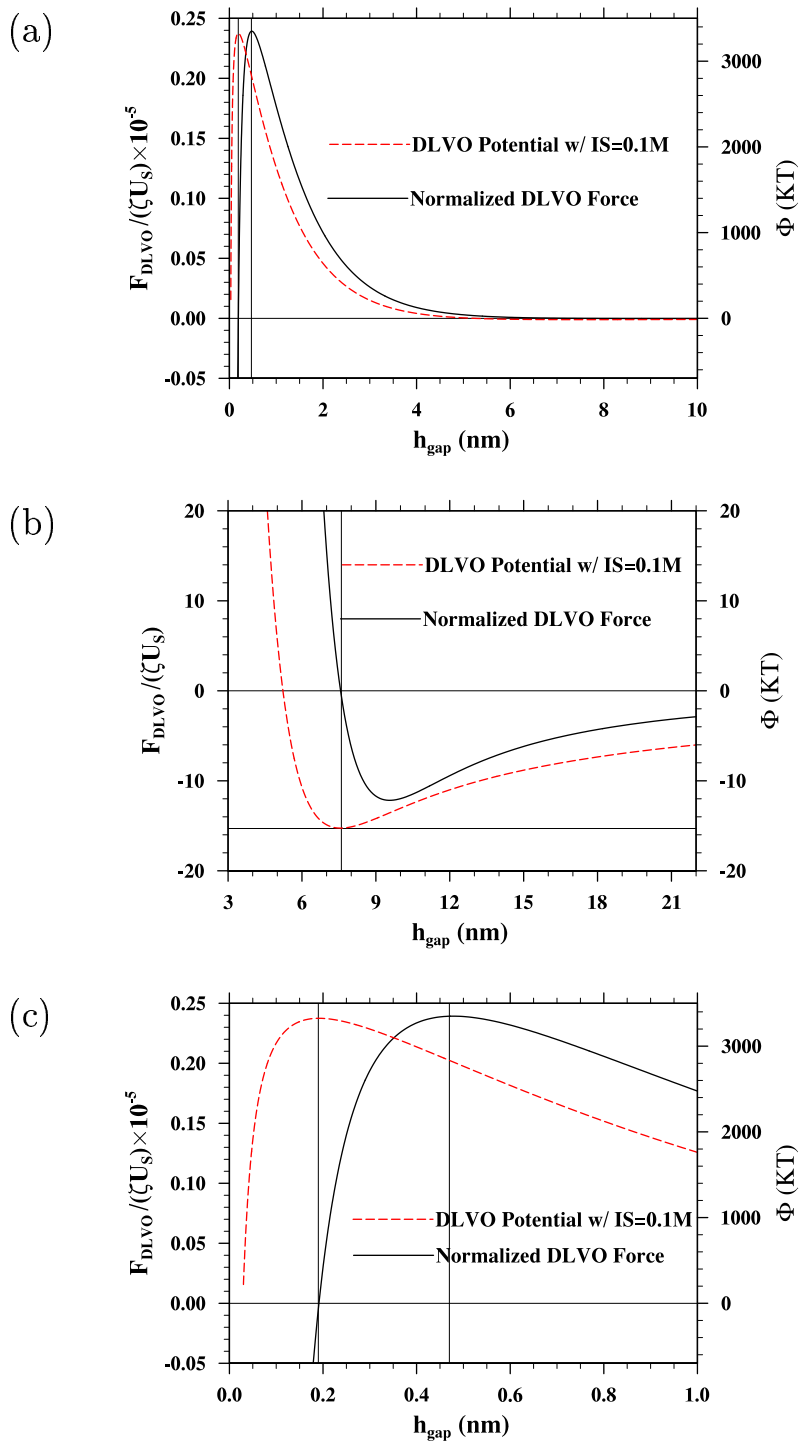

Figure 3.9: DLVO potential energy and force as a function of the gap distance: (a) full view; (b) zoom-in view near SEM; (c) zoom-in view near peak energy barrier.

Table 3.5: Force combinations tested in simulations of colloid transport and deposition.

	Brownian force	Local hydrodynamic interaction	Colloidal interaction force	Added mass	Fluid acceleration force	Gravity & buoyancy force
Run 1	ON	OFF	ON	ON	ON	OFF
Run 2	ON	ON	ON	ON	ON	OFF

Table 3.6: Number of deposited colloids and residence for different runs.

	PEM deposition (counts) ($h_{eq} = 0.157nm$)	SEM deposition (counts) ($h_{gap} \leq 13.3nm$)	near surface residence (occurrence) ($h_{gap} < 13.3nm$)	($13.3 < h_{gap} < 100nm$)
Run 1:	0 / 1,000	93 / 1,000	4.37×10^8	3.10×10^6
Run 2:	0 / 1,000	43 / 1,000	1.85×10^8	5.28×10^6

For each run, the simulation was repeated twice. First, only retention at the primary energy minimum (PEM) was counted by using a gap distance of $0.157nm$ as the criterion for deposition. The gap distance $0.157nm$ corresponds to the left of peak energy barrier ($3,324kT$ located at $0.191nm$). The DLVO energy and force are shown in Figure 3.9. For the specific conditions considered here, the peak energy barrier is extremely high, but the secondary energy minimum (SEM) is also significant, and the SEM well covers a larger region. The repeated run, while keeping all other conditions, used a gap distance of $13.3nm$ as the retention criterion, namely, a colloid located below $13.3nm$ at the end of simulation is viewed as a deposited colloid. $13.3nm$ corresponds to a location with a negative energy potential of $-10kT$, slightly to the right of secondary energy minimum (SEM), with DLVO energy of $-15.25kT$ at a gap

distance of $7.58nm$. The idea here is that the first run captured retention at PEM only, while the second run capture both retention at both PEM and SEM. The differences between the numbers of retention from the two sub-runs may be loosely interpreted as the number of retention at SEM, as a retention at $-10kT$ location is likely to move further down to the SEM well and thus is unlikely to escape the SEM well — some evidence of this will be shown in Figure 3.13(b) below. For the discussions below, the first sub-runs will be called Run 1a and Run 2a, and the repeated runs will be denoted as Run 1b and Run 2b.

Table 3.6 shows that the total number of deposited colloids at a time when a total of $1,000$ colloids have been injected at the inlet. No deposition was observed in both Run 1a and Run 2a, this is consistent with the very high $(3,324kT)$ value of peak energy barrier[1]. Out of the $1,000$ colloids injected, 93 were found to be deposited at SEM when local hydrodynamic interactions were not considered. This number reduced to 43 when the hydrodynamic interactions (or hydrodynamic retardation effect) were included. This implies a factor of 2.2 reduction in deposition at SEM.

Also listed in Table 3.6 are the numbers of near-surface residence occurrence — an occurrence is counted if a colloid was found to be located within a selected gap distance range at any time step. Two gap distance ranges were considered: $h_{gap} < 13.3\,nm$ and $13.3\ nm < h_{gap} < 100\ nm$. Interestingly, while the near-surface residence for

[1] Before we arrived at this result, we tested convergence of the results with changing time step size. In the process, we found that too large of a time step could lead to deposition simply due to a numerical artifact: an overprediction of colloid velocity near a grain surface can lead to unstable oscillations of colloid position, first outside the peak energy barrier; then the oscillations amplified and led to a jump across the peak energy barrier which became counted as a deposition at PEM. Such numerical artifact is more severe when the local hydrodynamic interactions are considered — this is expected as the correction factors are very sensitive function of gap distance when the gas distance is small. The results presented here used a very small time step size of $dt = \tau_c^*/2,000$. Physically, such small time step size is needed only when a colloid is very close to the grain surface (say below $100nm$) where the correction factors and the DLVO energy profile changes very rapidly. Outside this region, a larger time step size can be used. We are currently investigating the use of variable time step size for Lagrangian tracking of colloids.

$h_{gap} < 13.3\ nm$ was reduced to $1.85/4.37 = 42.3\%$ when the hydrodynamic retardation was introduced, the residence time for the gap range $13.3\ nm < h_{gap} < 100\ nm$ was 70% higher with the hydrodynamic retardation. This in part is due to slower velocity of a colloid in this region. Also a trapped colloid will also take longer time to escape this region. Taken together, the total residence times for $h_{gap} < 100\ nm$ were 7.47×10^8 and 7.13×10^8 for Run 1 and Run 2, respectively. In other words, the hydrodynamic retardation shifted colloids from the secondary energy well region to a region slightly outside (but still close to the grain surface). Note that the DLVO energy is $-1.31kT$ at 100 nm. Therefore, a portion of the colloids located in the range $13.3\ nm < h_{gap} < 100\ nm$ could still be viewed as temporarily deposited. We are working to generate local number concentration profile as a function of the gap distance, similar to what has been presented in Yang *et al.* (1998) for an impinging jet system. This will require more samples (longer-time run) and more in-depth post-processing. Nevertheless, the above data implies that the concentration profile near the SEM is less peaked when the hydrodynamic retardation is considered.

We shall now examine some representative colloid trajectories. Figure 3.10(a) shows 10 colloid trajectories within a $y-z$ slice defined by $59\delta \leq x \leq 61\delta$ (i.e., a thickness of 10 μm). This slice contains the centers of the glass beads in the 16-beads layers. Although the slice is centered at the contact point of the 9-beads layer, the finite thickness of the slice implies a finite size of the 9-bead layer is intercepted, in this case, the projected radius is $\sqrt{100^2 - 95^2} = 0.312R$. More precisely, a range of interceptions from 0 to $0.312R$ are made, this is why a filled circle is drawn around the centers of the glass beads in the 9-beads layer. In contrast, the range of interceptions for the 16-beads layer is from R to $\sqrt{100^2 - 5^2} = 0.9987R$, so a thin line is drawn there. The $x-$axis points out of the paper. Each trajectory is marked by a different color and an identification number. A fixed time interval of $0.064s$ is used to plot the locations of a colloid on a trajectory. Colloid 1 in Figure 3.10(a) enters the cell in the negative x direction (such detail can only be obtained by zooming in the trajectory), then stays in the slice and moves along a curved streamline first upward (diverging streamlines seem

(a)

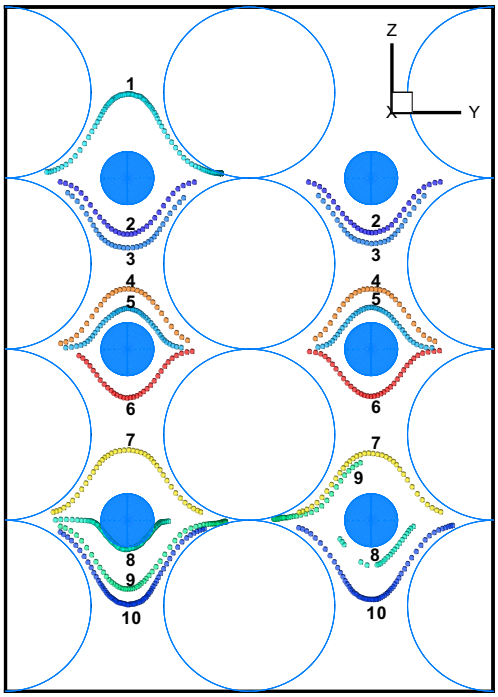

(b)

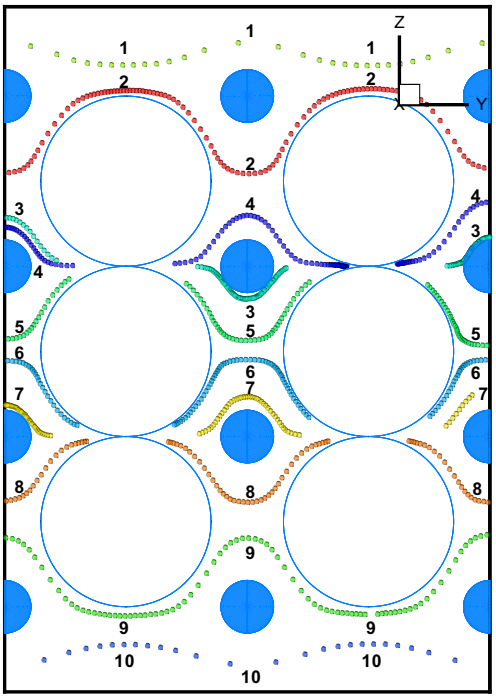

Figure 3.10: 3D trajectories seen within a narrow 2D slice of thickness 10 μm: (a) for a slice with $59\delta \leq x \leq 61\delta$, where glass beads in the 16-beads layer contact each other; (b) for a slice with $79\delta \leq x \leq 81\delta$, where glass beads in the 9-beads layer contact each other.

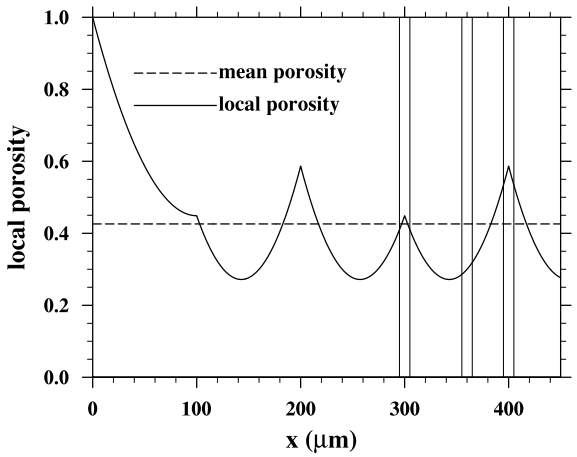

Figure 3.11: Local porosity as a function of x. The three pairs of vertical lines mark the slices considered in Figure 3.10 and Figure 3.12.

in the y-z plane) then downward (converging in the y-z plane). When it approaches the converging zone, it gets deposited there (within SEM well). Most of the colloids (Colloids 2 to 7, and 10) find a more optimal flow region in between the glass beads and move more quickly (judged by the larger spacing between consecutive locations). In fact, they leave the slice temporally to avoid the strong convergence zone in the slice and re-enter the slice at a later time. Colloid 8 travels very slowly near the contact point in the 9-beads layer but eventually leaves that region. Colloid 9 travels into the convergence zone near the contact point in 16-bead layer, and comes very close to the glass-bead surface, but it was not captured. The above suggests that the convergence zone near the contact point is likely the preferred site for colloid attachment.

Figure 3.10(b) shows 10 colloid trajectories within a $y - z$ slice defined by $79\delta \leq x \leq 81\delta$. This slice contains the centers of the glass beads in the 9-beads layers. In this case, colloids (1,2,9,10) can travel very easily near the channel walls due to large local porosity. Away from the wall regions, the trajectories are similar to Figure 3.10(a).

The colloid trajectories shown in the two slices in Figure 3.10 are mostly two-dimensional because the two slices are located in region of high local porosity (larger than the mean porosity) as illustrated in Figure 3.11. Figure 3.10(a) corresponds to

$295\mu m \leq x \leq 305\mu m$ and Figure 3.10(b) for $395\mu m \leq x \leq 405\mu m$.

Figure 3.12 shows 10 trajectories within a $y-z$ slice defined by $71\delta \leq x \leq 73\delta$. In this slice, glass beads in 16-beads (or 9-beads) layers do not touch one another, but glass beads in the 16-beads layer are in contact with those in the 9-beads layer. The range of interception radii is $0.760R$ to $0.835R$ for the 16-beads layer, and $0.893R$ to $0.937R$ for the 9-beads layer. There is a strong cross flow (relative to the streamwise flow velocity) in this slice due to the layer-layer contact blocking, so colloids do not stay very long in this slice, rather they wander in and out of this slice frequently. Note that the average porosity (0.300) in this slice is lower than the mean porosity (0.426). The slice is also shown in Figure 3.11, we note that the porosity increases with x locally so the cross flow tends to be directed to the positive x direction (out of the paper).

The above pore-scale visualizations do not provide any details on the motion of colloids near a grain surface. Furthermore, Brownian motion does not show up since the motion caused by the fluid flow dominates thetrajectories visualized at the pore scale in Figure 3.10 and 3.12. Next, we shall probe into the region in the grain surface. Figure 3.13 shows two representative trajectories, using a deposited colloid from Run 1 and Run 2. The gap distance from the grain surface is plotted as a function of time. Several important observations can be made here. First, since these two deposited colloids happened to be injected at an exact same location, their trajectories are similar initially. At about $h_{gap} = 1100\ nm \approx 2a_c$, the effect of hydrodynamic retardation started to separate the two trajectories, with hydrodynamic retardation slows down the approach to the grain surface. This is seen clearly by the different slopes of the two trajectories. Second, the fluctuations are caused by the Brownian motion. A close examination reveals that the fluctuations are reduced as the colloids make its way to the surface, this reduction of the level of fluctuations is also due to the hydrodynamic retardation effect — a drag larger than the Stokes drag causes a smaller movement of the colloid when hit by thermal fluctuation force. In the Eulerian approach when the concentration is solved, the hydrodynamic retardation decrease the effective diffusion coefficient, as seen in the study of Yang *et al.* (1998). Third, right

before deposition, the approach speed is increased due to increased van der Waals force near the SEM well. Finally, Figure 3.13(b) shows the time evolution of gap distance after the colloids are captured by the SEM well. Colloids can move around the SEM due to Brownian energy, but cannot escape the SEM well as the depth of SEM well is $-15.25kT$. Interestingly, without the hydrodynamic retardation, the trajectory shows a quasi-periodic oscillation with a time period of about 2×10^{-4} s or about $0.3125\tau_c^*$. This period is roughly 625 time steps, so it must have been fully resolved. Qualitatively, we may expect a physical oscillation around SEM as the DLVO force changes direction there, if the viscous drag (the damping) is weak. We will show this is the case below.

Figure 3.14 shows the drag force, DLVO force, and Brownian force for the same colloid from Run 2 discussed in Figure 3.13(b) after the capture by SEM. Brownian force is by far the most dominant force. Due to its short time scale and large relative magnitude, Brownian force is plotted only for a small time duration in Figure 3.14(b). The drag force shows intermediate magnitude and time scale of oscillation, showing that colloids frequently change its velocity direction. We note that the drag force shown in Figure 3.14 is about a factor 5 larger than the drag force experienced by colloids when they are in the inner pore region (i.e., flow region not very close to the grain surface), due to the significant augmentation by local hydrodynamic interaction, although the relative velocity between the colloid and the flow in the inner pore region is much larger. The DLVO force only depends on location, having the smallest magnitude and longest time scale of oscillation. The above picture clearly shows that Brownian motion is the driving force for the random motion after the capture.

Finally, Figure 3.15 shows the drag force, DLVO force, and Brownian force for the same colloid from Run 1 discussed in Figure 3.13(b) after the capture by SEM. In this case, without the hydrodynamic retardation, the colloid can move more freely around SEM, the DLVO force becomes comparable in magnitude as the Brownian force, and the drag force which acts as damping is negligible. This then implies that the system can oscillate with a period on the order of $T = 2\pi\sqrt{(\tau_c^*/(3.125 \times 10^5))/(kU_s)} \approx 7.87 \times 10^{-4}\sqrt{k}$, where $k\zeta U_s$ is the spring constant corresponding to the local average

slope shown in Figure 3.9(b) near SEM. An estimate from Figure 3.9(b) for k is $k = 15\zeta U_s$ (N/nm). Then the period of the oscillation is $T = 2.03 \times 10^{-4}$ s, precisely the period observed in Figure 3.13(b).

In summary, we present preliminary results on microscopic viscous flow simulation in a 3D porous channel and on the transport of sub-micron colloids in a model porous medium. Two numerical methods, namely, the MRT-LBE method and the hybrid Physalis approach, are applied simultaneously to solve the same viscous flow problem in a porous channel. Results from the two methods were shown to be in qualitative agreement, while the mesoscopic MRT-LBE approach demonstrated better accuracy than the macroscopic Physalis method, especially in the presence of multiple grain-grain and grain-wall contacts.

Upon the fully resolved porous media flow, we then track the deposition and migration of colloids in the bulk suspension using a Lagrangina approach. At the given solution ionic strength and physicochemical setting, no deposition at the primary energy minimum was found due to the presence of extremely high energy barrier. Instead, retention by the shallow secondary energy minimum (SEM) well was detected. Careful examination shows that the local hydrodynamic interaction between colloid and grain surface defers the process of colloid deposition in the SEM, but does not prevent it to occur. Prior to being captured by the SEM, the colloid trajectories are shown to be dependent on the local porosity, flow convergency, and contact points. At large local porosity, the colloid trajectory is quasi-two-dimensional, whereas at small local porosity, the variation in trajectory becomes much more acute. After the colloids being captured by the SEM well, the local hydrodynamic interaction plays an important role in suppressing the quasi-periodic motion, which is induced by the combined effect of particle inertia and DLVO forces near SEM.

(a)

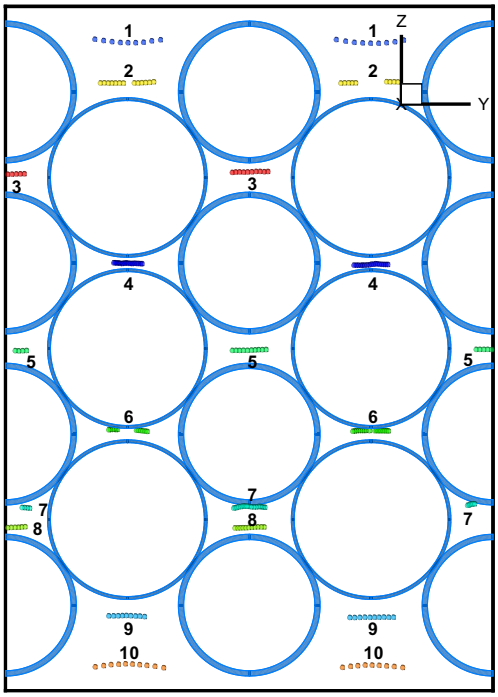

(b)

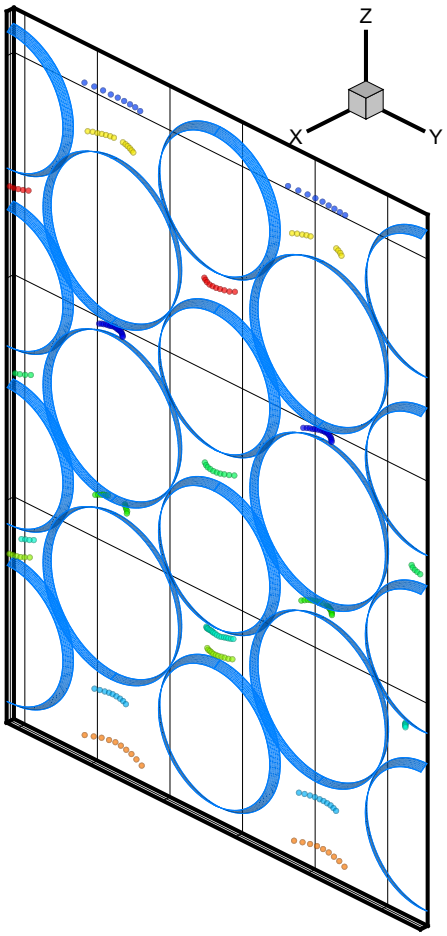

Figure 3.12: 3D trajectories seen within a narrow 2D slice of thickness 10 μm for a slice with $71\delta \leq x \leq 73\delta$: (a) 2D view; (b) 3D view.

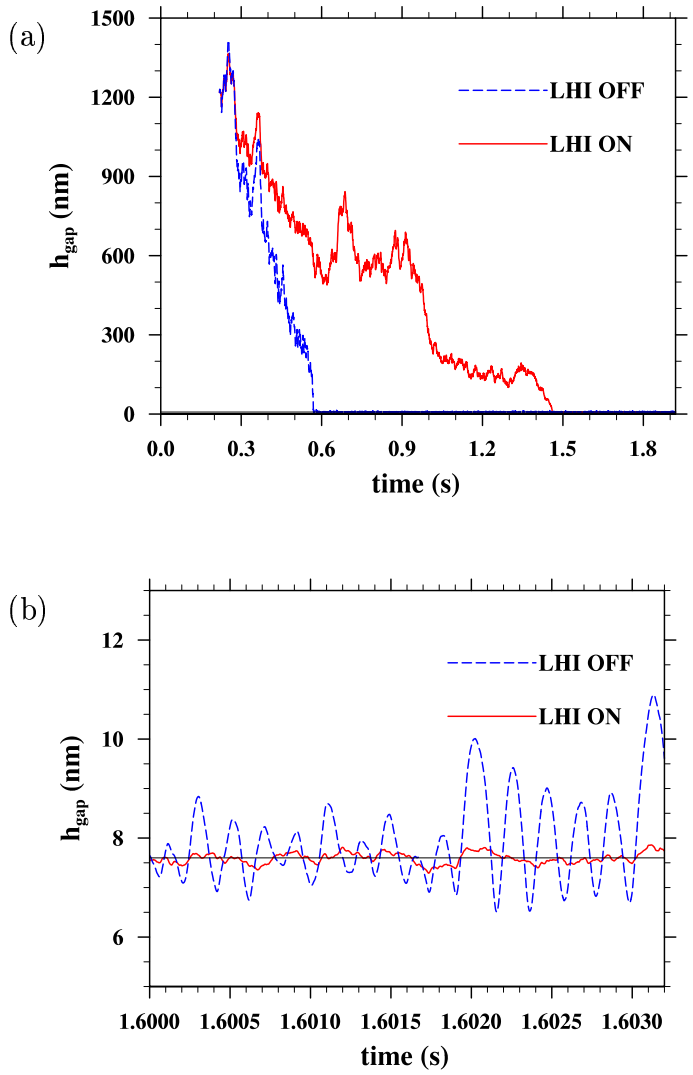

Figure 3.13: Gap distance between a colloid and a collector surface as a function of time: (a) from the moment of release to the SEM deposition; (b) a zoom-in view after the capture of colloids by SEM well. The horizontal line represents the SEM location of $7.58nm$ at the given ionic strength of $0.1M$.

(a)

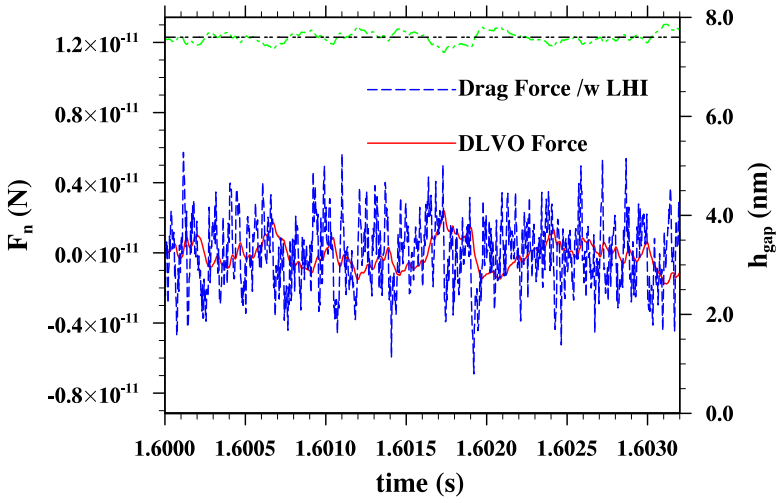

(b)

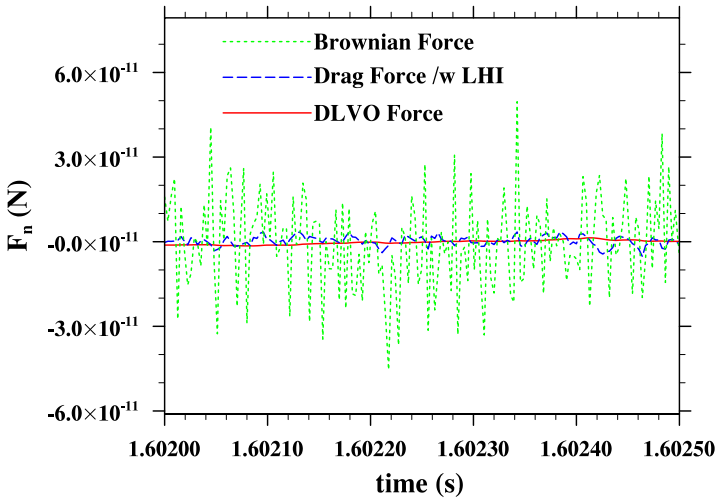

Figure 3.14: Forces acting on a colloid with LHI after the capture by the SEM well: (a) drag force and physicochemical force as a function of time, and the corresponding gap distance; (b) a zoom-in portion of (a), including drag force, physicochemical force, and Brownian force.

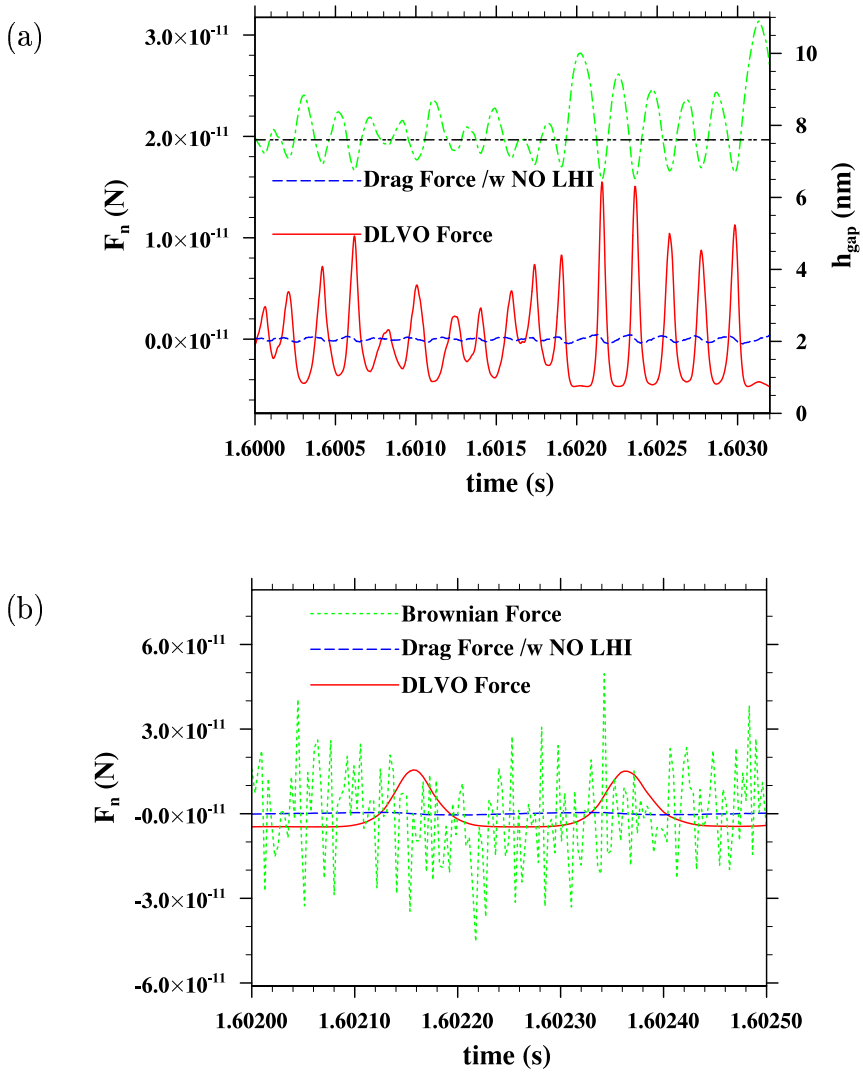

Figure 3.15: Forces acting on a colloid without LHI after the capture by the SEM well: (a) drag force and physicochemical force as a function of time, and the corresponding gap distance; (b) a zoom-in portion of (a), including drag force, physicochemical force, and Brownian force.

Chapter 4

LATTICE BOLTZMANN SIMULATION OF TURBULENT FLOW LADEN WITH FINITE-SIZE PARTICLES

In this chapter, we develop a particle-resolved simulation method and apply it to study turbulent flow laden with finite size particles. The method is based on the multiple-relaxation-time lattice Boltzmann equation. The no-slip boundary condition on the moving particle boundaries is handled by a second-order interpolated bounce-back scheme. The populations at a newly converted fluid lattice node are constructed by the equilibrium distribution with non-equilibrium corrections. MPI implementation details are described and the resulting code is found to be computationally efficient with a good scalability. The method is first validated using unsteady sedimentation of a single particle and sedimentation of a random suspension. It is then applied to a decaying isotropic turbulence laden with particles of Kolmogorov to Taylor microscale sizes. At a given particle volume fraction, the dynamics of the particle-laden flow is found to depend mainly on the effective particle surface area and particle Stokes number. The presence of finite-size inertial particles enhances dissipation at small scales while reducing kinetic energy at large scales. This is in accordance with related studies. However, the normalized pivot wavenumber is found to not only depend on the particle size, but also on the ratio of particle size to flow scales and particle-to-fluid density ratio. Further examination of local profiles illustrates strong turbulent modulation within half particle radius to the particle surface, as well as self-similarity of the profiles with proper scaling.

4.1 Introduction

Turbulent particle-laden flows have seen their occurrence and applications in a large number of natural and industrial processes. Over the past two decades, significant efforts have been devoted to advance computational and experimental methods in order to quantify the interactions between the dispersed particle phase and the carrier fluid phase. Since turbulent particle-laden flows usually encompass a wide range of length and time scales, it is computationally demanding to simultaneously resolve both the carrier-phase turbulent flow and the disturbance flows due to the particles. A common practice is to employ the point-particle model so that the computational cost can be substantially reduced. The point-particle model implicitly assumes that the particle size is much smaller than the Kolmogorov length scale of the carrier fluid turbulence, and particle Reynolds number is small so the disturbance flow around a particle is a Stokes flow. Using this approach, substantial progress has been made towards studies on preferential concentration of inertial particles, turbulent modulation by inertial particles, and turbulent collision rate of inertial particles.

Despite the successful application of the point-particle model, its validity is often questionable when particle mass loading is significant or particles form aggregates yielding strong multiscale couplings between the particulate phase and the carrier phase. Furthermore, in many engineering applications, particle size can be of the same order as or larger than Kolmogorov scale. The scales contained in the disturbance flows then overlap with the scales of motion in the carrier turbulence. In this situation, the point-particle model is no longer a valid description and the finite-size effect of the dispersed phase must be resolved together with the carrier fluid turbulence.

The motivation of this work is to understand the motion and hydrodynamic interactions of finite-size inertial particles suspended in a turbulent flow. One of the major challenges is to develop an efficient and accurate approach to resolve the disturbance flows around particles suspended in a turbulent carrier fluid.

In recent years, several computational methods have been proposed along this direction. Examples include the arbitrary Lagrangian-Eulerian-based finite element

method, fictitious domain method, immersed boundary method, force coupling method, hybrid Physalis method, the mesoscopic lattice Boltzmann method (LBM), and its variation, the immersed-boundary-lattice-Boltzmann method. More details about these methods are described in Chapter 1.

To date, many of the above-mentioned particle resolved simulation methods have been applied to study particle-particle interaction or particulate suspension in a non-turbulent fluid (Qi, 1999; Ding and Aidun, 2000; Nguyen and Ladd, 2002; Climent and Maxey, 2003), but with only a few studies on turbulent particle-laden flows. In this case, the challenge is the multiscale nature involving a wide range of scales from the integral scale of the background turbulence to the scales of disturbance flows around each particle. For this reason, particle resolved simulation of turbulent particle-laden flows requires the state-of-the-art supercomputers.

The main objectives of this work are to describe our own implementation of LBM using interpolated bounce back and to present our preliminary results. Following the description of the simulation method, we first validate our code using unsteady sedimentation of a single particle. We then apply the method to study statistics in a random suspension at finite particle Reynolds numbers and compare our results with those reported in Climent and Maxey (2003). The main results concern decaying turbulent flows laden with finite-size particles. We first show that our method can reproduce the results for a single fixed particle residing in dacaying turbulence in Burton and Eaton (2005), and then demonstrate the capability of our method in capturing the interactions between several thousands of freely moving particles and turbulent flows in Lucci *et al.* (2010). A key new physical result discussed is the dependence of normalized pivot wavenumber on the dimensionless particle size. Timing and scalability of the code are also briefly discussed.

4.2 Simulation Method

In this section, we first introduce the lattice Boltzmann approach aimed at simulating a turbulent flow laden with finite size particles. Due to the high computational

demand, the code needs to be parallelized to run on a scalable computer such that results can be obtained in a timely manner. Hence the MPI implementation of the code represents an important effort. We will describe the general strategy and some specific details related to the MPI implementation in order to achieve a good computational efficiency.

4.2.1 Lattice Boltzmann Simulation

In this study, the mesoscopic lattice Boltzmann approach, based on the multiple-relaxation-time (MRT) lattice Boltzmann equation (LBE) (d'Humières *et al.*, 2002), is applied to simulate decaying homogeneous isotropic turbulence laden with finite size spherical particles in a three-dimensional periodic domain. In the MRT-LBE, the mesoscopic particle distribution function at a fluid lattice point is governed by

$$\mathbf{f}(\mathbf{x}+\mathbf{e}_i\delta_t, t+\delta_t) = \mathbf{f}(\mathbf{x},t) - \mathbf{M}^{-1}\cdot\mathbf{S}\cdot\left[\mathbf{m}-\mathbf{m}^{(\mathrm{eq})}\right], \tag{4.1}$$

where $\mathbf{M}$ is an orthogonal transformation matrix converting the distribution function $\mathbf{f}$ from discrete velocity space to the moment space $\mathbf{m}$, in which the collision relaxation is performed. The transformation between the particle velocity space and the moment space is given as

$$\mathbf{m} = \mathbf{M}\cdot\mathbf{f}, \qquad \mathbf{f} = \mathbf{M}^{-1}\cdot\mathbf{m}. \tag{4.2}$$

The diagonal relaxation matrix matrix $\mathbf{S}$ specifies the relaxation rates for the non-conserved moments. In this work, the D3Q19 model is utilized with the discrete velocities ordered as

$$\mathbf{e}_i = \begin{cases} (0,0,0), & i=0, \\ (\pm1,0,0),(0,\pm1,0),(0,0,\pm1), & i=1-6, \\ (\pm1,\pm1,0),(\pm1,0,\pm1),(0,\pm1,\pm1), & i=7-18. \end{cases} \tag{4.3}$$

The corresponding 19×19 transform matrix $\mathbf{M}$, the 19 components of moment $\mathbf{m}$ and its equilibrium counterpart $\mathbf{m}^{(\mathrm{eq})}$, and the relaxation matrix $\mathbf{S}$ are described in detail in d'Humières *et al.* (2002) and Chapter 2 of this dissertation.

The macroscopic hydrodynamic variables, including density, momentum, and pressure, are obtained from the moments of the mesoscopic distribution function $\mathbf{f}$, namely,

$$\rho = \rho_0 + \delta\rho, \quad \rho_0 = 1 \tag{4.4}$$

$$\delta\rho = \sum_i f_i, \quad \rho_0 \mathbf{u} = \sum_i f_i \mathbf{e}_i, \quad p = \delta\rho c_s^2 \tag{4.5}$$

where $\mathbf{u}$ is the macroscopic fluid velocity, and the sound speed c_s is equal to $1/\sqrt{3}$ in lattice units.

The computation domain is covered with a uniform cubic lattice. The periodic boundary condition is applied in all three directions. The no-slip boundary condition on solid particle surfaces are implemented using a second-order interpolated bounce-back scheme (Lallemand and Luo, 2003a). First, for each fluid node near a particle surface, all the links moving into the surface of a solid particle are identified, and the boundary-cutting location on the link is calculated in terms of the percentage (q) of the link outside the surface. For better numerical stability, when $q \leq 0.5$, the interpolation is performed before streaming, while for $q > 0.5$, it is done after streaming (Lallemand and Luo, 2003a). When two particles are in close contact, two fluid lattice nodes may not be available near the missing population to allow for a second-order interpolation. In this case, a linear interpolation or a simple on the node bounce back is used instead. For a moving solid boundary, the boundary links have to be identified and q has to be updated for each time step.

In our implementation, the above LBE evolution only applies to the fluid nodes where the particle distribution functions are defined. No distribution function is defined for solid lattice nodes lying within the particles. When a particle is moved, a solid node may move out of the solid region and become a fluid node with unknown distribution functions. In this work, all the 19 particle distribution functions for the new fluid

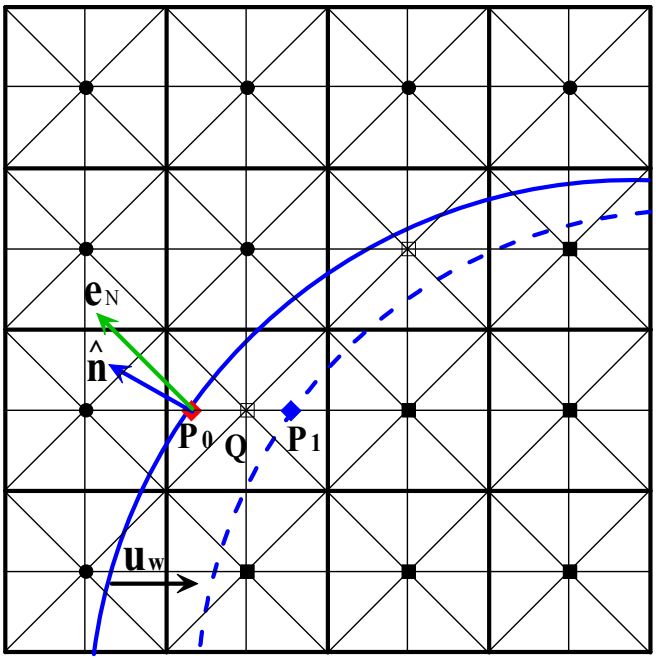

Figure 4.1: A two-dimensional sketch illustrates how the lattice velocity direction $\mathbf{e}_N$ is defined, for the purpose of implementing the non-equilibrium correction. The filled circles denote fluid lattice nodes at the beginning of a time step, filled squares are solid lattice nodes, and the open squares represent newly created fluid lattice nodes. The thick curve represents the solid surface at the beginning of the time step, and the dashed curve the new particle surface at the end of the time step.

node are constructed by an equilibrium distribution plus a nonequilibrium correction (Caiazzo, 2008), namely,

$$f_i(\mathbf{x}) = f_i^{(eq)}(\mathbf{x}; \mathbf{u}_w, \bar{\rho}) + f_i^{(neq)}(\mathbf{x} + \mathbf{e}_N) \tag{4.6}$$

where $\mathbf{u}_w$ is the velocity of the moving boundary at the new fluid node Q (Figure 4.1) using the center, translation and angular velocity of the solid particle at the end of time step, $\bar{\rho}$ is the fluid density averaged over all the existing fluid nodes found in the immediate neighborhood using the density value based on the latest distribution functions. On extremely rare occasion when multiple solid particles are almost in contact, no single neighborhood fluid node is available; in this case, $\bar{\rho}$ is set to ρ_0. Since the magnitude of $\mathbf{u}_w$ is assumed to be much smaller than the sound speed c_s, in reality, the three points P_0, Q, and P_1 in Figure 4.1 are very close to one another.

While the equilibrium part is calculated with $\mathbf{u}_w$ and $\bar{\rho}$ at $\mathbf{x}$, the non-equilibrium part is obtained from a neighboring node at $\mathbf{x}+\mathbf{e}_N$. Here the $\mathbf{e}_N$ is a specified discrete velocity along which direction the quantity $\hat{\mathbf{n}}\cdot\mathbf{e}_N$ takes the maximum value (Figure 4.1), where $\hat{\mathbf{n}}$ the unit normal vector pointing outwards of the moving boundary at the point P_0 through which the solid node Q at the beginning of a time step will cross the particle surface to enter the fluid domain. The equilibrium population is calculated as

$$f_i^{(eq)}(\mathbf{x},t) = W_i\left[\rho + \frac{\rho_0 \mathbf{e}_i\cdot\mathbf{u}}{{c_s}^2} + \frac{\rho_0 \mathbf{u}\mathbf{u}:(\mathbf{e}_i\mathbf{e}_i - {c_s}^2\mathbf{I})}{2{c_s}^4}\right] \tag{4.7}$$

where $\mathbf{I}$ is the identity matrix, and the weight W_i is given as

$$W_i = \begin{cases} 1/3, & i = 0, \\ 1/18, & i = 1-6, \\ 1/36, & i = 7-18. \end{cases} \tag{4.8}$$

Our numerical tests suggested that the refilling technique as given by Eq. (4.6) yielded smaller force oscillations when compared to other methods such as the extrapolation method used in Lallemand and Luo (2003a).

The hydrodynamic force $\mathbf{F}_i$ acting on the ith particle is calculated during the interpolated bounce-back procedure by summing up the loss of fluid momentum on all the links across the surface of the ith particle, and the torque $\mathbf{\Gamma}_i$ acting on the ith particle is the sum of the cross product of the local position vector relative to the center of the particle and the loss of fluid momentum, over all boundary links. This ensures that the net loss (or gain) of momentum by the fluid lattice particles is exactly equal to the gain (or loss) of momentum of the solid particles, so the total momentum of the system is conserved. This represents a unique advantage of LBM as it avoids spatial differentiations that would be needed for computing the net hydrodynamic force and torque on each solid particle in terms of local stress distribution on the particle surface, for Navier-Stokes based CFD methods.

In case particles are in close contact, the flow in the narrow gap between the particles is no longer fully resolved. The physical lubrication force, which is proportional to the radial relative velocity and inversely proportional to the gap distance, cannot

be directly simulated. One could add, by empirical tuning, the portion of physical lubrication force that is not resolved to the portion that is directly resolved, as was done in Nguyen and Ladd (2002). Since the lubrication force changes rapidly with the gap distance and a finite time step must be used, a more effective approach to prevent particles from overlap due to under-estimation of the physical lubrication force is to introduce a soft-sphere like short-range repulsive force. In this preliminary study, we simply adopt the following pair-wise repulsive force acting on the ith particle due to its interaction with jth particle (Glowinski *et al.*, 2001; Feng and Michaelides, 2005)

$$\mathbf{F}_{ij} = \begin{cases} 0, & r_{ij} > R_{ij} + \zeta, \\ \frac{c_{ij}}{\varepsilon_p} \left(\frac{r_{ij} - R_{ij} - \zeta}{\zeta} \right)^2 \left(\frac{\mathbf{r}_{ij}}{r_{ij}} \right), & r_{ij} \leq R_{ij} + \zeta \end{cases} \tag{4.9}$$

where $\mathbf{r}_{ij} \equiv \mathbf{Y}_i - \mathbf{Y}_j$, $r_{ij} \equiv \|\mathbf{Y}_i - \mathbf{Y}_j\|$, $R_{ij} \equiv R_i + R_j$, c_{ij} is a force scale and is set to be the buoyancy force in this study. $\mathbf{Y}_i$ and $\mathbf{Y}_j$ represent the center location of the ith and jth particle with radius of R_i and R_j, respectively. ζ is a threshold gap distance within which the model repulsive force becomes active. In this work, ζ is set as two lattice spacing. The stiffness parameter, ε_p, is set to be small enough to prevent particles from overlapping.

At each time step, with the resolved hydrodynamic force, repulsive force, and torque acting on particles readily obtained, the particle translational and angular velocities, center position and angular displacement are updated using the Crank-Nicolson scheme for particle position and angular displacement integration and the forward Euler scheme for velocity and angular velocity (with force and torque being averaged over the two half time steps to reduce fluctuations),

$$\mathbf{V}_i^{t+\delta t} = \mathbf{V}_i^t + \frac{1}{M_p} \left(\frac{\mathbf{F}_i^{t+\delta t/2} + \mathbf{F}_i^{t-\delta t/2}}{2} + \sum_j \mathbf{F}_{ij}^t \right) \delta t, \tag{4.10}$$

$$\mathbf{\Omega}_i^{t+\delta t} = \mathbf{\Omega}_i^t + \frac{1}{I_p} \left(\frac{\mathbf{\Gamma}_i^{t+\delta t/2} + \mathbf{\Gamma}_i^{t-\delta t/2}}{2} \right) \delta t, \tag{4.11}$$

$$\mathbf{Y}_i^{t+\delta t} = \mathbf{Y}_i^t + \frac{1}{2} \left(\mathbf{V}_i^t + \mathbf{V}_i^{t+\delta t} \right) \delta t, \tag{4.12}$$

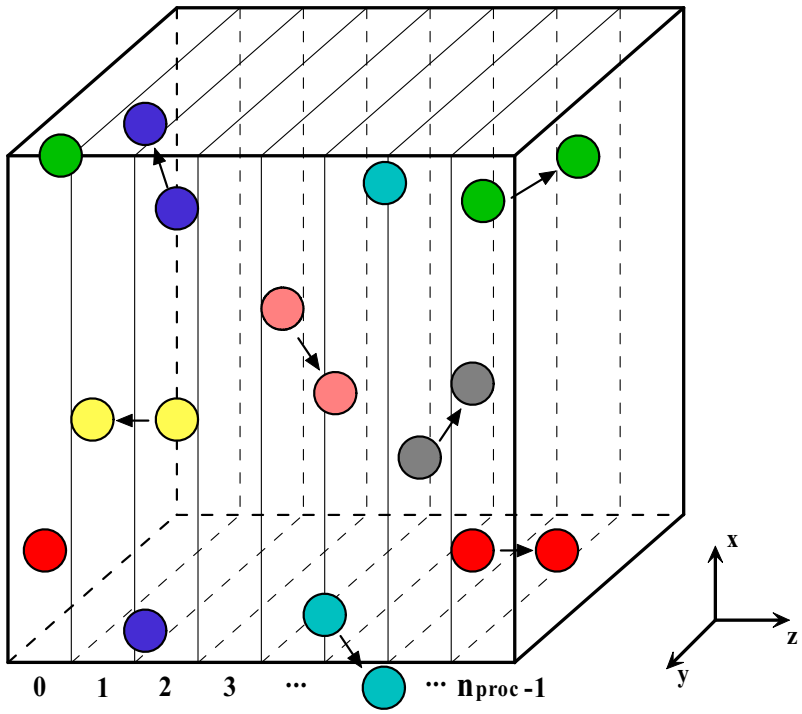

Figure 4.2: 1D domain decomposition and periodic boundary condition manifested by particle movement.

$$\mathbf{\Theta}_i^{t+\delta t} = \mathbf{\Theta}_i^t + \frac{1}{2}\left(\mathbf{\Omega}_i^t + \mathbf{\Omega}_i^{t+\delta t}\right)\delta t \tag{4.13}$$

where M_p and $I_p \equiv \frac{2}{5}M_p^2 R_i^2$ are the mass and moment of inertia of the ith particle.

To summarize, for each time step, the sequence of operations is as follows: (1) MRT collision step, (2) interpolation of populations needed for bounce back on the solid particle surfaces and calculations of force and torque acting on each solid particle, (3) streaming, (4) computation of solid particle short-range repulsive interaction forces, (5) updating solid particle locations and velocities, (6) updating lattice links cutting through solid particle surfaces, (7) refilling populations for the new fluid nodes, (8) updating hydrodynamic variables, and (9) updating fluid flow and solid particle statistics.

4.2.2 MPI Implementation

The computational domain of the periodic box is decomposed in a given direction, e.g., the z direction, as shown in Figure 4.2, producing a sequential set of slabs of dimension $(nx, ny, nz/n_{proc})$, where nx, ny, and nz are the lengthscales in units of lattice spacing in x, y, z direction, respectively, and n_{proc} is the number of processes employed. Each of these slabs is mapped to an individual process according to its sequential number, and this one-to-one mapping is fixed during the computation. For example, process 0 takes charge slab 0, process 1 corresponds to slab 1, and so on. Since the 2nd-order interpolated bounce-back scheme may utilize the information of two adjacent layers of fluid lattice nodes in the z direction to construct the missing population at a lattice node in the immediate vicinity of a solid surface, the minimum slab size has to be 2 lattice units in order to limit the data communication to neighboring slabs only. This implies that, for the particle-laden flow simulation, the maximum number of processes that can be utilized is $nz/2$ for our one-dimensional domain decomposition approach. Multiple-dimensional domain decomposition should be explored in the future to allow the use of a much larger number of processes.

The initial positions for the freely-moving particles are generated by a master process, say, process 0, via a random number generator. The use of a fixed seed for random number generation on only the master process ensures the repeatability of the initial positions of the particles. The particles are then distributed to different processes according to the z component of their center locations. If the center of a particle is found to be moved to its neighboring slab at the end of a time step, all other data related to this particle including its global index, center position, angular displacement, force and torque acting on the particle, and translational and angular accelerations, are transferred together to the neighboring slab. In addition to the global particle index, a local particle index is also employed within each slab, to accelerate certain operations involving particles belonging to the same process, for example, the calculation of particle-particle repulsive force, the update of particle dynamic evolution, and the re-ordering of particles in a slab after some new particles moving in and some

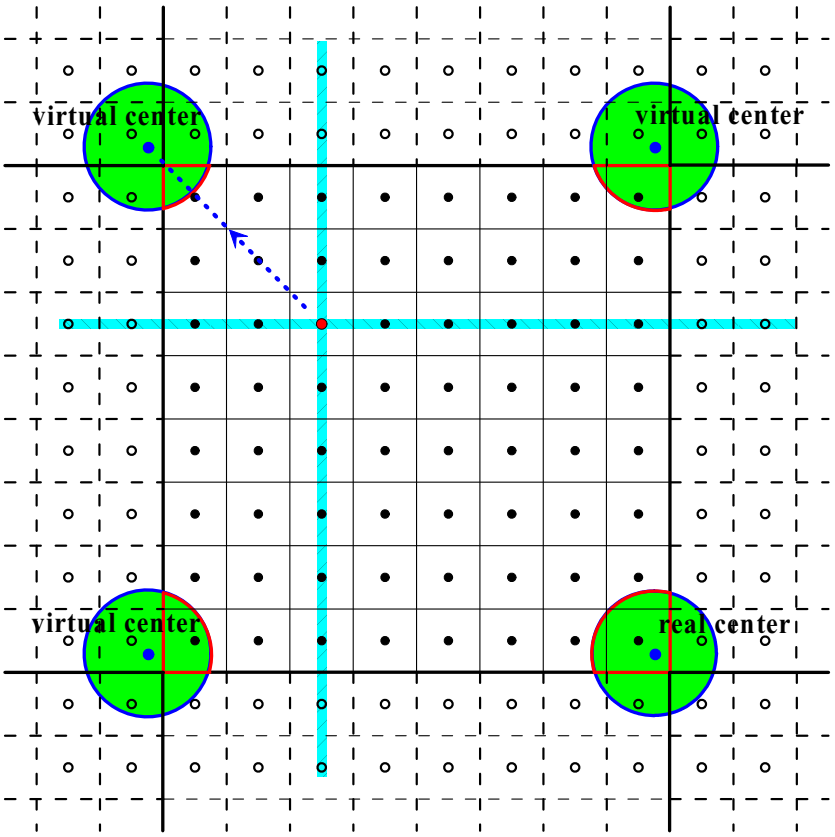

Figure 4.3: A 2D schematic used to illustrate the essential concept of the efficient scheme for computing the minimum distance of a lattice node to the center of a solid particle, regardless where the solid particle is located. In this figure, the center of the solid particle is located close the lower right corner of the domain, representing one of the most challenging situations. The three periodic images of the solid particle are also shown, with virtual centers located outside the domain near the other three corners. The red dot represents any lattice node of interest. By simply comparing the coordinate of the real particle center and that of the node, one can divide the domain into four quadrants (in 2D) and then easily find the nearest particle center to the lattice node of interest, and thus the shortest particle-to-node distance. In the figure, the nearest particle center to the red dot is the one located in the upper left quadrant.

old particle leaving the slab.

Comparing with the point-particle based simulation, one of the most challenging issues for finite-size particles is on the comprehensive and efficient handling of the scenario when a particle is crossing the computational domain boundary. For instance,

as illustrated in a 2D schematic shown in Figure 4.3, a particle could be close to a corner of the cubic box, thus its volume could be distributed into eight portions (four in 2D), each of which residing in one of the corners due to the periodic boundary conditions applied in all directions. Clearly each portion of the particle can have either a real center located inside or virtual particle centers located outside the computational domain. Since LBM requires a lattice node to be classified as a fluid node within the fluid region or a solid node inside a solid particle, it is necessary to calculate the minimum distance from the solid particle center to the lattice node of interest. A straightforward method is to calculate and compare all eight distance from the lattice node to the real center and seven virtual centers, but it would be cumbersome.

A much more efficient scheme to find this minimum distance is as follows. First, the x coordinate of the lattice node x_{node} is compared with the x-component of the position of the real particle center x_{part} , which is located within the computational domain. The following three-step procedure allows this minimum distance to be computed. First, if $x_{part} - x_{node} > nx/2$, then the replacement of x_{part} by a virtual x center at $x_{part} - nx$ would provide the minimum separation in magnitude in the x direction. Second, if $x_{part} - x_{node} < -nx/2$, then the replacement of x_{part} by a virtual x center at $x_{part} + nx$ would provide the minimum separation in the x direction. Third, if $-nx/2 \leq x_{part} - x_{node} \leq nx/2$, the use of a real particle center is adequate. The essence of this operation is to ensure that the magnitude of the separation in the x direction is no larger than $nx/2$. This procedure is repeated in the y and z directions, together they provide an efficient method to compute the minimum distance of a lattice node to the particle center, requiring only one-time calculation of projected distance in each spatial direction instead of eight times. Another benefit of this algorithm is that it can handle any particle size relative to the slab width, as long as the particle diameter is less than half of the computational domain size.

This algorithm has been applied extensively and consistently in the code to reduce computational effort, such as the detection of particle overlap, construction of the lattice links crossing the solid particle boundary, calculation of the interpolated

bounce-back on particle surfaces, particle-particle repulsive force, and refilling of the missing populations for the newly-generated fluid lattice nodes.

It is a common practice in an MPI code to have variables localized as much as possible to reduce the memory usage and consequently the time to access memory, which would lead to a higher computational efficiency. However, there exist circumstances that a global variable is preferred, in order to save communication time in between processes and to simplify the code structure.

In this code, a small number of solid particle arrays are set to global arrays, including the array of particle center position, translational and angular velocity, and particle-particle repulsive force. This treatment introduces redundancy and a small impact on data communication, but the extra memory requirement is almost negligible when compared to other large local arrays already allocated in the same process. For example, suppose the the code is set to contain 1 million particles and run at grid resolution of 1024^3 with 512 processes, thus the local distribution function has a dimension of $f(19, 1024, 1024, 2)$, and the global array of particle position is $yp(3, 1M)$. With double precision, the former alone would occupy memory of $19 \times 1024 \times 1024 \times 2 \times 8/1024^2 = 304MB$, while the latter consumes $3 \times 1M \times 8/1024^2 = 24MB$, which has only a marginal effect on the total memory usage, but eliminates the need for data communication.

Since the dispersed phase can move freely in the carrier flow, the boundary links and the boundary cutting location q on each link must be updated at every time step. To identify if a fluid lattice node possesses boundary links, one needs to calculate the distance between each particle center and the node of interest. Typically with thousands of particles and millions of nodes available, the task of updating distances could be computationally intensive, if one attempts to blindly compare each node to each individual particle directly.

A solution to this problem is to only consider the fluid lattice nodes surrounding the particle surface in a confined region, e.g., a small cubic box with a lateral length of particle diameter plus four lattice spacings, which would encompass all the potential

fluid nodes with links crossing particle boundary. All the other nodes outside this range will be filtered out in a nested conditional screening as follows. First, check the x-coordinate of the node of concern, keep the node for the next level of screening if its x coordinate falls within the truncation region, otherwise drop it and turn to the next node in the x direction. This procedure is repeated in the y, and then in the z direction. This nested screening ensures that only the lattice nodes in a minimal region are considered in the search of boundary links for a given solid particle. Finally, the distances between all selected lattice nodes and the center of the solid particle are computed to identify all boundary links on the solid particle. For 256^3 lattice resolution and 6400 particles of radius of 4, tests have shown that the computational efficiency for this boundary link search algorithm is faster than the unscreened algorithm, by a factor of more than two thousand.

In summary, the above MPI implementation details yielded an overall efficient MPI code for particle-resolved simulation of turbulent particle-laden flows, as will be demonstrated by timing and scalability data to be presented in the next section.

4.3 Results

In this section, we will first present results from code validation simulations involving a single particle and a random suspension in a non-turbulent background carrier flow. The results for a decaying turbulent particle-laden flow will then be discussed to demonstrate the capability and computational efficiency of the approach. Preliminary results concerning turbulence modulation by finite-size solid particles will be provided to reveal the effects of particles on the energy spectrum of the turbulent flow and on the spatial distribution of dissipation rate around a solid particle.

4.3.1 Validation: Single Particle Settling

Mordant and Pinton (2000) measured the velocity of a steel bead settling under gravity ($9.8m/s^2$) in a large water tank. The steel bead was released from rest. Here we consider one of their measured cases with the diameter of the bead equal to $0.8mm$.

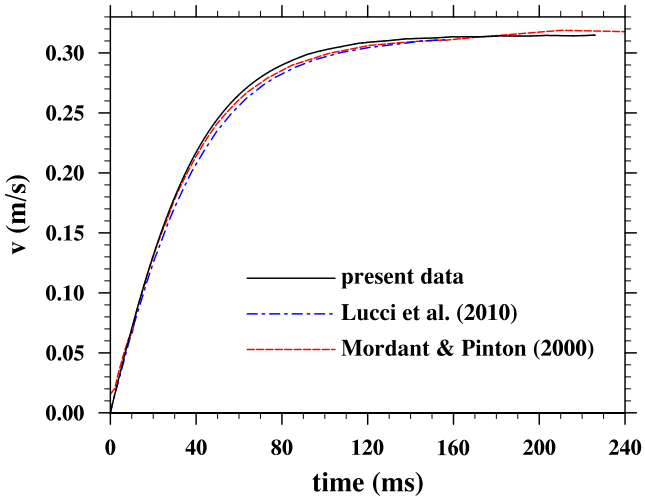

Figure 4.4: Time evolution of the velocity of a small steel bead settling under gravity in a large water tank.

The particle density is $\rho_p = 7710 kg/m^3$. The water density and kinematic viscosity are $\rho_f = 1000 kg/m^3$ and $\nu_f = 0.9 \times 10^{-6} m^2/s$. In the LBM simulation, we set the particle diameter to $d = 8$ (in lattice units). The system is governed by two dimensionless parameters: the solid particle to fluid density ratio, ρ_p/ρ_f, and the dimensionless gravity gd^3/ν^3, where g is the gravitational acceleration. These two dimensionless parameters in the LBM simulation are matched with those in the experiment. A domain size of $12.5d \times 12.5d \times 128d$ (or $100 \times 100 \times 1024$ lattice units) is used. Figure 4.4 compares the simulated settling velocity with the measured curve. Also shown is the result from Lucci *et al.* (2002) based on a finite-difference immersed-boundary scheme. In both simulations, periodic boundary conditions are assumed in all three directions. All results are in excellent agreement. The steady-state settling velocity obtained in the LBM is $0.315 m/s$ in physical units, which is very close to $0.316 m/s$ measured in Mordant and Pinton (2000). This validates our LBM particle-resolved simulation code.

To be complete, we note that, for a free sphere in an unbounded spatial domain, the wake can become unstable. In a spectral simulation of a uniform flow around a sphere in a large spatial domain, Bagchi *et al.* (2001) found steady and axisymmetric flow when the particle Reynolds number is less than 210, steady and nonaxisymmetric

flow without vortex shedding when the Reynolds number is between 210 and 270, and unsteady three-dimensional flow with vortex shedding when the Reynolds number is above 270. In our simulation, the final particle Reynolds number is 280. However, we applied periodic boundary conditions in all three directions in a finite domain, so it is not a free sphere in an unbounded domain. We suspect that the particular setup we used delayed the development of non-axisymmetric and unsteady wakes. A closer inspection showed that the particle did start to rotate towards the end of the simulation with the total angular displacements of 8.6°, 1.76°, and 0.66°, respectively, along the x, y, and z axes at the end of the simulation ($t = 0.24s$), where x and y are the horizontal directions and z is the vertical direction. The particle was also found to drift slowly in the y direction with a total translational displacement of about one particle diameter at $t = 0.24s$. A non-axisymmetric wake was also observed near the end of the simulation. It could be possible that an unsteady wake will develop if the simulation were to continue for a much longer time than what is presented in Figure 4.4.

4.3.2 Sedimentation of a Random Suspension

To further validate our implementation of LBM, we first consider a random suspension at finite particle Reynolds numbers and compare our results with those of Climent and Maxey (2003). Solid spherical particles were randomly seeded in an initially quiescent fluid domain of size 128^3. Periodic boundary conditions were applied in all three directions. A series of simulations were conducted to yield five different volume concentrations, using 1, 40, 120, 240, 480 particles of a fixed radius of 5 grid spacing. The single-particle case was used as the reference case. A volumetric body force was applied to balance the excess weight of the particles in the vertical direction. The gravitational acceleration was varied to give two different particle Reynolds numbers of roughly 4.1 and 11.2, based on the single-particle sedimentation velocity and particle diameter. The sedimentation velocity was corrected to ensure that the system has a zero net vertical mass flux. In a Stokes suspension flow, this additional correction

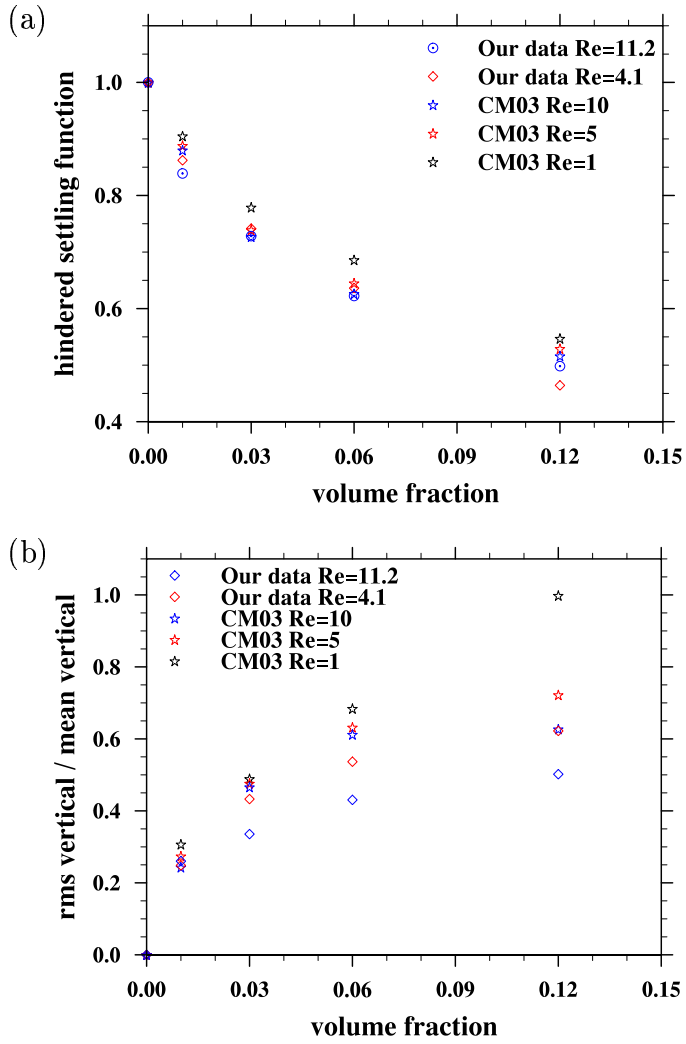

Figure 4.5: (a) Average settling velocity normalized by V_0 in 128^3 simulations: comparing the present study with Climent and Maxey (2003); (b) Fluctuation of settling velocity normalized by its mean value, V_{rms}/V_{mean}, in 128^3 simulations: comparing the present study with Climent and Maxey (2003).

would not be needed. However, in a suspension at finite particle Reynolds number, the system is no longer a linear system, a simple balance of the body force and the excess weight cannot guarantee a net zero mass flux, due to nonlinear fluid inertial effects.

An important question for a random suspension is how the mean velocity varies with the particulate volume concentration. Figure 4.5(a) shows the mean sedimentation velocity normalized by V_0, the terminal velocity of a single particle sedimenting in the

same periodic domain. The estimated statistical uncertainties of our own data are also plotted. This is known as the hindered settling function and it is plotted as a function of particulate volume fraction. Also shown are results from Climent and Maxey (2003) at particle Reynolds numbers of 1, 5, and 10. Clearly, the particle average settling velocity is significantly reduced as its volume fraction is increased, and the larger the particle Reynolds number the smaller the settling velocity. The results are in good agreement with those of Climent and Maxey (2003), with our simulations predict a somewhat smaller settling velocity. The differences could be due to two reasons. First, there are statistical uncertainties in both studies. Second, the force coupling method is an approximate method in which the disturbance flow is not fully resolved.

The relative vertical velocity fluctuations V_{rms}/V_{mean} are shown in Figure 4.5(b). The overall trends are similar: the relative vertical velocity fluctuation increases with the volume fraction, but decreases with the particle Reynolds number. Quantitatively, our simulations yield smaller values. The origin for the quantitative differences between our simulations and those of Climent and Maxey (2003) remains to be studied.

4.3.3 Decaying Turbulence Laden with a Fixed Particle

In order to further verify our LBM code, we performed a simulation of decaying homogeneous isotropic turbulence with a fixed particle. The results concerning turbulence modulation in the region near the particle are compared with those of Burton and Eaton (2005) using a finite difference method together with an overset-grid technique. In the simulation, we set a domain of 512^3 grid points with periodic boundary conditions applied in all three directions. An initial turbulent field is obtained by specifying a Gaussian field with a prescribed kinetic energy spectrum as in Burton and Eaton (2005)

$$E(k) = \left(\frac{6u_0^2}{\sqrt{\pi}}\right)\left(\frac{k^2}{k_p^3}\right)\exp\left[-\left(\frac{k}{k_p}\right)^2\right], \tag{4.14}$$

where k is the wave number, k_p is the wave number at which $E(k)$ reaches a maximum, and u_0 is the initial r.m.s. velocity. Both k and k_p have been normalized by the

minimum wavenumber $k_0 \equiv 2\pi/L_B$, where L_B is the computational domain size. The initial flow statistics can be derived from Eq. (4.14) as follows:

$$\frac{3}{2}u_{rms}^2 \equiv \int_0^\infty E\left(k\right)\mathrm{d}k = \frac{3}{2}u_0^2 \quad \text{or} \quad \frac{u_{rms}}{u_0} = 1.0, \tag{4.15}$$

$$\frac{\epsilon L_B}{u_0^3} \equiv \frac{2\nu L_B}{u_0^3}\int_0^\infty k^2 E\left(k\right)\mathrm{d}k = 18\pi^2 k_p^2 \frac{\nu}{u_0 L_B}, \tag{4.16}$$

$$\frac{L_f}{L_B} \equiv \frac{\pi}{2u_0^2 L_B}\int_0^\infty \frac{E\left(k\right)}{k}\mathrm{d}k = \frac{3}{4\sqrt{\pi}k_p}, \tag{4.17}$$

$$\frac{\lambda}{L_B} \equiv \frac{1}{L_B}\sqrt{\frac{15\nu u_0^2}{\epsilon}} = \frac{1}{2\pi k_p}\sqrt{\frac{10}{3}}, \tag{4.18}$$

$$\frac{\eta}{L_B} \equiv \frac{1}{L_B}\left(\frac{\nu^3}{\epsilon}\right)^{1/4} = \sqrt{\frac{1}{3\pi\sqrt{2}}\frac{1}{k_p}\frac{\nu}{u_0 L_B}}, \tag{4.19}$$

$$R_\lambda \equiv \frac{u_{rms}\lambda}{\nu} = \frac{1}{2\pi k_p}\sqrt{\frac{10}{3}}\frac{u_0 L_B}{\nu}, \tag{4.20}$$

where u_{rms} is the realized component r.m.s. fluctuation velocity, ν is the fluid kinematic viscosity, ϵ is the viscous dissipation rate, L_f is the longitudinal velocity correlation length, λ is the transverse Taylor microscale, η is the Kolmogorov length, and R_λ is the Taylor microscale Reynolds number. It is noted that the peak wavenumber k_p can be derived from the definitions of R_λ and η above

$$k_p = \left(\frac{L_B}{2\pi}\right)\left(\frac{20}{27R_\lambda^2\eta^4}\right)^{1/4}. \tag{4.21}$$

After the initialization of the velocity field, the populations $\mathbf{f}(\mathbf{x}, t)$ were then evolved iteratively to establish a consistent initial pressure field as described in Mei *et al.* (2006). The parameter settings are shown in Table 4.1. Here we set the same input parameters in our simulation as those in Burton and Eaton (2005), i.e., the same Taylor microscale Reynolds number R_λ and the ratio between the Kolmogorov length and particle diameter η/d. Note that due to the reduced size of our computational

Table 4.1: Parameter settings for flow field initialization in our LBM code and in the finite difference simulation of Burton and Eaton (2005). Here d is the particle diameter.

	grid	L_B	L_B/d	u_0	k_p/k_0	ν	R_λ	η/d
LBM	512^3	512	64	0.0205	2.34	0.0193	64.34	0.48
BE (2005)	192^3	192	192	0.447	7.03	0.122	65	0.5

domain ($L_B/d = 64 < 192$), the normalized peak wavenumber k_p/k_0 in our simulation is consequently decreased in order to maintain the same R_λ and η/d as in Burton and Eaton (2005). Nevertheless, the domain size L_B of our LBM simulation is verified to be larger than 4 times the integral length L_f, which is 92.16 in the lattice Boltzmann units at $t = 0$, implying it is sufficient to encompass the largest length scale of the turbulence at the specified Taylor microscale Reynolds number R_λ.

The total time duration of our LBM simulation is from $t = 0$ to $t = 0.79T_{e,0}$, corresponding to $10,000$ time steps, where the initial eddy turnover time is defined as $T_{e,0} \equiv u_{rms}^2/\epsilon$. The high-order statistics of real turbulence is realized by evolving the single-phase flow until the skewness of about -0.5 has been developed at $t = 0.16T_{e,0}$, as shown in Figure 4.7(a) below. At this point, a single fixed particle with diameter of about twice the Kolmogorov length scale of the unladen turbulence is inserted at the center of the domain. No-slip boundary condition on the particle surface is achieved by applying a second-order interpolated bounce-back scheme. For the fixed particle, the information of the populations $\mathbf{f}(\mathbf{x}, t)$ for the fluid nodes inside the particle is ignored. The flow field is over-resolved as shown by $k_{max}\eta > 10$ for the whole time interval.

Figure 4.6 displays zoom-in view of the vorticity contours on a center-cut plane of $z = 255.5$. Both the laden and unladen flows are shown at two time points of $0.47T_{e,0}$ ($6,000$ lattice time steps) and $0.79T_{e,0}$ (10,000 lattice time steps), respectively. The enhanced vorticity near the particle surface indicates the local increase of dissipation, which can be attributed to the effect of the no-slip boundary condition on the particle

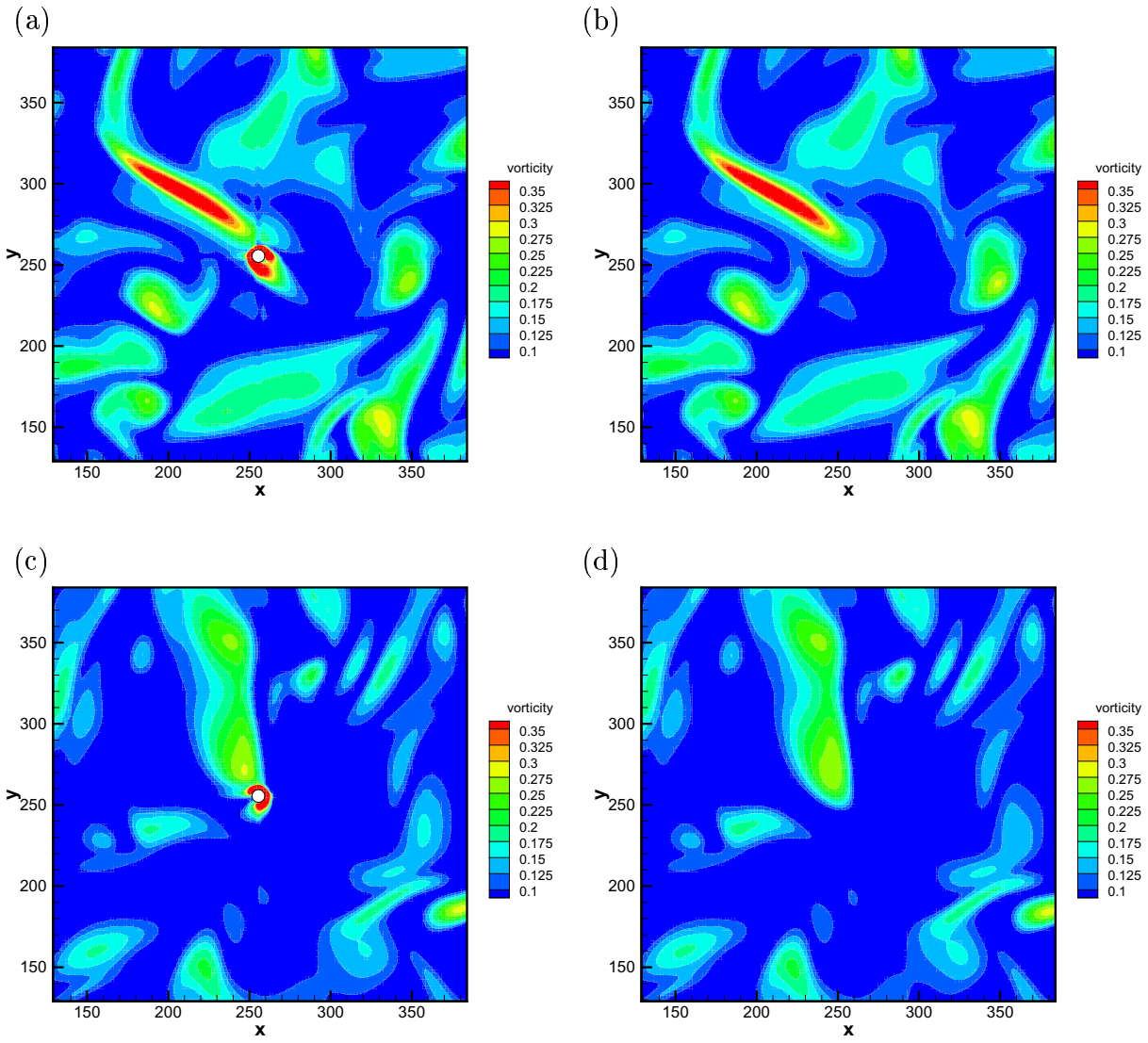

Figure 4.6: Zoom-in view of vorticity contour and particle location on a plane-cut of $z = 255.5$ in the 512^3 simulation: (a) $0.47T_{e,0}$ and (c) $0.79T_{e,0}$. Note that the presence of particles is associated with high vorticity values (represented by the colors towards the red end), indicating relatively large dissipation near particle surfaces. The corresponding vorticity contours for single-phase flow at the two times are shown in (b) and (d), respectively.

surface. At large radial distance from the particle surface, the particle-laden flow is almost identical with the unladen flow results.

Figure 4.7, 4.8, and 4.9 illustrate the impact of particle insertion on turbulence

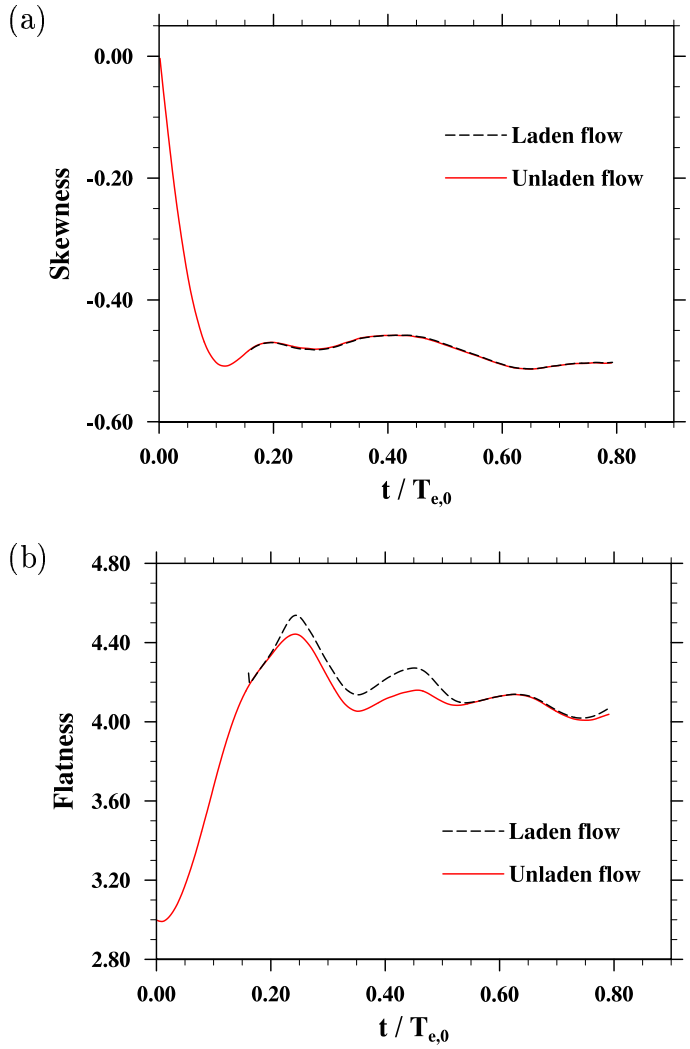

Figure 4.7: Time evolution of high-order statistics of turbulence for both particle-laden and unladen flow: (a) skewness, (b) flatness.

evolution using various statistics, including the velocity derivative skewness and flatness, Taylor microscale Reynolds number, and normalized turbulent dissipation rate. Due to the small volume fraction of 2.0×10^{-6}, the particle-laden flow is almost indistinguishable from the unladen flow, except for the flatness shown in Figure 4.7(b), where the two cases are distinct from the moment of particle insertion at $t = 0.16T_{e,0}$ to $t = 0.55T_{e,0}$, corresponding to $2,000 \sim 7,000$ lattice time units. It is of interest to compare this time duration with the flow adjustment time required to establish the boundary layer around the particle surface. The flow adjustment time can be roughly

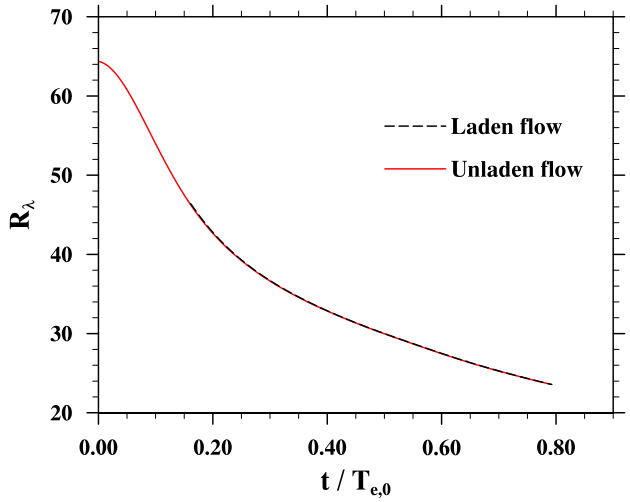

Figure 4.8: Time evolution of Taylor microscale Reynolds number for both particle-laden and unladen flow.

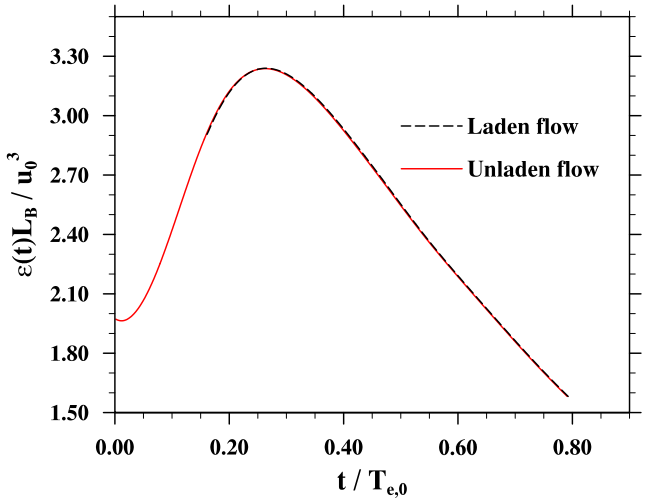

Figure 4.9: Time evolution of normalized dissipation rate for both particle-laden and unladen flow.

estimated as $T_{adjust} = \delta_{BL}^2/\nu$, where the boundary layer thickness $\delta_{BL} \sim a_p/\sqrt{Re_p}$, and ν is the fluid kinematic viscosity. In this case, the maximum particle Reynolds number Re_p is approximately 20 (Burton and Eaton, 2005). Then the period of flow adjustment is about $T_{adjust} \sim {a_p}^2/(Re_p\nu) = 4^2/(20 \times 0.0193) = 41.5$ lattice time units, which is much less than the aforementioned time duration of $5,000$ lattice time units. After this time duration, the flatness of the laden flow and unladen flow reconcile.

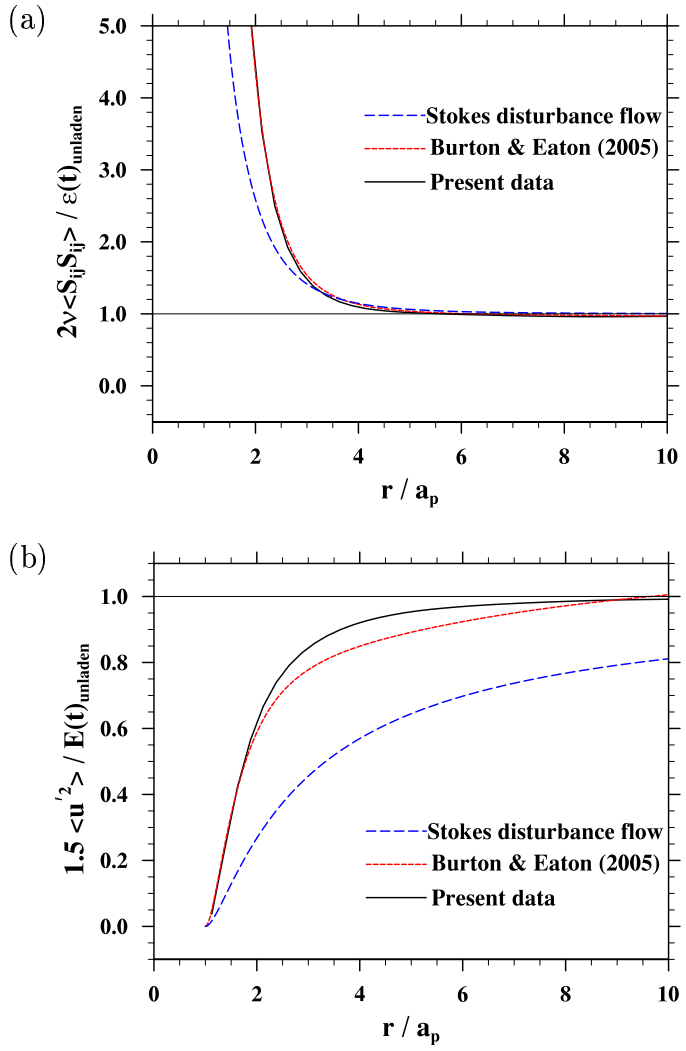

Figure 4.10: Comparison with the results of Burton and Eaton (2005) and Stokes disturbance flow. (a) normalized dissipation rate, and (b) normalized turbulent kinetic energy. The horizontal line marks the level of 1.0.

Figure 4.10 shows the radial profiles of turbulent kinetic energy and dissipation rate calculated by volume-average in spherical shells around the particle. The particle-laden flow results were first normalized by their unladen counterparts, and then averaged temporally to produce a mean profile. Specifically, in this study, we picked the normalized profiles at $7,000$, $8,000$, $9,000$, and $10,000$ lattice time units, which is far from the flow adjustment period described in Figure 4.7(b), and consequently allow us to avoid the transient effect introduced by the particle insertion. The

four time points also correspond to $t = 0.66T_{e,i}, 0.80T_{e,i}, 0.93T_{e,i}, 1.06T_{e,i}$, respectively, where $T_{e,i}$ is the eddy turnover time estimated at the moment when particle is inserted into the domain, and is $7,540$ lattice time units. The time-averaged profile was then compared with the results kindly provided by Prof. Burton and Prof. Eaton, where the data were processed in a similar procedure. Note that the temporal average performed for Burton and Eaton's data includes $t = 0.71T_{e,i}$ and $1.07T_{e,i}$ in their case, which cover approximately the same time duration as in our post-processing.

Considering the different configuration in our LBM simulation and the overset-grid finite difference simulation in Burton and Eaton (2005), it is interesting to observe that the results from the two fundamentally different methods reach quantitative agreement. Figure 4.10(a) shows almost identical profiles for normalized dissipation rate, where its value drops to within 20% of unit value prior to $r/a_p < 4$, and then flat out to unit value towards large radial distance. For turbulent kinetic energy profiles shown in Figure 4.10(b), the overlapped data within the range of $1.0 < r/a_p < 1.5$ depicts a substantial increase from zero to about 60% of unit value, followed by a gradual recovery towards full turbulent kinetic energy within the range of $1.5 < r/a_p < 9$, where the LBM results show marginally higher kinetic energy profile during the process. Overall, it is clear that the turbulence has been attenuated significantly near the particle surface.

Additionally, a zeroth-order analytic model based on Stokes disturbance flow (see Appendix D) is also presented in Figure 4.10 to be compared with the simulation results. The prediction from the model shows smaller kinetic energe and larger dissipation rate, which can be mainly ascribed to the effect of finite particle Reynolds number, such that the disturbance flow around the particle is no longer Stokes flow. In fact, the maximum value of particle Reynolds number in the simulation is approximately 20, as reported in Burton and Eaton (2005).

Table 4.2: Parameter settings in our LBM code and in the finite difference simulation of Lucci *et al.* (2010) for the single-phase decaying turbulence. Here L_B is the computational domain size, $k_0 = 2\pi/L_B$, and Δx is the grid spacing.

	grid	L_B	u_0	k_p/k_0	ν
LBM	256^3	256	0.020494	4	2.4094×10^{-3}
PS	256^3	2π	0.0503	4	1.4514×10^{-4}
Lucci *et al.* (2010)	256^3	1.0	0.0503	4	2.31×10^{-5}

	$dt \cdot u_0/\Delta x$	$\frac{U}{U_{Lucci}}$	$\frac{L}{L_{Lucci}}$	$\frac{T}{T_{Lucci}}$
LBM	0.02049	0.407437	256	628.32
PS	0.02049	1.0	6.2832	6.2832
Lucci *et al.* (2010)	0.02515	1.0	1.0	1.0

4.3.4 Decaying Turbulence Laden with Large Particle Loading

Prior to the simulation of particle-laden turbulence, the accuracy of our LBM code was verified by a comparison with a pseudo-spectral code for particle-free decaying homogeneous isotropic turbulence. The particle-free or single-phase flow will be referred to as the Case 1 flow. For most simulations, we consider a periodic domain of 256^3 grid points, indicating the potential range of wave number $1 \leq k \leq 128$. Following the work of Lucci *et al.* (2010), the initial velocity field at $t = 0$ was specified by a Gaussian field with a prescribed kinetic energy spectrum as

$$E(k) = \left(\frac{3u_0^2}{2}\right)\left(\frac{k}{k_p^2}\right)\exp\left(-\frac{k}{k_p}\right), \tag{4.22}$$

where k is the wave number, k_p is the wave number containing peak energy, and u_0 is the initial r.m.s. velocity. Both k and k_p have been normalized by the minimum wavenumber $k_0 \equiv 2\pi/L_B$, where L_B is the computational domain size.

Here we performed two simulations of the single-phase decaying flow, one using the LBM, and the second using the golden-standard pseudo-spectral method (Peng *et al.*, 2010). The settings of the simulation parameters are shown in Table 4.2. To separate the time scales of acoustic waves from hydrodynamics, we used a small velocity

scale in LBM, so the lattice time is much smaller than the hydrodynamic time scales. For example, the Kolmogorov time scale at the initial time is equal to 117 lattice time units. The relative velocity, length, and time scale ratios are listed Table 4.2 which can be used to convert flow statistics from one to the another. Note also that the effective time step sizes used in the different approaches are very similar.

It can be shown theoretically that this initial energy spectrum implies the following initial flow statistics:

$$\frac{3}{2}u_{rms}^2 \equiv \int_0^\infty E\left(k\right)\mathrm{d}k = \frac{3}{2}u_0^2 \quad \text{or} \quad \frac{u_{rms}}{u_0} = 1.0, \tag{4.23}$$

$$\frac{\epsilon L_B}{u_0^3} \equiv \frac{2\nu L_B}{u_0^3}\int_0^\infty k^2 E\left(k\right)\mathrm{d}k = 72\pi^2 k_p^2 \frac{\nu}{u_0 L_B}, \tag{4.24}$$

$$\frac{L_f}{L_B} \equiv \frac{\pi}{2u_0^2 L_B}\int_0^\infty \frac{E\left(k\right)}{k}\mathrm{d}k = \frac{3}{8k_p}, \tag{4.25}$$

$$\frac{\lambda}{L_B} \equiv \frac{1}{L_B}\sqrt{\frac{15\nu u_0^2}{\epsilon}} = \frac{1}{2\pi k_p}\sqrt{\frac{5}{6}}, \tag{4.26}$$

$$\frac{\eta}{L_B} \equiv \frac{1}{L_B}\left(\frac{\nu^3}{\epsilon}\right)^{1/4} = \sqrt{\frac{15\nu u_0^2}{\epsilon}} = \sqrt{\frac{1}{6\pi\sqrt{2}}\frac{1}{k_p}\frac{\nu}{u_0 L_B}}, \tag{4.27}$$

$$R_\lambda \equiv \frac{u_{rms}\lambda}{\nu} = \frac{1}{2\pi k_p}\sqrt{\frac{5}{6}}\frac{u_0 L_B}{\nu}, \tag{4.28}$$

where u_{rms} is the realized component r.m.s. fluctuation velocity, ν is the fluid kinematic viscosity, ϵ is the viscous dissipation rate, L_f is the longitudinal velocity correlation length, λ is the transverse Taylor microscale, η is the Kolmogorov length, and R_λ is the Taylor microscale Reynolds number. It is noted that the peak wavenumber k_p plays an important role in determining the initial flow dissipation rate, all flow length scales, and the flow Reynolds number.

In Table 4.3, we compare non-dimensional flow statistics for the Case 1 simulation, namely, the single-phase decaying turbulence. At $t = 0$, the above theoretical

Table 4.3: Comparison of simulated flow statistics for single phase turbulence. LBM and SP denote our LBM simulation and our pseudo-spectral simulation. The simulation by Lucci *et al.* (2010) is a second-order finite-difference simulation.

	u_{rms}/u_0	$\epsilon L_B/u_0^3$	L_f/L_B	λ/L_B	η/L_B	R_λ	R_{L_f}	R_{L_B}
$t/T_{Lucci} = 0$								
Theoretical	1.00	5.22	0.0938	0.0363	0.00208	79.1	204	2177.5
LBM	0.997	5.27	0.0830	0.0361	0.00207	78.3	180	2169
PS	0.997	5.28	0.0829	0.0360	0.00207	78.3	180	2171
Lucci *et al.* (2010)	1.00	5.81	0.0684	0.0345	0.00202	75	149	2177
$t/T_{Lucci} = 1$								
LBM	0.886	6.919	0.0858	0.0280	0.00193	53.9	165	1926
PS	0.884	6.963	0.0860	0.0278	0.00193	53.5	165	1924
Lucci *et al.* (2010)	0.847	7.70	0.0685	0.0259	0.00188	49	129	1888
$t/T_{Lucci} = 5$								
LBM	0.506	1.688	0.108	0.0323	0.00275	35.6	119	1104
PS	0.503	1.668	0.115	0.0323	0.00276	35.4	126	1096
Lucci *et al.* (2010)	0.463	1.57	0.0891	0.0305	0.00280	31	89.8	1078

predictions are also listed. In the pseudo-spectral (PS) simulation, the energy spectrum is truncated at $k = N/3$. For the initial spectrum given by Eq. (4.22), it an be shown theoretically that this truncation has no noticeable effect on the kinetic energy and dissipation rate. The relative differences between the pseudo-spectral results and the theoretical values are typically about 1% or less, except in L_f where it is 11.6%. These minor differences are due to the discretization effect in the wave vector space. Since the integral length L_f is mostly determined by the large scale, the mode discretization has a significant effect. In our LBM, an identical initial flow as in the pseudo-spectral simulation was used. The initial populations $\mathbf{f}(\mathbf{x}, t)$ were iterated following the procedure described in Mei *et al.* (2006) to achieve a consistent initial pressure field; this amounts to solving a pressure Poisson equation iteratively. It is clear that all flow statistics from the LBM simulation are in excellent agreement with those from the PS simulation. Almost identical kinetic energy and dissipation rate spectra between the

Table 4.4: Parameters for particle-laden flow simulations at the release time.

Case	N^3	d	ρ_p/ρ_f	N_p	d/η	d/λ	ϕ_v	ϕ_m	τ_p/τ_k
2	256^3	8.0	2.56	6,400	16.1	1.1	0.10	0.23	36.8
3	256^3	8.0	5.0	6,400	16.1	1.1	0.10	0.36	71.9
3H	512^3	16.0	5.0	6,400	16.1	1.1	0.10	0.36	71.9
4	256^3	11.0	2.56	2,304	22.1	1.5	0.10	0.21	69.6
5	512^3	8.0	5.0	51,200	8.08	0.559	0.10	0.36	18.1

LBM and SP simulations were also observed (not shown here). These provide a direct validation of our LBM simulation and are consistent with the results shown in Peng *et al.* (2010).

The flow statistics obtained by Lucci *et al.* (2010), also shown in Table 4.3, however, have some inconsistencies even at the initial time. For example, the dissipation rate is larger than the theoretical value by about 11.3% and the Taylor microscale is less by 5% when compared to the theoretical value. Part of these inconsistencies could be a result of different random numbers used in the flow initialization. Since our simulated flow statistics are much closer to the theoretical values at $t = 0$, we suspect there are some other problems in Lucci *et al.* (2010), either in their low-order finite-difference scheme or in their processing of flow statistics. Overall, the data in Table 4.3 imply that the numerical method used in Lucci *et al.* (2010) has a noticeable numerical dissipation at earlier times, while our LBM simulation has negligible numerical dissipation. We shall return to this point again when we compare time evolutions of turbulence kinetic energy and dissipation rate.

For the particle-laden turbulence simulations, the single-phase flow field was evolved for sometime until a converged velocity-derivative skewness of about -0.50 was developed. At this moment, particles were released in the domain at random locations with a gap distance of at least two grid spacing in between. Initial translational velocities of particles are set as the instantaneous fluid velocity at the particle center,

and angular velocity is set to zero. A set of five simulations, listed in Table 4.4, were preformed to study the turbulence modulation by finite-size particles. Cases 2, 3, and 4 roughly match Cases D, E, and G in Lucci *et al.* (2010). The gravity was set to zero. The simulations are run from $t = 0$ to $t = 2.12T_{e,0}$, corresponding to $5,000$ time steps, where the initial eddy turnover time $T_{e,0} \equiv u_{rms}^2/\epsilon$ and it is $2,356$ lattice time units. The flow fields are well resolved as shown by $k_{max}\eta > 1$ for the whole time interval. All the simulations were performed on an IBM Power6 supercomputer at NCAR with MPI parallelization using 32 processors (at 256^3) to 128 processors (at 512^3). Each simulation takes 6 to $27h$ of wall-clock time.

Figure 4.11 displays the vorticity contour for Case 4 on the boundaries of the computational domain at $3,000$ lattice time step ($1.27T_{e,0}$) and $5,000$ lattice time step ($2.12T_{e,0}$), respectively. A layer of fluid to the top is removed to show the locations of a portion of the $2,304$ particles. The magnitude of vorticity decreases with time as expected, as can be seen from the color difference of Figure 4.11(a) and (b).

In Figure 4.12 we provide 2D visualizations of the vorticity magnitude on a slice and locations of the particles cutting through the same slice, for two different times. These are results from the Case 3 run at $z = 128.5$ (a $x - y$ slice near the center of the domain). It is observed that the presence of particles is often associated with high voritcity values (the red spots), suggesting that motion of finite size particles can generate small-scale flow structures near its surface. Note that Case 3 has the largest density ratio and likely the largest slip velocity. We found that the enhanced activities at small scales due to particles are self evident when compared to the particle-free case as shown in Figure 4.12(b) and Figure 4.12(d). The vortical structures are larger in size and more interconnected in the single-phase flow case. There is very little correlation between the single-phase and two-phase vorticity fields at a given time. At the earlier time $t = 0.522T_{e,0}$, both the particles and the fluid have large kinetic energy and as such there is a large slip velocity between a particle and its neighboring flow, the disturbance near the particle surface is more visible. At later times, the system has less and less kinetic energy and interphase slip velocity, the disturbance flow near the particles are

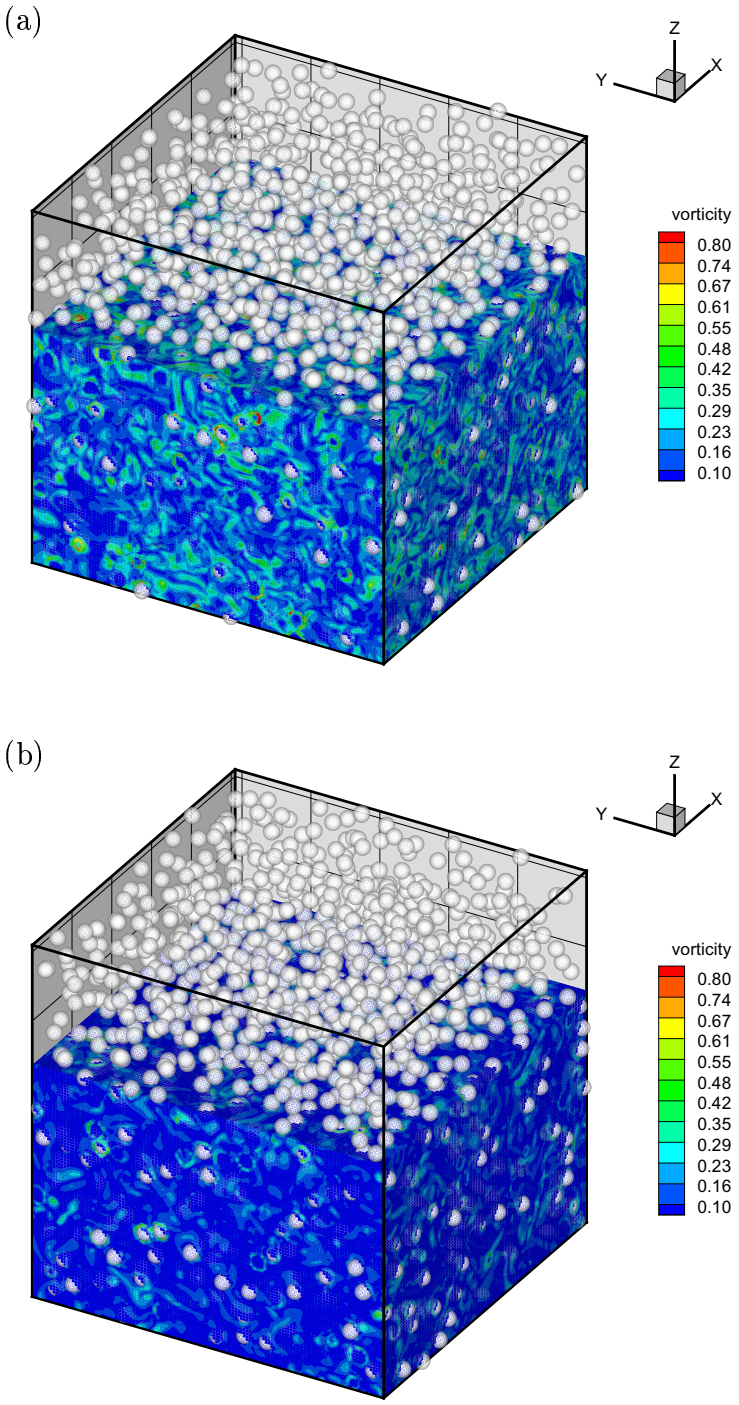

Figure 4.11: Vorticity contour at (a) $1.27T_{e,0}$ and (b) at $2.12T_{e,0}$ for case 4. A layer of fluid is removed to show some of the 2304 particles.

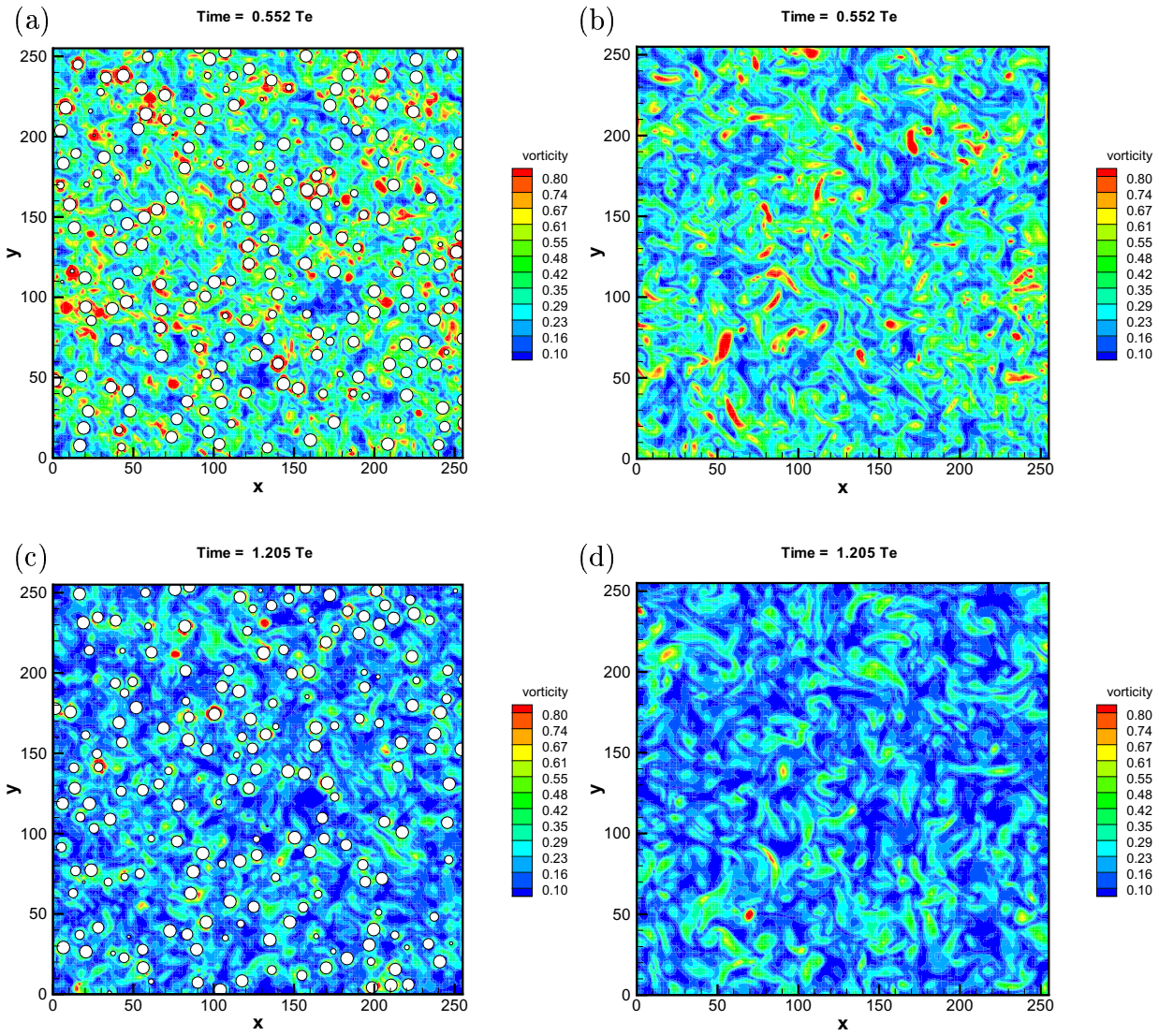

Figure 4.12: Snapshots of vorticity contour and particle location on a plane-cut of $z = 128.5$ in 256^3 simulation of case 3: (a) $0.55T_{e,0}$ and (c) $1.21T_{e,0}$. Note that the presence of particles is often associated with high vorticity values (represented by the colors towards the red end), indicating relatively larger dissipation near particle surfaces. The corresponding vorticity contours for single-phase flow at the two times are shown in (b) and (d), respectively.

weaker. The effect of particles on the viscous dissipation thus changes with time, as will be shown in Figure 4.14 below.

Figure 4.13(a) shows the temporal evolution of turbulent kinetic energy (TKE)

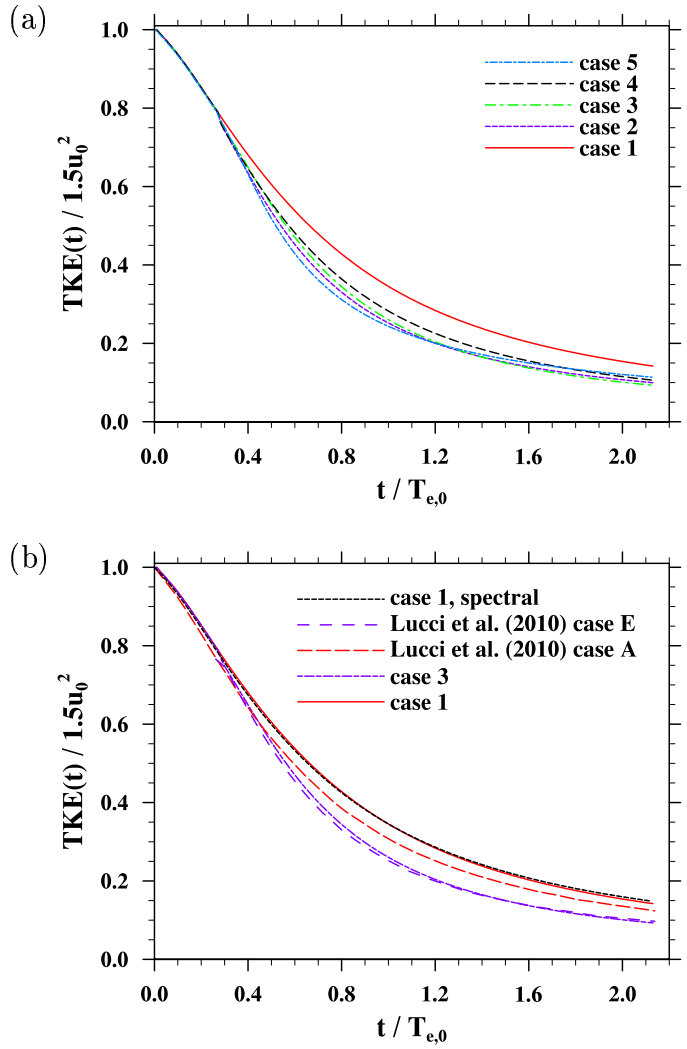

Figure 4.13: Temporal evolution of turbulent kinetic energy normalized by its initial value. (a) Different cases simulated here; (b) Comparison with the results of Lucci *et al.* (2010) and PS (for single-phase turbulence only).

normalized by $1.5u_0^2$ computed at time $t = 0$ for all the five cases. It should be noted that the kinetic energy $TKE^{full}(t)$ we computed is the kinetic energy for the full field, including the space occupied by the particles where a rigid body translation and rotation together define the local velocity. The average kinetic energy of the fluid domain, $TKE^{fluid}(t)$, is related to $TKE^{full}(t)$ as

$$TKE^{full}(t) = TKE^{fluid}(t)(1-\phi_v) + \phi_v\left(\frac{1}{2}\langle V_p^2\rangle + \frac{1}{20}d^2\langle\Omega_p^2\rangle\right) \tag{4.29}$$

Compared with the particle-free turbulence, the TKE decreases faster in the particle-laden cases from the moment of particle release till about $1.6T_{e,0}$, and then the decaying rate tends to be the same in all cases. In addition, the increase of particle number results in an evident reduction of TKE, as shown by comparing the curves from Case 2 and Case 4. This may be associated with more surface areas in Case 2 than in Case 4. The increase of particle density has a marginal effect on decaying rate reduction, based on a comparison of Case 2 with Case 3.

In Figure 4.13(b), we compare our results with the results of Lucci *et al.* and PS (for single-phase turbulence only). Note that Case 1 and Case 3 of our LBM simulations correspond to the parameter setting of Case A and Case E in Lucci *et al.* (2010). Our LBM and PS results for the single-phase flow overlap, but the curve from Lucci *et al.* (2010) for the single phase flow shows a faster decay of kinetic energy due to their larger viscous dissipation at the early times, as has already been noted in Table 4.3 (also see in Figure 4.14(b) below). The larger viscous dissipation for the single phase flow simulation in Lucci *et al.* (2010) could be partially due to the numerical dissipation in the second-order finite-difference scheme that Lucci *et al.* used. Our result for Case 3 is closer to the result of Case E in Lucci *et al.* (2010). It should be noted that our data represent $TKE^{full}(t)$ while the result of Lucci *et al.* is for $TKE^{fluid}(t)$, so the comparison is not a very direct comparison. The good comparison is somewhat surprising as the results for even the single-phase flow case do not match. It may be possible that the regularized three-point delta function used in the immersed boundary implementation in Lucci *et al.* (2010) is a local filter that somewhat smooths out large velocity gradient at the particle-fluid boundaries, reducing slightly the local dissipation rate near the particle surface. The numerical dissipation in a low order finite-difference scheme and the regularization filtering may happen to cancel one another, giving results comparable to what observed in our LBM scheme. For these reasons, we believe that our results for both the single-phase and the particle-laden flow are likely to be more accurate than those of Lucci *et al.* (2010).

Figure 4.14(a) shows the modification of turbulent dissipation rate due to the

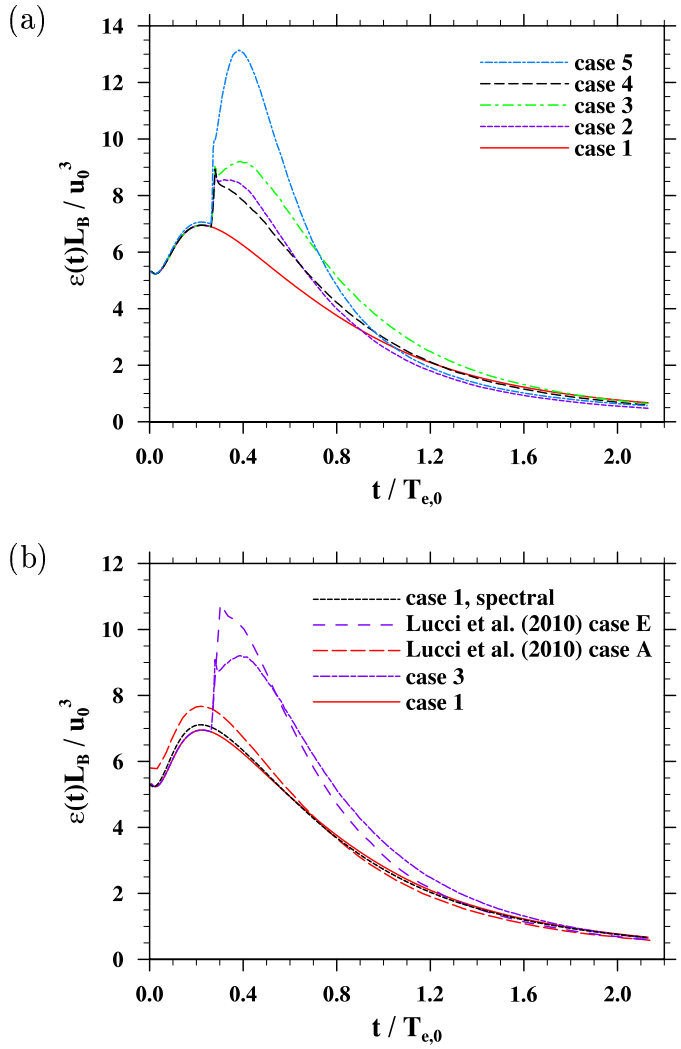

Figure 4.14: Temporal evolution of turbulent dissipation rate normalized by its initial value. (a) Different cases simulated here; (b) Comparison with the results of Lucci *et al.* (2010) and PS (for single-phase turbulence only).

presence of particles. The local dissipation inside the particles is zero, so the whole field dissipation and the fluid-region averaged dissipation are related by

$$\epsilon^{full}(t) = (1 - \phi_v)\,\epsilon^{fluid}(t)\,. \tag{4.30}$$

We computed $\epsilon^{full}(t)$ directly and then divided by $(1-\phi_v)$ to obtain $\epsilon^{fluid}(t)$ which is what shown in Figure 4.14. At the moment of about $0.26T_{e,0}$, the injection of particles into the fluid domain causes a sudden jump of the dissipation rate, followed by a peak value at about $0.4T_{e,0}$, and then the total dissipation decreases monotonically.

The total particle surface area normalized by the domain size squared is equal to $6\phi_v L/d$, implying that Case 5 has the largest effective surface areas and Case 4 has the smallest effective surface. This explains why the peak dissipation of the system after the introduction of solid particles is the largest for Case 5, and the smallest for Case 4. The two intermediate cases, Case 2 and Case 3, have the same effective surface area, but different Stokes numbers. The larger the Stokes number (Case 3 compared to Case 2), the higher the peak dissipation value due to a larger slip velocity. Another observation is that, after the peak is reached, the system dissipation rate decays faster if the particle Stokes number is smaller, indicating a faster approach to an interphase quasi-equilibrium stage of the system evolution (the later part of the time evolution shown in Figure 4.13(a) and Figure 4.14(a)).

Figure 4.14(b) compared our LBM results of the average flow dissipation rate to SP single-phase simulation and to the results of Lucci *et al.* (2010), in a manner similar to Figure 4.13(b). Again for the single-phase flow simulation, our LBM result matches the SP result, but Lucci *et al.* over-predicted the flow dissipation at earlier times. The two particle-laden cases are in general agreement in that both have a higher flow dissipation rate when compared to the single-phase turbulence for most of the time after particle release. An important difference between our result for Case 3 and the result of Lucci *et al.* for Case E is that, immediately after the particle injection, the jump in the dissipation rate in Lucci *et al.* is much larger than in our result. As the viscous boundary layers develop on the particle surface, the LBM result shows a gradual increase in flow dissipation before reaching a second peak while the Lucci *et al.* shows a monotonic decay. At the moment of particle injection, there is an unphysical jump or mismatch of fluid velocity and particle surface condition. The LBM scheme is a weakly compressible formulation while Lucci *et al.*'s is an incompressible flow solver. The regularization function in the Lucci *et al.*'s immerse boundary treatment would also have a strong impact at the moment of injection. At this moment, it is not completely clear which method better handles the flow physics immediately after the unphysical jump condition. Nevertheless, the time evolutions after the transition stage

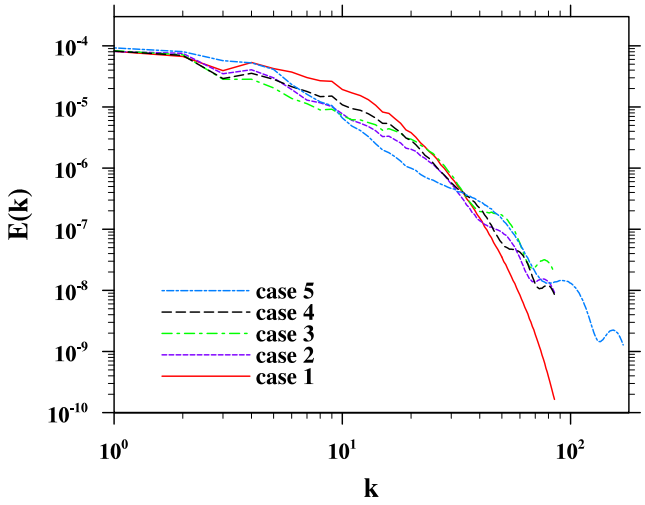

Figure 4.15: Kinetic energy spectrum at the end of simulation ($2.12T_{e,0}$).

($t/T_{e,0} > 0.6$) are very similar.

An important characteristic of the particle-laden turbulent flow is the addition of motion at the scale of particle size, at the cost of reduction of large-scale fluid motion, since no energy is added to the system here. This is clearly shown in Figure 4.15 where we compare the kinetic energy spectra at the end of simulations $t = 2.12T_{e,0}$. It should be noted that we use the full velocity field including the rigid-body velocity inside the particles to compute the energy spectrum. Typically, the kinetic energy is higher at higher wavenumbers when compared to the single phase flow. At intermediate and low wavenumbers, this is reversed. Interestingly, wave-like oscillations are observed at the tails of the spectra for turbulent particle-laden flow, as shown previously in Ten Cate *et al.* (2004) and Lucci *et al.* (2010), due to the discontinuity of flow velocity gradient at the finite-size particle surface. Compared to the results of Case 2 and Case 4, Case 3 possesses noticeably larger TKE at large wavenumbers due to large mass loading and large Stokes number.

The result for Case 5 is more complicated. First, the cross-over at large wavenumbers becomes very evident with a clear attenuation of energy at the intermediate wavenumbers. Second there is apparently a second cross-over at $k = 4 \sim 5$. It could

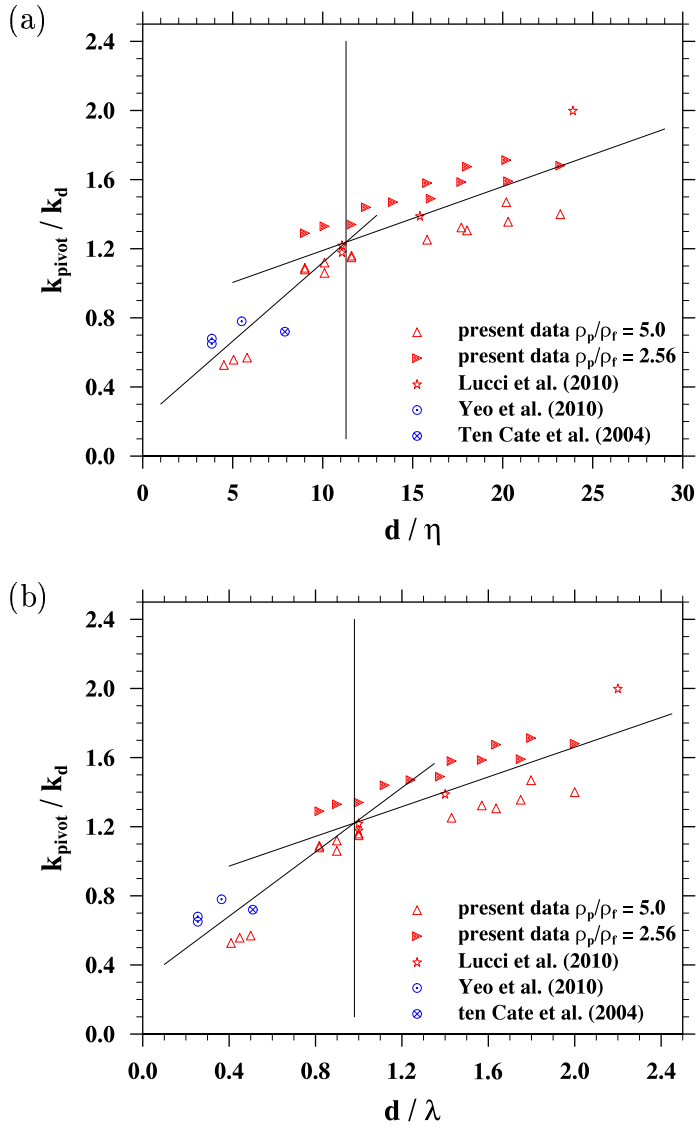

Figure 4.16: Normalized pivoting wavenumber as a function of particle size scaled by (a) Kolmogorov length scale, and by (b) Taylor microscale. The slopes are 0.091 and 0.037 in (a) and 0.93 and 0.43 in (b). The vertical lines are at 11.3 and 0.98 in (a) and (b), respectively.

be due to some large-scale structures formed by the particles. This will need to be studied in the future.

It is now well known that the cross-over wavenumber or pivot wavenumber, k_{pivot} , at the large-wave number end scales with the particle diameter. We introduce $k_d \equiv L_{box}/d$, where L_{box} is the computational domain size. Figure 4.16 shows

the dimensionless pivot wavenumber k_{pivot}/k_d as a function of nondimensional particle diameter. In Figure 4.16(a), the diameter is normalized by the Kolmogorov scale of the single-phase flow, and in Figure 4.16(b) by the transverse Taylor microscale of the single phase flow. Each data point represents the result at a given time during the decay. Additional simulations than those mentioned in Table 4.4 are performed to cover different d ranges. All results available in the studies shown in Table 1.1 are also shown. Our results are in general agreement with one another, although the simulations in Ten Cate *et al.* (2004) and Yeo *et al.* (2010) are obtained for forced particle-laden turbulent flows. Despite some scattering of the data points partially due to some uncertainty in reading the pivot wavenumbers, two important observations can be made. First, the dimensionless wavenumber increases with the dimensionless particle size. This is due to the different natures of the local flow: a particle of diameter of the order of Kolmogorov scale senses a more uniform local velocity gradient, while a particle much larger than the Kolmogorov scale experiences a more complex local flow field including inertia-subrange fluctuations. Another observation is that there appears to be two slopes in each of the plot, the dimensionless pivot wavenumber is more sensitive to particle size when $d/\eta < 11$ or $d/\lambda < 1$, and becomes less sensitive for large particle sizes. The transition takes place apparently at $d \sim \lambda$, as λ represents the scale of velocity gradient in the undisturbed turbulent flow. Finally, the magnitude of k_{pivot}/k_d depends on the particle-to-fluid density ratio at a given volume fraction, with denser particles leading to a smaller k_{pivot}/k_d.

We shall now examine the effect of the no-slip particle-fluid interface at the particle scale by gathering statistics as a function of distance from the surface of each particle. Figure 4.17 shows the profile of bin-averaged $< S_{ij}S_{ij} >$ computed at different times for case 3 and case 3H, respectively. The calculation of strain rate S_{ij} by LBM is described in detail in Yu *et al.* (2006) and Appendix C. The distance r from a fluid lattice node to the center of the nearest particle is normalized by particle radius a_p, and then divided into bins of given width of $\delta_{bin} = 0.05a_p$. The averaged particle

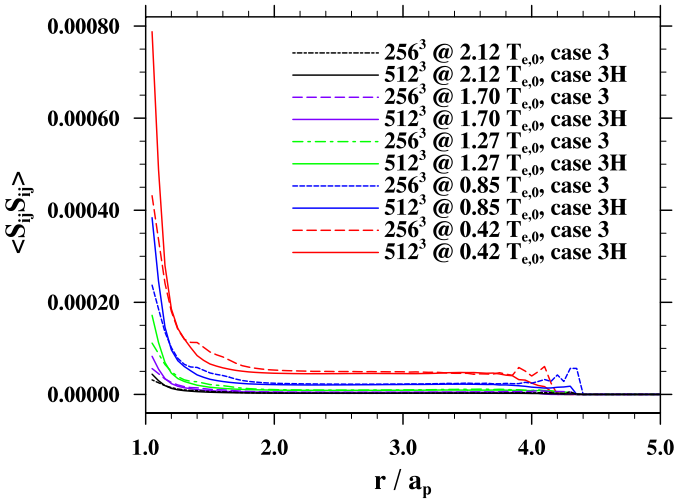

Figure 4.17: Profile of bin-averaged $< S_{ij}S_{ij} >$ as a function of distance from the particle center showing dependence on lattice resolution.

center-to-center distance l_p can be estimated as

$$\frac{l_p}{a_p} = \left(\frac{4\pi}{3\phi_v}\right)^{1/3} \approx 3.47, \tag{4.31}$$

which implies that the statistics would be subjected to significant uncertainties due to insufficient number of fluid lattice nodes at distance larger than $3.47a_p$. Indeed, this is justified by the observation that the value of $< S_{ij}S_{ij} >$ starts to fluctuate from about $3.8a_p$, and becomes almost negligible when $r/a_p > 4.4$, as shown in Figure 4.17.

It is clear that for a single time, the $< S_{ij}S_{ij} >$ value dramatically decreases from the surface of a particle to a distance of about $1.5a_p$, and then retains the low value. This indicates the substantial impact of the solid particles to their surroundings within this range. For both case 3 and case 3H, the magnitude of $< S_{ij}S_{ij} >$ reduces as time evolves, which is expected for decaying turbulent flow simulations. We also noted that the higher resolution (case 3H) yields smoother profiles, e.g., the fluctuations in case 3 within the range of $1.3a_p \sim 1.8a_p$ is avoided in case 3H, due to larger number of fluid nodes available in the latter case. For this reason, we will focus on the results from case 3H for the following discussions.

Figure 4.18(a) shows the profile of normalized bin-averaged dissipation rate at different times for case3H. The normalization is performed by scaling the dissipation

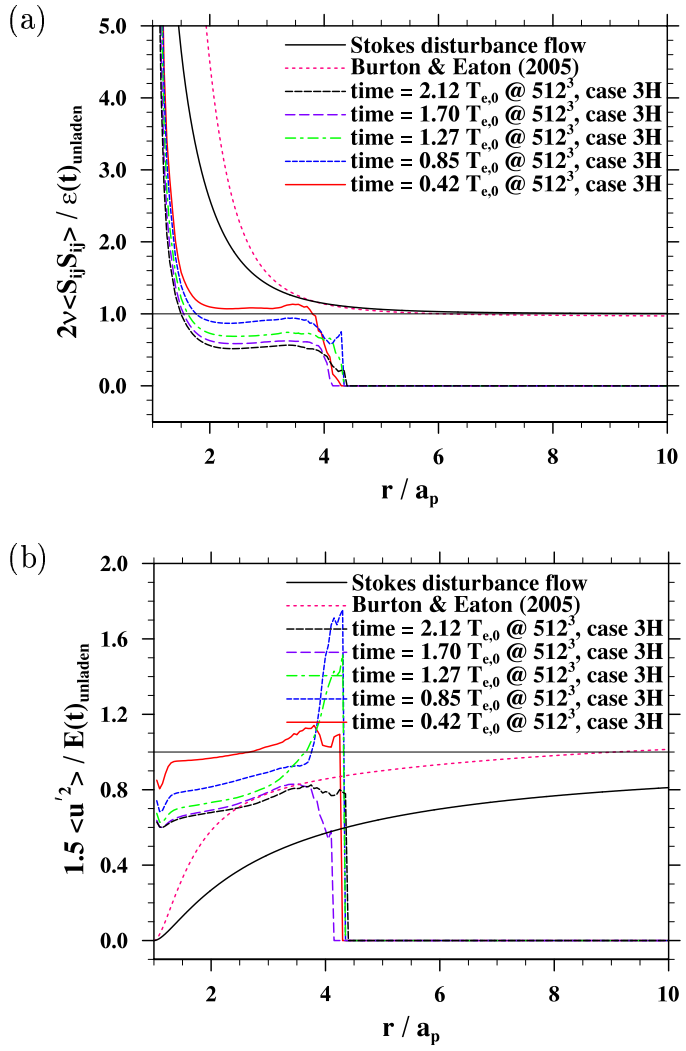

Figure 4.18: Comparison with the results of Burton and Eaton (2005) and Stokes disturbance flow. (a) normalized dissipation rate, and (b) normalized turbulent kinetic energy. The horizontal line marks the level of 1.0.

rate of the particle-laden turbulence with its particle-free counterpart simulated with the same initial condition and lattice resolution. The trends are similar to those found in Figure 4.17: the normalized dissipation rate drops substantially within a short distance ($\sim 1.5a_p$) from the particle surface, and decreases with time for decaying turbulence.

Moreover, the results are compared with the averaged data from Figure 17 of Burton and Eaton (2005) as kindly provided for us by Prof. T.M. Burton and Prof.

J.K. Eaton, as well as results from a zeroth-order analytic model developed based on Stokes disturbance flow (see Appendix D). The analytic model underestimates the dissipation rate prior to a distance of $\sim 3.5a_p$ compared with Burton and Eaton's data, and then their results become almost identical at larger distance. This can be mainly attributed to the fact that the particle Reynolds number is up to 20 in Burton and Eaton's simulation, which no longer justifies the Stokes flow assumption of the model. It is also clear that the dissipation rate in case 3H are lower than that of Burton and Eaton (2005). The difference could be due to the much larger particle size in case 3H, where $d = 16.1\eta$ belonging to the inertial range, while in Burton and Eaton (2005) the particle size is $d = 2\eta$ in the dissipative range, which could enhance the dissipation.

Figure 4.18(b) shows the profile of bin-averaged turbulent kinetic energy as a function of distance from the center of a solid particle. Again, the results are normalized by those from unladen turbulence, and are compared with the averaged data from Figure 16 of Burton and Eaton (2005), as well as with the data from an analytic model based on Stokes disturbance flow (see Appendix D). The turbulent kinetic energy first declines to a lower value till the distance reaches about $1.1a_p$, followed by a jump to a high value at about $1.3a_p$, and then reaches a plateau with slight increase till $\sim 3.5a_p$, after which the results are severely distorted due to the lack of sufficient number of fluid lattice nodes. As time evolves, the normalized kinetic energy decreases, which is consistent with the decrease of dissipation rate as seen in Figure 4.18(a). In addition, the kinetic energy profiles are in general higher than that from Burton and Eaton (2005) within the comparable distance range of $\sim 3.5a_p$, due to the difference in particle sizes as mentioned above. The analytic model, however, yields markedly smaller values than Burton and Eaton's simulation within the whole range, mainly because of the inconsistency between the finite particle Reynolds number in the simulation and the Stokes disturbance flow assumption in the model.

It is also of interest to probe the appropriate way to normalize the profiles near the particle surface. Figure 4.19(a) shows the profiles of dissipation rate at different times scaled by the corresponding values computed from the particle-free turbulence.

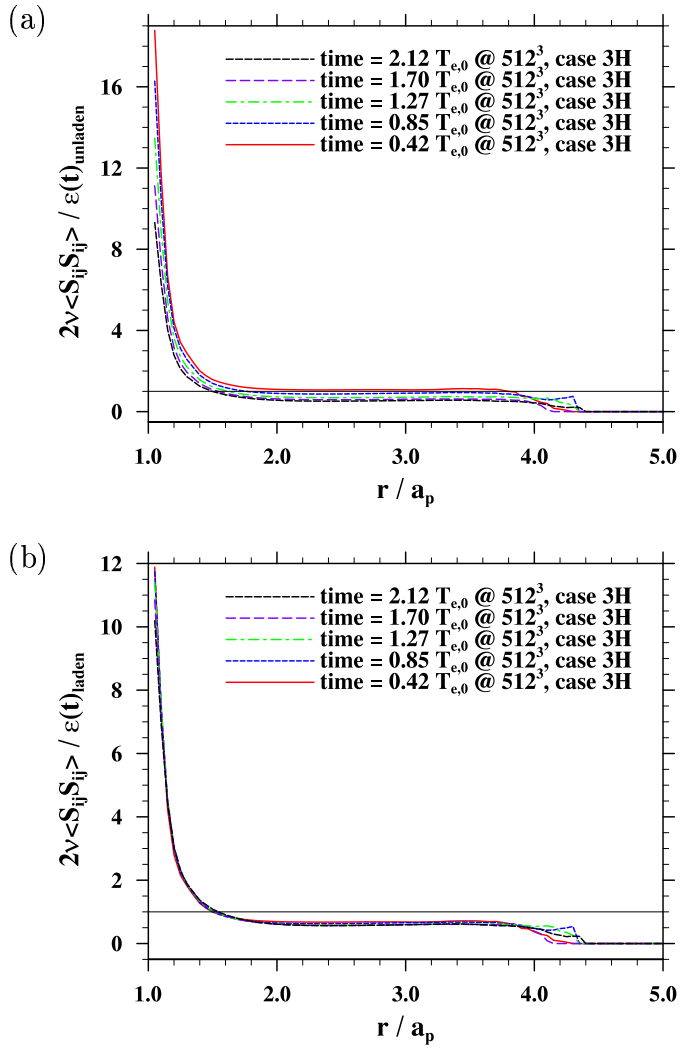

Figure 4.19: Profile of bin-averaged dissipation rate as a function of distance from the center of a particle: (a) normalized by the values from unladen turbulence, and (b) normalized by the values computed on the whole domain including both particle phase and fluid phase.

As a comparison, Figure 4.19(b) demonstrates the scaling by using the transient values of the whole domain from the particle-laden turbulence, including both solid and fluid region. Clearly, the data reconcile better in the latter case. Similar trend is shown in Figure 4.20: the normalization using values from particle-laden turbulence yields more consistent results.

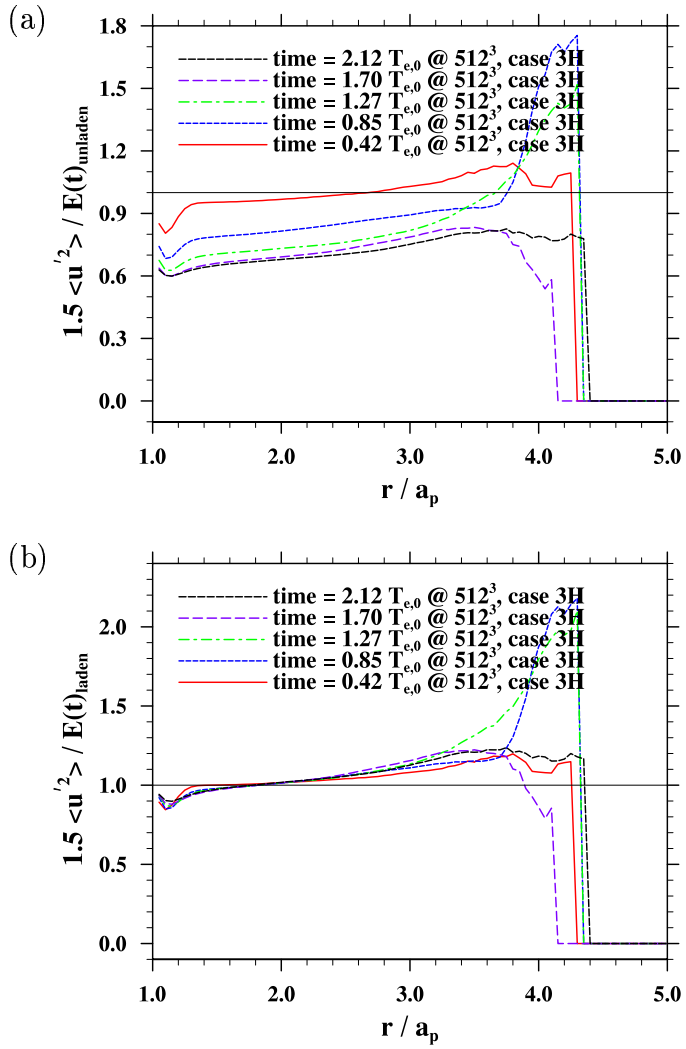

Figure 4.20: Profile of bin-averaged turbulent kinetic energyas a function of distance from the center of a particle: (a) normalized by the values from unladen turbulence, and (b) normalized by the values computed on the whole domain including both particle phase and fluid phase.

4.3.5 Timing and Scalability

Finally, we comment on the wall-clock times of the simulations, as shown in Table 4.5. All 256^3 runs in Table 4.5 used 32 processes and 512^3 runs used 128 processes. First, we note that the single phase flow simulation at 512^3 with 128 processes takes about twice the wall-clock time as the flow simulation at 256^3 with 32 processes, as expected from simple scaling of the problem size. A remarkable feature is that the particle-resolved simulations only take a moderate overhead in terms of wall-clock time,

Table 4.5: The wall-clock time per time step for various runs.

Case	N^3	d	N_p	ϕ_v	Wall-clock per time step (s)	Additional overhead (%)
1 (flow only)	256^3	–	–	–	3.11	–
2	256^3	8.0	6,400	0.1023	3.84	23
3	256^3	8.0	6,400	0.1023	3.85	24
4	256^3	11.0	2,304	0.0957	3.74	20
1 (flow only)	512^3	–	–	–	7.01	–
3H	512^3	16.0	6,400	0.1023	8.84	26
5	512^3	8.0	51,200	0.1023	10.1	44

when compared to the single-phase flow simulation at the same resolution. This moderate overhead is a result of the LBM algorithm and our careful MPI implementation.

Furthermore, the overhead reported in Table 4.5 depends on the number of solid particles as well as the solid particle size. We could roughly partition the overhead into three parts: (1) the overhead associated with exchanging two layers of fluid-particle distribution data when compared with just one layer in single-phase flow simulation, and additional one layer slab-to-slab communication associated with the refilling procedure; (2) the overhead for processing the boundary links on the solid particle surface which is proportional to the total solid particle surface area ($\sim N_p d^2$); and (3) the overhead associated with updating the translational and angular locations and velocities of solid particles and with MPI_ALLREDUCE operations to collect single particle information and to store in corresponding solid particle arrays. Assume the overhead associated with the third part is relatively insignificant; we can use the results in Table 4.5 to estimate the overheads for the first part and the second part. Note that the overhead for the first part is independent of the number of solid particles, and the overhead for the second part is proportional to $N_p d^2$. For example, by comparing Cases 2, 3, and 4, we infer that the overhead for the first part is roughly 12.5% for 256^3 simulation. The

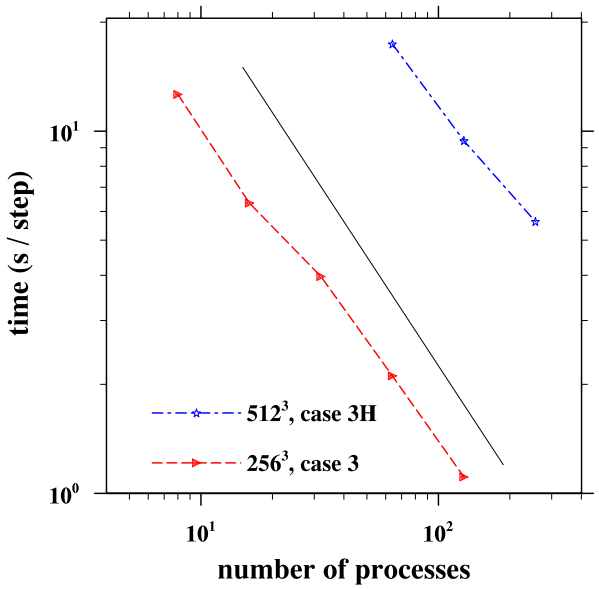

Figure 4.21: Scalability: CPU time vs the number of processes for case 3 and case 3H.

overhead for the second part for Case 2 and Case 3 is roughly 11% and for Case 4 it is roughly 7.5%. Likewise, a comparison of Case 3H and Case 5 shows the overhead for the first part is 8% for 512^3 simulations, the overhead for the second part for Case 3H and Case 5 are 18% and 36%, respectively.

We also document the scalability of the code against the number of processes used, in Figure 4.21. Case 3 and Case 3H are used and the wall-clock times per time step are shown in the figure. The black line shows the ideal scalability curve of slope -1. Clearly the code running time scales well with n_{proc} .

To summarize, in this chapter, we have presented a particle-resolved simulation method based on the multiple-relaxation-time lattice Boltzmann equation. The no-slip boundary condition on the moving particle surface is realized by a second-order interpolated bounce-back scheme. The mesoscopic particle distribution functions on a newly converted fluid node were built by an equilibrium distribution plus a non-equilibrium correction. A short-range repulsive force model was used to prevent particles from overlap. The code was implemented under the MPI framework with 1D domain decomposition, which has been proved to be efficient with an almost ideal scalability.

The code was first validated with sedimentation of a single particle and a multi-particle random suspension. It was then verified with the turbulence modulation data provided by Burton and Eaton(2005), where a single fixed particle resides in the decaying turbulence. Finally, it was applied to a decaying isotropic turbulence seeded with particles of Kolmogorov to Taylor microscale sizes. The resultant flow statistics were found to be in general agreement with those of Lucci *et al.* (2010), while better overall accuracy was achieved by our simulation. As expected, the presence of finite-size particles enhances dissipation at small scales while reducing kinetic energy at large scales. The effective particle surface area and particle Stokes number dominate the dissipation rate of the system. Moreover, the scaled pivot wavenumber shows positive correlation with the dimensionless particle size, and is more sensitive for small particle sizes than large ones, with the transition particle size of $d \sim \lambda$. At a given volume fraction, the normalized pivot wavenumber is inversely propotional to the particle-to-fluid density ratio. Profiles relative to the particle surface depict strong modulation that occurs within half particle radius, and the local profiles are self similar with proper normalization.

Chapter 5

SUMMARY AND FUTURE WORK

5.1 Summary and Main Conclusions

The motivation of this dissertation is twofold: (1) to investigate the motion and hydrodynamic interactions of finite-size particles suspended in a turbulent flow, and (2) to quantify the colloid deposition mechanism in saturated soil porous media in presence of energy barrier and complex pore-scale flow geometry. These apparently different applications share the similar flow configuration, namely, interactions of a viscous moving fluid with complex solid boundaries. The two applications involve flows at very different Reynolds numbers. We have demonstrated that both problems can be handled by multiple computational methods.

The first problem was motivated by the open question concerning the impact of the presence of finite-size inertial particles on the tubulent carrier flow. For this purpose, we developed a particle-resolved simulation method based on the multiple-relaxation-time lattice Boltzmann equation (MRT-LBE) (d'Humières *et al.*, 2002). The no-slip boundary condition on the moving particles boundaries was handled by a second-order interpolated bounce-back scheme (Lallemand and Luo, 2003a). The populations at a new fluid node were constructed by equilibrium distribution with non-equilibrium correction (Caiazzo, 2008). A simple repulsive force model was utilized to prevent particle-particle overlap. The code was parallelized with MPI and was found to be computationally efficient, especially for current-day scalable computers with $\mathcal{O}(100,000)$ processors. A number of specific MPI implementation issues have been resolved and explained. Up to $51,200$ particles in 3D have been considered in our simulations, representing one of the largest systems of this kind that have been

treated in direct numerical simulations. A remarkable feature of the approach is that the computational overhead is rather moderate even for a large number of particles in a turbulent carrier flow. We also demonstrated a good scalability of the code.

The force and torque on a particle were computed based on summing mesoscopic momentum exchanges at the boundary links. Apart from the refill problem, the method essentially conserves the overall momentum of the system at the mesoscopic level, which ensures the correct balance of kinetic energy of the whole system and viscous dissipation.

The code was first validated by studying the settling of a single particle under gravity, yielding excellent results compared to experimental data of Mordant and Piton (2010) and simulated results of Lucci *et al.* (2010). The method was then applied to two problems. The first is the sedimentation of a random suspension at finite particle Reynolds numbers. Results on the hindered settling function and relative particle vertical velocity fluctuation are presented in terms of particulate volume fraction and particle Reynolds numbers. These results are in reasonable agreement with the results obtained by Climent and Maxey (2003) using an approximate force coupling method. Furthermore, we verified our LBM simulation concerning a single fixed particle in a decaying turbulence. Profiles of turbulent kinetic energy and dissipation rate around the particle surface are compared with those in Burton and Eaton (2005), and quantitative agreement is achieved.

We then applied the method to study a decaying turbulence seeded with finite-size particles. In the particle-free case, the flow statistics matched precisely the results obtained from the accurate pseudo-spectral method, consistent with the observation of Peng *et al.* (2010). Several particle-laden flow cases reported in Lucci *et al.* (2010) were simulated here, with qualitatively similar results. Some inconsistencies in the results of Lucci *et al.* (2010) have been noted, implying that our LBM may have better overall accuracy than their second-order finite-difference scheme with immersed boundary treatment at the particle-fluid interface. The immersed boundary method introduces local smoothing, which is not present in our LB approach. The results show

that particles of Kolmogorov to Taylor microscale sizes introduce small-scale features, enhance the dissipation rate of the system, and alter the shape of energy spectrum. The normalized pivot wavenumber depends on dimensionless particle size and this dependence has a transition at $d/\lambda \sim 1$. This implies that the pivot wavenumber depends not only on particle size, but also the relative ratio of particle size to flow dissipation range scales as well as the particle-to-fluid density ratio. At a given particulate volume fraction, the effective particle surface area and particle Stokes number play a prominent role in the dynamic evolution of overall kinetic energy, energy spectrum, and the flow dissipation rate. Profiles relative to the particle surface demonstrate high dissipation rate and low kinetic energy in the region of $1.0 < r/a_p < 1.5$, indicating strong modulation near particle surface. Also noted is the self-similarity of the profiles with proper normalization.

The second application in this work concerns the important environment impacts of colloid and colloid-facilitated contaminant transport and retention in soil porous media. Here we report preliminary results on microscopic viscous flow simulation in a three-dimensional porous channel and on the transport of sub-micron colloids in a model porous medium. We apply simultaneously two fundamentally different numerical methods, namely, the mesoscopic MRT-LBE method and the Navier-Stokes based Physalis method, to solve viscous flows in a porous channel with different levels of porosity and grain-grain contact. For a porous channel with one fixed spherical grain, the two methods yielded identical velocity profiles and mean flow statistics, force and torques on the grain. When two grains are introduced with both grain-grain and grain-channel walls contact points, a reasonable inter-comparison is also achieved.

As the numbers of grains and contact points are increased, it appears that the mesoscopic LBM approach is superior to the hybrid macroscopic approach. The numerical implementation of the no-slip boundary condition on grain surface is simpler in LBM, and the results of the simulated flow are more accurate near the contact points. In LBM, the calculation of all fluid-surface interaction forces are straightforward and the overall integral force balance was shown to be better satisfied. On the other hand,

the Physalis method requires iterations to match the analytical Stokes flow solutions on the surfaces of all particles to the numerical solutions slightly away from the particle surfaces. The iteration converges more slowly as the numbers of particles and contact points increase. In this sense, Physalis is not an ideal method for a system with a large number of particles. Parallel implementation for Physalis is also a problem. It may also be possible that our Physalis code could be further improved to reach the similar consistency and accuracy as LBM.

Transport and deposition of colloids were simulated by Lagrangian tracking, under a given solution ionic strength and physicochemical setting. Given the high energy barriers (above $3,000kT$) considered in our simulations, no deposition at the primary energy minimum was found, but depositions at the secondary energy minimum (SEM) were demonstrated. The local hydrodynamic retardation appears to reduce the ability for colloids to move into the SEM well, but does not prevent this to occur. Visualizations of colloid trajectories within thin slices show different levels of complexity depending on the local porosity, flow convergence, and contact points. The trajectories are quasi-two-dimensional when the local porosity is high. A close examination of colloid motion near the surface clearly shows the effect of local hydrodynamic interaction in delaying the approach of a colloid to a collector surface due to van der Waals attraction. After the colloids being captured by the SEM well, they may exhibit an quasi-periodic motion if the local hydrodynamic interaction is not considered, due to a relative weak drag force. The period of such oscillation can be predicted in terms of particle inertia and directional change of DLVO force near SEM, based on a simple mass-spring oscillator model. Hydrodynamic interaction appears to introduce high enough dissipation to eliminate such quasi-periodic motion. It was shown that a very small time step size is needed when a colloid is close to the grain surface to correctly account for the rapid change in DLVO force and the local hydrodynamic retardation effect.

We wish to point out that both the results from this study and the computational approach have contributed to quite a few journal papers and follow-up studies,

including Wang *et al.* (2013), Gao *et al.* (2013), Qiu *et al.* (2012), Gao *et al.* (2010), Wang *et al.* (2009), and Gao *et al.* (2008). The full potential of the LB approach for viscous flows laden with solid particles will be better realized as petascale computers are becoming more readily available.

5.2 Future Work

First, with regard to the particle-laden turbulence, we have so far presented some preliminary results using our particle-resolved simulations. A thorough analysis on the statistics of the dispersed phase and the carrier fluid phase would be the next step, if the resluts are to be compared with those of single-phase flows or results of particle-laden turbulence using the point-particle method. The statistical data of interest could include, for example, probability density functions of local velocity, local velocity-gradient, local dissipation rate, and local vorticity. The radial distribution function and collision rates of solid particles may also be studied. Towards this end, the numerical method will be critically examined in order to improve the representation of short-range particle-particle interaction. Other fundamental numerical issues related to moving particles such as force oscillations and the refill problem also require further research. Due to the multiscale nature of the particle-laden turbulent flow problem, it requires the state-of-the-art computers to include all relevant scales into the simulations with realistic physical parameters. Multiple-dimensional domain decomposition, as was already undertaken in Stratford and Pagonabarraga (2008) and Wang *et al.* (2013), represents an important step towards taking full advantage of the petascale computing systems.

Second, concerning the colloid transport problem and porous medium flows, it would be desirable to systematically investigate the colloid deposition mechanism under different conditions and configurations using our simulation tool. A step in this direction has been reported in Qiu *et al.* (2012) using a 2D model porous medium. Further analysis involves the effects depending on flow speed, ionic strength, random

grain packing, irregular grain shapes, suface roughness, and physical and charge heterogeneities. One future direction is to employ our simulation tool to study the depth-dependent retention profile and time-dependent effluent concentration profile (i.e., the breakthrough curve). This will allow us to compare our simulation results directly to column experimental data and those in previous computational studies. Future work would also include the inter-comparison with parallel microscopic visualization experiments being conducted by Professor Yan Jin's group at the University of Delaware (Qiu *et al.*, 2012).

REFERENCES

Aidun, C.K., Y. Lu, and E.J. Ding, 1998: Direct analysis of particulate suspensions with inertia using the discrete Boltzmann equation. *J. Fluid Mech.*, **373**, 287–311.

Apte, S.V., M. Martin, and N.A. Patankar, N.A., 2009: A numerical method for fully resolved simulation of rigid particle-flow interactions in complex flows. *J. Comput. Phys.*, **228**, 2712–2738.

Ayala, O., W.W. Grabowski, and L.-P. Wang, 2007: A hybrid approach for simulating turbulent collisions of hydrodynamically-interacting particles. *J. Comput. Phys.*, **225**, 51–73.

Bagchi, P., M.Y. Ha, and S. Balachandar, 2001: Direct numerical simulation of flow and heat transfer from a sphere in a uniform cross-flow. *J. Fluids Eng.*, **123**, 347–358.

Balachandar, S., and J.K. Eaton, 2010: Turbulent dispersed multiphase flow. *Annu. Rev. Fluid Mech.*, **42**, 111–133.

Bhatnagar, P.L., E.P. Gross, and M. Cook, 1954: A model for collision process in gases. I. Small amplitude processes in charged and neutral one-component systems. *Phys. Rev.*, **94**, 511–525.

Bradford, S.A., S.R. Yates, M. Bettahar, and J. Simunek, 2002: Physical factors affecting the transport and fate of colloids in saturated porous media. *Water Resour. Res.*, **38**, 1327–1338.

Bradford, S.A., J. Simunek, M. Bettahar, M.T. van Genuchten, and S.R.Yates, 2006: Significance of straining in colloid deposition: Evidence and implications. *Water Resour. Res.*, **42**, w12s15, doi:10.1029/2005WR004791.

Bradford, S.A., S. Torkzaban, and S.L. Walker, 2007: Coupling of physical and chemical mechanisms of colloid straining in saturated porous media. *Water Res.*, **41**, 3012–3024.

Bradford, S.A., and N. Toride, 2007: A stochastic model for colloid transport and deposition. *J. Environ. Qual.*, **36**, 1346–1356.

Brown, D.L., R. Cortez, and M.L. Minion, 2001: Accurate projection methods for the incompressible Navier-Stokes equations. *J. Comput. Phys.*, **168**, 464–499.

Burganos, V.N., C.A. Paraskeva, P.D. Christofides, and A.C. Payatakes, 1994: Motion and deposition of non-Brownian particles in upflow collectors. *Sep. Technol.*, **4**, 47–54.

Burton, T.M., and J.K. Eaton, 2005: Fully resolved simulations of particle-turbulence interaction. *J. Fluid Mech.*, **545**, 67–111.

Caiazzo, A., 2008: Analysis of lattice Boltzmann nodes initialisation in moving boundary problems. *Prog. Comput. Fluid Dyn.*, **8**, 3-10.

Chen H., S. Chen, and W.H. Matthaeus, 1992: Recovery of the Navier-Stokes equations using a lattice-gas Boltzmann method. *Phys. Rev. A.*, **45**, R5339-5342.

Cushing, R.S., and D.F. Lawler, 1998: Depth filtration: Fundamental investigation through three-dimensional trajectory analysis. *Environ. Sci. Technol.*, **32**, 3793–3801.

Climent, E., and M.R. Maxey, 2003: Numerical simulations of random suspensions at finite Reynolds numbers. *Int. J. Multiphase Flow*, **29**, 579–601.

de Jonge, L.W., C. Kjaergaard, and P. Moldrup, 2004: Colloids and colloid-facilitated transport of contaminants in soils: An introduction. *Vadose Zone J.*, **3**, 321–325.

Derjaguin, B.V., and L. Landau, 1941: Theory of the stability of strongly charged lyophobic sols i and of the adhesion of strongly charged particles in solutions of electrolytes. *Acta Physicochem (USSR)*, **14**, 633–662.

d'Humières, D., P. Lallemand, and U. Frisch, 1986: Lattice gas models for 3D hydrodynamics. *Europhys. Lett.*, **2**, 291–297.

d'Humières, D., 1992: Generalized lattice Boltzmann equations. *Rarefied Gas Dynamics: Theory and Simulations*, **159**, 450–458.

d'Humières, D., I. Ginzburg, K. Krafczyk, P. Lallemand, and L.-S. Luo, 2002: Multiple-relaxation-time lattice Boltzmann models in three dimensions. *Phil. Trans. Roy. Soc. London A.*, **360**, 437–451.

Ding, E.-J., and C.K. Aidun, 2000: The dynamics and scaling law for particles suspended in shear flow with inertia. *J. Fluid Mech.*, **423**, 317–344.

Dünweg, B., U.D. Schiller, and A.J.C. Ladd, 2007: Statistical mechanics of the fluctuating lattice Boltzmann equation. *Phys. Rev. E.*, **76**, 036704.

Eaton, J.K., 2006: Turbulence modulation by particles. *Multiphase Flow Handbook*, Taylor and Francis.

Elghobashi, S., and G. Truesdell, 1993: On the two-way interaction between homogeneous turbulence and dispersed solid particles. I: turbulence modification. *Phys. Fluids*, **5**, 1790–1801.

Elimelech, M.J., and C.R. O'Melia, 1990: Kinetics of deposition of colloidal particles in porous media. *Environ. Sci. Technol.*, **24**, 1528–1536.

Elimelech, M.J., J. Gregory, X. Jia, and R.A. Williams, 1995: *Particle Deposition and Aggregation: Measurement, Modeling,and Simulation.* Butterworth-Heinemann, Oxford.

Feng, Z.G., and E.E. Michaelides, 2004: The immersed boundary-lattice Boltzmann method for solving fluid particles interaction problems. *J. Comput. Phys.*, **195**, 602–628.

Feng, Z.G., and E.E. Michaelides, 2005: Proteus: a direct forcing method in the simulations of particulate flows. *J. Comput. Phys.*, **202**, 20–51.

Fergusona, C., de R. Husmanb, N. Altavillac, D. Deerea, and N. Ashboltc, 2003: Fate and transport of surface water pathogens in watersheds. *Crit. Rev. Environ. Sci. Technol.*, **33**, 299–361.

Franchi, A., and C.R. O'Melia, 2003: Effects of natural organic matter and solution chemistry on the deposition and reentrainment of colloids in porous media. *Environ. Sci. Technol.*, **37**, 1122–1129.

Frimmel, F.H., F. von der Kammer, and Flemming, H.-C., 2007: *Colloidal Transport in Porous Media.* Springer, New York.

Frisch, U., B. Hasslacher, and Pomeau, Y., 1986: Lattice-gas automata for the Navier-Stokes equations. *Phys. Rev. Lett.*, **56**, 1505–1508.

Gao, H., and L.-P. Wang, 2007: Towards fully resolved simulation of turbulent collision of heavy particles. CDROM Proceedings of *6th International Conference on Multiphase Flow*, Paper 713, Leipzig, Germany, July 9–17.

Gao, H., J. Han, Y. Jin, and L.-P. Wang, 2008: Modeling microscale flow and colloid transport in saturated porous media. *Int. J. Comp. Fluid Dyn.*, **22**, 493–505.

Gao, H., C.Q. Qiu, D. Fan, Y. Jin, and L.-P. Wang, 2010: Three-dimensional microscale flow simulation and colloid transport modeling in saturated soil porous media. *Comput. Math. Appl.*, **59**, 2271–2289.

Gao, H., H. Li, and L.-P. Wang, 2013: Lattice Boltzmann simulation of turbulent flow laden with finite-size particles. *Comput. Math. Appl.*, **65**, 194–210.

Ginzburg, I., F. Verhaeghe, and D. d'Humières, 2008a: Two-relaxation-time lattice Boltzmann scheme: About parametrization, velocity, pressure and mixed boundary conditions. *Commun. Comput. Phys.*, **3**, 427–478.

Ginzburg, I., F. Verhaeghe, and D. d'Humières, 2008b: Study of simple hydrodynamic solutions with the two-relaxation-times lattice Boltzmann scheme. *Commun. Comput. Phys.*, **3**, 519–581.

Glowinski, R., T.-W. Pan, T.I Hesla, and D.D. Joseph, 1999: A distributed Lagrange multiplier/fictitious domain method for particulate flows. *Int. J. Multiphase Flow*, **25**, 755–794.

Glowinski, R., T.-W. Pan, T.I. Hesla, D.D. Joseph, and J. Périaux, 2001: A fictitious domain approach to the direct numerical simulation of incompressible viscous flow passed moving rigid bodies: application to particulate flow. *J. Comput. Phys.*, **169**, 363–426.

Gore, R.A., and C.T. Crowe, 1989: Effect of particle size on modulating turbulence intensity. *Int. J. Multiphase Flow*, **15**, 279–285.

Guo, Z., C. Zheng, and B. Shi, 2002: Discrete lattice effects on the forcing term in the lattice Boltzmann method. *Phys. Rev. E.*, **65**, 046308.

Hahn, M.W., and C.R. O'Melia, 2004: Deposition and reentrainment of Brownian particles in porous media under unfavorable chemical conditions: Some concepts and applications. *Environ. Sci. Technol.*, **38**, 210–220.

Happel, J., 1958: Viscous flow in multiparticle systems: Slow motion of fluids relative to beds of spherical particles. *AIChE J.*, **4**, 197–201.

Homann, H., and J. Bec, 2010: Finite-size effects in the dynamics of Neutrally buoyant particles in turbulent flow. *J. Fluid Mech.*, **651**, 81–91.

He, X., and L.-S. Luo, 1997a: A *priori* derivation of the lattice Boltzmann equation. *Phys. Rev. E.*, **55**, 6333–6336.

He, X., and L.-S. Luo, 1997b: Theory of the lattice Boltzmann method: From the Boltzmann equation to the lattice Boltzmann equation. *Phys. Rev. E.*, **56**, 6811–6817.

Herzig, J.P., D.M. Leclerc, and P. LeGoff, 1970: flow of suspensions through porous media: Application to deep filtration. *Ind. Eng. Chem.*, **62**, 8–35.

Higuera F.J., and J. Jiménez, 1989: Boltzmann approach to lattice gas simulations. *Europhys. Lett.*, **9**, 663–668.

Higuera F.J., S. Succi, and R. Benzi, 1989: Lattice gas dynamics with enhanced collisions. *Europhys. Lett.*, **9**, 345–349.

Hogg, R., T.W. Healy, and D.W. Fuerstenau, 1966: Mutual coagulation of colloidal dispersions. *Trans. Faraday Soc.*, **62**, 1638–1651.

Homann, H., and J. Bec, 2010: Finite-size effects in the dynamics of neutrally buoyant particles in turbulent flow. *J. Fluid Mech.*, **651**, 81–91.

Hu, H., 1996: Direct simulation of solid-liquid mixtures. *Int. J. Multiphase Flow*, **22**, 335–352.

Hu, H., N.A. Patankar, and M.Y. Zhu, 2001: Direct numerical simulations of solid-liquid systems using the aribitrary Lagrangian-Eulerian technique. *J. Comput. Phys.*, **169**, 427–462.

Jin, Y. and M. Flury, 2002: Fate and transport of viruses in porous media. *Adv. Agron.*, **77**, 39–102.

Jin, G.D., G.-W. He, L.-P. Wang, and J. Zhang, 2010: Subgrid scale fluid velocity timescale seen by inertial particles in large-eddy simulation of particle-laden turbulence. *Int. J. Multiphase Flow*, **36**, 432–437.

Jin, G.D., G.-W. He, and L.-P. Wang, 2010: Large eddy simulation of collisional statistics of inertial particles in isotropic turbulence. *Phys. Fluids*, **22**, 055106.

Johnson, A.A., and T.E. Tezduyar, 1999: Advanced mesh generation and update methods for 3D flow simulations. *Comput. Mech.*, **23**, 130–143.

Johnson, W.P., and M. Tong, 2006: Observed and simulated fluid drag effects on colloid deposition in the presence of an energy barrier in a impinging jet system. *Environ. Sci. Technol.*, **40**, 5015–5021.

Johnson, W.P., X. Li, and G. Yal, 2007: Colloid retention in porous media: Mechanistic confirmation of wedging and retention in zones of flow stagnation. *Environ. Sci. Technol.*, **41**, 1279–1287.

Kim, J., and P. Moin, 1985: Application of a fractional-step method to incompressible Navier-Stokes equations. *J. Comp. Phys.*, **59**, 308–323.

Kim, S., and S.J. Karrila, 1991: *Microhydrodynamics, principles and selected applications*. Butterworth-Heinemann, Boston.

Ladd, A.J.C., 1993: Short-time motion of colloidal particles: Numerical simulation via a fluctuating lattice-Boltzmann equation. *Phys. Rev. Lett.*, **70**, 1339–1342.

Ladd, A.J.C., 1994a: Numerical simulations of particulate suspensions via a discretized Boltzmann equation. Part 1. Theoretical foundation. *J. Fluid Mech.*, **271** 285–309.

Ladd, A.J.C., 1994b: Numerical simulations of particulate suspensions via a discretized Boltzmann equation. Part 2. Numerical results. *J. Fluid Mech.*, **271** 311–339.

Lallemand, P., and L.-S. Luo, 2000: Theory of the lattice Boltzmann method: dispersion, dissipation, isotropy, Galilean invariance and stability. *Phys. Rev. E*, **61**, 6546–6562.

Lallemand, P., and L.-S. Luo, 2003a: Lattice Boltzmann method for moving boundaries. *J. Comp. Phys.*, **184**, 406–421.

Lallemand, P., and L.-S. Luo, 2003b: Theory of the lattice Boltzmann method: Acoustic and thermal properties in two and three dimensions. *Phys. Rev. E.*, **68**, 036706.

Landau, L., and E. Lifshitz, 1959: *Fluid Mechanics*. Addison-Wesley, London.

Li, X., T.D. Scheibe, and W.P. Johnson, 2004: Apparent decreases in colloid deposition rate coefficient with distance of transport under unfavorable deposition conditions: A genenral phenomenon. *Environ Sci. Technol.*, **38**, 5616–5625.

Li, X., P. Zhang, C.L. Lin, and W.P. Johnson, 2005: Role of hydrodynamic drag on microsphere deposition and re-entrainment in porous media under unfavorable conditions. *Environ Sci. Technol.*, **39**, 4012–4020.

Lucci, F., A. Ferrante, and S. Elghobashi, 2010: Modulation of isotropic turbulence by particles of Taylor length-scale size. *J. Fluid Mech.*, **650**, 5–55.

Mawdsley, J.L., R.D. Bardgett, R.J. Merry, B.F. Pain, and M.K. Theodorou, 1995: Pathogens in livestock waste, their potential for movement through soil and environmental pollution. *Appl. Soil Ecology*, **2**, 1–15.

Maxey, M.R., and J.J. Riley, 1983: Equation of motion for a small rigid sphere in a nonuniform flow. *Phys. Fluids*, **26**, 883–889.

Maxey, M.R., and B.K. Patel, 2001: Localized force representations for particles sedimenting in Stokes flows. *Int. J. Multiphase Flow*, **27**, 1603–1626.

McCarthy, J.F., and L.D. McKay, 2004: Colloid transport in the subsurface: Past, present, and future challenges. *Vadose Zone J.*, **3**, 326–337.

McGechan, M.B., and D.R. Lewis 2002: Transport of particulate and colloid-sorbed contaminants through soil. Part I: General principles. *Biosystems Eng.*, **83**, 255–273.

McLaughlin, J.B., 1989: Aerosol particle deposition in numerically simulated channel flow. *Phys. fluids A*, **1**, 1211–1224.

McNamara G.R., G. Zanetti, 1988: Use of the Boltzmann equation to simulate lattice-gas automata. *Phys. Rev. Lett*, **61**, 2332–2335.

Mei, R., L.-S. Luo, P. Lallemand, and D. d'Humières, 2006: Consistent initial conditions for lattice Boltzmann simulations. *Computers and Fluids*, **35**, 855–862.

Metreveli, G., E.-M. Kaulisch, and F.H. Frimmel, 2005: Coupling of a column system with ICP-MS for the characterisation of colloid-mediated metal(loid) transport in porous media. *Acta hydrochimica et hydrobiologica*, **33**, 337–345.

Mordant, N., and J. Pinton, 2000: Velocity measurement of a settling sphere. *Eur. Phys. J. B*, **18**, 343–352.

Naso, A., and A. Prosperetti, 2010: The interaction between a solid particle and turbulent flow. *New J. Phys.*, **12**, 033040.

Nguyen, N.Q., and A.J.C. Ladd, 2002: Lubrication corrections for lattice Boltzmann simulations of particle suspensions. *Phys. Rev. E*, **66**, 046708.

Paraskeva, C.A., V.N. Burganos, and A.C. Payatakes, 1991: Three dimensional trajectory analysis of particle deposition in constricted tubes. *Chem. Eng. Comm.*, **108**, 23–48.

Paris, A.D., and J.K. Eaton, 2001: Turbulence attenuation in a particle-laden channel flow. *Tech. Rep.*, TDS–**137**, Stanford University.

Patankar, N.A., P. Singh, D. Joseph, R. Glowinski, and T.W. Pan, 2000: A new formulation of the distributed Lagrange multiplier/fictitious domain method for particulate flows. *Int. J. Multiphase Flow*, **26**, 1509–1524.

Payatakes, A.C., R. Rajagopalan, and C. Tien, 1974a: On the use of Happel's model for filtration studies. *J. Colloid Interf. Sci.*, **49**, 321–325.

Payatakes, A.C., C. Tien, and R.M. Turian, 1974b: Trajectory calculation of particle deposition in deep bed filtration. *AIChE J.*, **20**, 889–899.

Peng, Y., W. Liao, L.-S. Luo, and L.-P. Wang, 2010: Comparison of the lattice Boltzmann and pseudo-spectral methods for decaying turbulence. Part I: Low-order statistics. *Comput. Fluids*, **39**, 568–591.

Peskin, C., 2002: The immersed boundary method. *Acta Numerica*, **11**, 479–517.

Qi, D., 1999: Lattice-Boltzmann simulations of particles in non-zero-Reynolds-number flows. *J. Fluid Mech.*, **385**, 41–62.

Qian, Y.H., D. d'Humières, and P. Lallemand, 1992: Lattice BGK models for Navier-Stokes equation. *Europhys. Lett.*, **17**, 479–484.

Qiu, C.Q., J. Han, H. Gao, L.-P. Wang, and Y. Jin, 2012: Pore-scale numerical and experimental investigation of colloid retention at the secondary energy minimum. *Vadose Zone J.*, **11**, doi:10.2136/vzj2011.0071.

Rajagopalan, R., and C. Tien, 1976: Trajectory analysis of deep-bed filtration with the sphere-in-cell porous media model. *AIChE J.*, **22**, 523–533.

Shao, X.M., T.H. Wu, and Z.S. Yu, 2012: Fully resolved numerical simulation of particle-laden turbulent flow in a horizontal channel at a low Reynolds number. *J. Fluid Mech.*, doi:10.1017/jfm.2011.533.

Shen, C., B. Li, Y. Huang, and Y. Jin, 2007: Kinetics of coupled primary- and secondary-minimum deposition of colloids under unfavorable conditions. *Environ Sci. Technol.*, **41**, 6976–6982.

Shen, C., Y. Huang, B. Li, and Y. Jin, 2008: Effects of solution chemistry on straining of colloids in porous media under unfavorable conditions. *Water Resour. Res.*, **44**, DOI: 10.1029/2007WR006580.

Singh, P., D.D. Joseph, T.I. Hesla, R. Glowinski, and T.-W. Pan, 2000: A distributed Lagrange multiplier/fictitious domain method for viscoelastic particulate flows. *J. Non-Newtonian Fluid Mech.*, **91**, 165–188.

Singh, P., T.I. Hesla, and D.D. Joseph, 2003: Distributed Lagrange multiplier method for particulate flows with collisions. *Int J. Multiphase Flow*, **3**, 495–509.

Smith, J.E., and J.M. Perdek, 2004: Assessment and management of watershed microbial contaminants. *Crit. Rev. Environ. Sci. Technol.*, **34**, 109–139.

Snyder, L.J., and W.E. Stewart, 1966: Velocity and pressure profiles for Newtonian creeping flow in regular packed beds of spheres. *AIChE J.*, **12**, 167–173.

Song, L., and M. Elimelech, 1993: Dyanmics of colloid deposition in porous media: Modeling the role of retained particles. *Colloids Surf. A*, **73**, 49–63.

Song, L., and M. Elimelech, 1994: Transient deposition of colloidal particles in heterogenous porous media. *J. Colloid Interface Sci.*, **167**, 301–313.

Spielman, L.A., 1977: Particle capture from low-speed laminar flows. *Annu. Rev. Fluid Mech.*, **9**, 297–319.

Squires, K.D., and J.K. Eaton, 1990: Particle response and turbulence modification in isotropic turbulence. *Phys. Fluids A*, **2**, 1191–1203.

Squires, K.D., and J.K. Eaton, 1991: Preferential concentration of particles by turbulence. *Phys. Fluids A*, **3**, 1169–1179.

Steffan, R.J., K.L. Sperry, M.T. Walsh, S. Vainberg, and C.W. Condee, 1999: Field-scale evaluation of in situ bioaugmentation for remediation of chlorinated solvents in groundwater. *Environ. Sci. Technol.*, **33**, 2771–2781.

Stratford, K., and I. Pagonabarraga, 2008: Parallel simulation of particle suspensions with the lattice Boltzmann method. *Comp. Math. with Applications*, **55**, 1585–1593.

Sundaram, S., and L.R. Collins, 1997: Collision Statistics in an isotropic particle-laden turbulent suspension. Part 1: Direct numerical simulations. *J. Fluid Mech.*, **335**, 75–109.

Swailes, D.C., and M.W. Reeks, 1994: Particle Deposition from a turbulent flow. I. A steady-state model for high inertia particles. *Phys. Fluids*, **6**, 3392–3403.

Takagi, S., H. Oğuz, Z. Zhang, and A. Prosperetti, 2003: Physalis: a new method for particle simulation. Part II: two-dimensional Navier-Stokes flow around cylinders. *J. Comput. Phys.*, **187**, 371–390.

Tanaka, T., and J.K. Eaton, 2008: Classification of turbulence modification by dispersed spheres using a novel dimensionless number. *Phy. Rev. Lett.*, **101**, 114502.

Ten Cate, A., J.J. Derksen, L.M. Portela, and H.E.A. van den Akker, 2004: Fully resolved simulations of colliding monodisperse spheres in forced isotropic turbulence. *J. Fluid Mech.*, **519**, 233–271.

Tenneti, S., R. Garg, and S. Subramaniam, 2011: Drag law for monodisperse gas-solid systems using particle-resolved direct numerical simulation of flow past fixed assemblies of spheres. *Int. J. Multiphase Flow*, **37**, 1072–1092.

Tufenkji, N., 2007: Colloid and Microbe Migration in Granular Environments: A Discussion of Modelling Methods. *Colloidal Transport in Porous Media*, Springer.

Tufenkji, N., and M. Elimelech, 2004: Correlation equation for predicting single-collector efficiency in physicochemical filtration in saturated porous media. *Environ. Sci. Technol.*, **38**, 529–536.

Tufenkji, N., and M. Elimelech, 2005: Breakdown of colloid filtration theory: Role of secondary energy minimum and surface charge heterogeneities. *Langmuir*, **21**, 841–852.

Uhlmann, M., 2005: An immersed boundary method with direct forcing for the simulation of particulate flows. *J. Comput. Phys.*, **209**, 448–476.

Uhlmann, M., 2008: Interface-resolved direct numerical simulation of vertical particulate channel flow in the turbulent regime. *Phys. Fluids*, **20**, 053305.

van Oss, C.J., 1994: *Interfacial forces in aqueous media.* Marcel Dekker, New York.

Verwey, E.J., and J.T.G. Overbeek, 1948: *Theory of stability of lyophobic colloids.* Elsevier, Amsterdam.

Wang, L.-P., and M.R. Maxey, 1993: Settling velocity and concentration distribution of heavy particles in homodeneous isotropic turbulence. *J. Fluid Mech.*, **256**, 27–68.

Wang, L.-P., and B. Afsharpoya, 2006: Modeling fluid flow in fuel cells using the lattice-Boltzmann approach. *Math. and Comput. in Simulation*, **72**, 242–248.

Wang, L.-P., B. Rosa, H. Gao, G.W. He, and G.D. Jin, 2009: Turbulent collision of inertial particles: point-particle based, hybrid simulations and beyond. *Int. J. Multiphase Flow*, **35**, 854–867.

Wang, L.-P., O. Ayala, H. Gao, C. Andersen, and K. Mathews, 2013: Study of forced turbulence and its modulation by finite-size solid particles using the Lattice Boltzmann approach. *Comput. Math. Appl.*, submitted.

Wu, T.H., X.M. Shao, and Z.S. Yu, 2011: Fully resolved numerical simulation of turbulent pipe flows laden with large neutrally-buoyant particles. *J. Hydrodyn.*, **23**, 21–25.

Xu, Y. and S. Subramaniam, 2010: Effect of particle clusters on carrier flow turbulence: A direct numerical simulation study. *Flow Turb. Comb.*, **85**, 735–761.

Yang, C., T. Dabros, D. Li, and J.H. Masliyah, 1998: Kinetics of particle transport to a solid surface from an impinging jet under surface and external force fields. *J. Colloid Int. Sci.*, **208**, 226–240.

Yao, K.M., J.M. Habibian, and C.R. Omelia, 1971: Water and waste water filtration : concepts and applications. *Environ. Sci. Technol.*, **5**, 1105–1112.

Yeo, K., S. Dong, E. Climent, and M.R. Maxey, 2010: Modulation of homogeneous turbulence seeded with finite size bubbles or particles. *Int. J. Multiphase Flow*, **36**, 221–233.

Yu, D., R. Mei, L.-S. Luo, and W. Shyy, 2003: Viscous flow computations with the method of lattice Boltzmann equation. *Progress in Aerospace Sci.*, **39**, 329–367.

Yu, H., L.-S. Luo, and S.S. Girimaji, 2006: LES of turbulent square jet flow using an MRT lattice Boltzmann model. *Comput. Fluids*, **35**, 957–965.

Zhang, Z., and A. Prosperetti, 2003: A method for particle simulation. *J. Appl. Mech. Trans. ASME*, **70**, 64–74.

Zhang, Z., and A. Prosperetti, 2005: A second-order method for three-dimensional particle simulation. *J. Comp. Phys.*, **210**, 292–324.

Zhou, Y., A.S. Wexler, and L.-P. Wang, 2001: Modelling turbulent collision of bidisperse inertial particles. *J. Fluid Mech.*, **433**, 77–104.

Appendix A

THE GENERAL 3D STOKES SOLUTION AROUND A SPHERICAL PARTICLE

In the process of developing our code for the hybrid Physalis method, we found quite a few typos in the Appendix of Zhang and Prosperetti (2005). Here we correct these typos and present a complete 3D Stokes flow solution around a spherical particle.

First the pressure field normalize by $\mu\nu/a^2$ can be shown to take the following general form:

$$\begin{aligned} p^* &= p_0 + \sum_{n=1}^{\infty} \left\{ \left[s^n - \frac{n(2n-1)}{2(n+1)} s^{-n-1} \right] \sum_{m=0}^{n} \left[P_{nm} \cos(m\phi) + \tilde{P}_{nm} \sin(m\phi) \right] P_n^m(\cos\theta) \right. \\ &\quad \left. - \frac{n(4n^2-1)}{n+1} s^{-n-1} \sum_{m=0}^{n} \left[\Phi_{nm} \cos(m\phi) + \tilde{\Phi}_{nm} \sin(m\phi) \right] P_n^m(\cos\theta) \right\}, \end{aligned} \tag{A.1}$$

where $s \equiv r/a$, θ is the polar angle, ϕ is the azimuthal angle, P_n^m is the associated Legendre function.

The velocity components, normalized by ν/a, should be written in spherical coordinates as:

$$\begin{aligned} u_r^* &= \sum_{n=1}^{\infty} \left\{ \left[\frac{n}{2(2n+3)} s^{n+1} - \frac{n}{4} s^{-n} + \frac{n(2n+1)}{4(2n+3)} s^{-n-2} \right] \right. \\ &\quad \times \sum_{m=0}^{n} \left[P_{nm} \cos(m\phi) + \tilde{P}_{nm} \sin(m\phi) \right] P_n^m(\cos\theta) \\ &\quad + \left[n s^{n-1} - \frac{n(2n+1)}{2} s^{-n} + \frac{n(2n-1)}{2} s^{-n-2} \right] \\ &\quad \left. \times \sum_{m=0}^{n} \left[\Phi_{nm} \cos(m\phi) + \tilde{\Phi}_{nm} \sin(m\phi) \right] P_n^m(\cos\theta) \right\}, \end{aligned} \tag{A.2}$$

$$
\begin{aligned}
u_\theta^* \;=\; & \sum_{n=1}^{\infty} \Bigg\{ \left[\frac{n+3}{2(n+1)(2n+3)} s^{n+1} + \frac{n-2}{4(n+1)} s^{-n} - \frac{n(2n+1)}{4(n+1)(2n+3)} s^{-n-2} \right] \\
& \times \sum_{m=0}^{n} \left[P_{nm} \cos(m\phi) + \tilde{P}_{nm} \sin(m\phi) \right] \frac{dP_n^m(\cos\theta)}{d\theta} \\
& + \left[s^{n-1} + \frac{(n-2)(2n+1)}{2(n+1)} s^{-n} - \frac{n(2n-1)}{2(n+1)} s^{-n-2} \right] \\
& \times \sum_{m=0}^{n} \left[\Phi_{nm} \cos(m\phi) + \tilde{\Phi}_{nm} \sin(m\phi) \right] \frac{dP_n^m(\cos\theta)}{d\theta} \\
& + (s^n - s^{-n-1}) \sum_{m=0}^{n} \left[-m X_{nm} \sin(m\phi) + m \tilde{X}_{nm} \cos(m\phi) \right] \frac{P_n^m(\cos\theta)}{\sin\theta} \Bigg\}, \qquad \text{(A.3)}
\end{aligned}
$$

$$
\begin{aligned}
u_\phi^* \;=\; & \sum_{n=1}^{\infty} \Bigg\{ \left[\frac{n+3}{2(n+1)(2n+3)} s^{n+1} + \frac{n-2}{4(n+1)} s^{-n} - \frac{n(2n+1)}{4(n+1)(2n+3)} s^{-n-2} \right] \\
& \times \sum_{m=0}^{n} \left[-m P_{nm} \sin(m\phi) + m \tilde{P}_{nm} \cos(m\phi) \right] \frac{P_n^m(\cos\theta)}{\sin\theta} \\
& + \left[s^{n-1} + \frac{(n-2)(2n+1)}{2(n+1)} s^{-n} - \frac{n(2n-1)}{2(n+1)} s^{-n-2} \right] \\
& \times \sum_{m=0}^{n} \left[-m \Phi_{nm} \sin(m\phi) + m \tilde{\Phi}_{nm} \cos(m\phi) \right] \frac{P_n^m(\cos\theta)}{\sin\theta} \\
& - (s^n - s^{-n-1}) \sum_{m=0}^{n} \left[X_{nm} \cos(m\phi) + \tilde{X}_{nm} \sin(m\phi) \right] \frac{dP_n^m(\cos\theta)}{d\theta} \Bigg\}. \qquad \text{(A.4)}
\end{aligned}
$$

The correct vorticity components, normalized by ν/a^2, are

$$
\begin{aligned}
\omega_r^* \;=\; & \sum_{n=1}^{\infty} \Big\{ n(n+1)(s^{n-1} - s^{-n-2}) \\
& \times \sum_{m=0}^{n} \left[X_{nm} \cos(m\phi) + \tilde{X}_{nm} \sin(m\phi) \right] P_n^m(\cos\theta) \Bigg\}, \qquad \text{(A.5)}
\end{aligned}
$$

$$
\begin{aligned}
\omega_\theta^* \;=\; & \sum_{n=1}^{\infty} \Bigg\{ -\left[\frac{s^n}{n+1} + \frac{2n-1}{2(n+1)} s^{-n-1}\right] \\
& \times \sum_{m=0}^{n} \left[-mP_{nm}\sin(m\phi) + m\tilde{P}_{nm}\cos(m\phi)\right] \frac{P_n^m(\cos\theta)}{\sin\theta} \\
& - \frac{4n^2-1}{n+1} s^{-n-1} \sum_{m=0}^{n} \left[-m\Phi_{nm}\sin(m\phi) + m\tilde{\Phi}_{nm}\cos(m\phi)\right] \frac{P_n^m(\cos\theta)}{\sin\theta} \\
& + \left[(n+1)s^{n-1} + ns^{-n-2}\right] \sum_{m=0}^{n} \left[X_{nm}\cos(m\phi) + \tilde{X}_{nm}\sin(m\phi)\right] \frac{dP_n^m(\cos\theta)}{d\theta} \Bigg\},
\end{aligned}
\tag{A.6}
$$

$$
\begin{aligned}
\omega_\phi^* \;=\; & \sum_{n=1}^{\infty} \Bigg\{ \left[\frac{s^n}{n+1} + \frac{2n-1}{2(n+1)} s^{-n-1}\right] \\
& \times \sum_{m=0}^{n} \left[P_{nm}\cos(m\phi) + \tilde{P}_{nm}\sin(m\phi)\right] \frac{dP_n^m(\cos\theta)}{d\theta} \\
& + \frac{4n^2-1}{n+1} s^{-n-1} \sum_{m=0}^{n} \left[\Phi_{nm}\cos(m\phi) + \tilde{\Phi}_{nm}\sin(m\phi)\right] \frac{dP_n^m(\cos\theta)}{d\theta} \\
& + \left[(n+1)s^{n-1} + ns^{-n-2}\right] \sum_{m=0}^{n} \left[-mX_{nm}\sin(m\phi) + m\tilde{X}_{nm}\cos(m\phi)\right] \frac{P_n^m(\cos\theta)}{\sin\theta} \Bigg\}.
\end{aligned}
\tag{A.7}
$$

There are a total of six sets of the expansion coefficients, P_{nm}, $\tilde{P}_{nm}$, Φ_{nm}, $\tilde{\Phi}_{nm}$, X_{nm}, and $\tilde{X}_{nm}$. These are determined by matching the numerical solution near the particle.

Appendix B

TWO-DIMENSIONAL PARTICLE SETTLING BY LBM AND PHYSALIS METHOD

In Chapter 2, we demonstrate the capability of LBM and Physalis in simulating 3D particle settling in a square channel. As a supplement, here we will show the results from its 2D counterpart using both methods. In addition, we apply Physalis to the simulation of the settling of a cluster of ten cylinder particles, in order to test the behavior of a many-particle system under small perturbations in the initial configuration of the particles.

The setup of the 2D simulation is similar to that of its 3D counterpart, and it taken to mimic Patankar *et al.* (2000) and Zhang and Prosperetti (2003). Two cylinder particles fall along the centerline of a channel under gravity. The channel has a width $20a$ and height $80a$. The particles have a radius of $a = 1mm$ and are released at distances $72a$ and $68a$ from the bottom of the domain. The lower particle is initially positioned exactly on the centerline, while the higher one departs from the centerline with a distance of $10^{-2}a$ in the $x-$direction, in order to accelerate the tumbling process. The liquid density and kinematic viscosity are $\rho_l = 1000kg/m^3$ and $\nu_l = 1.0\times10^{-6}m^2/s$, and the particle density $\rho_p = 1010kg/m^3$. Gravitational accelaration is $g = 9.8m/s^2$ in the $y-$direction. In both LBM and Physalis simulation, the particle diameter is set to $2a/\Delta x = 20$. No-slip boundary conditions are imposed on the side walls of the channel and on the particle surfaces. Neumann boundary conditions are set at top and bottom of the domain, specifying zero velocity derivatives in $y-$direction. An artificial repulsive force is adopted (Eq. (2.43)) when the two partices are in close contact, to account for the insufficient resolution for the lubrication force, and thus prevent the particles from overlapping.

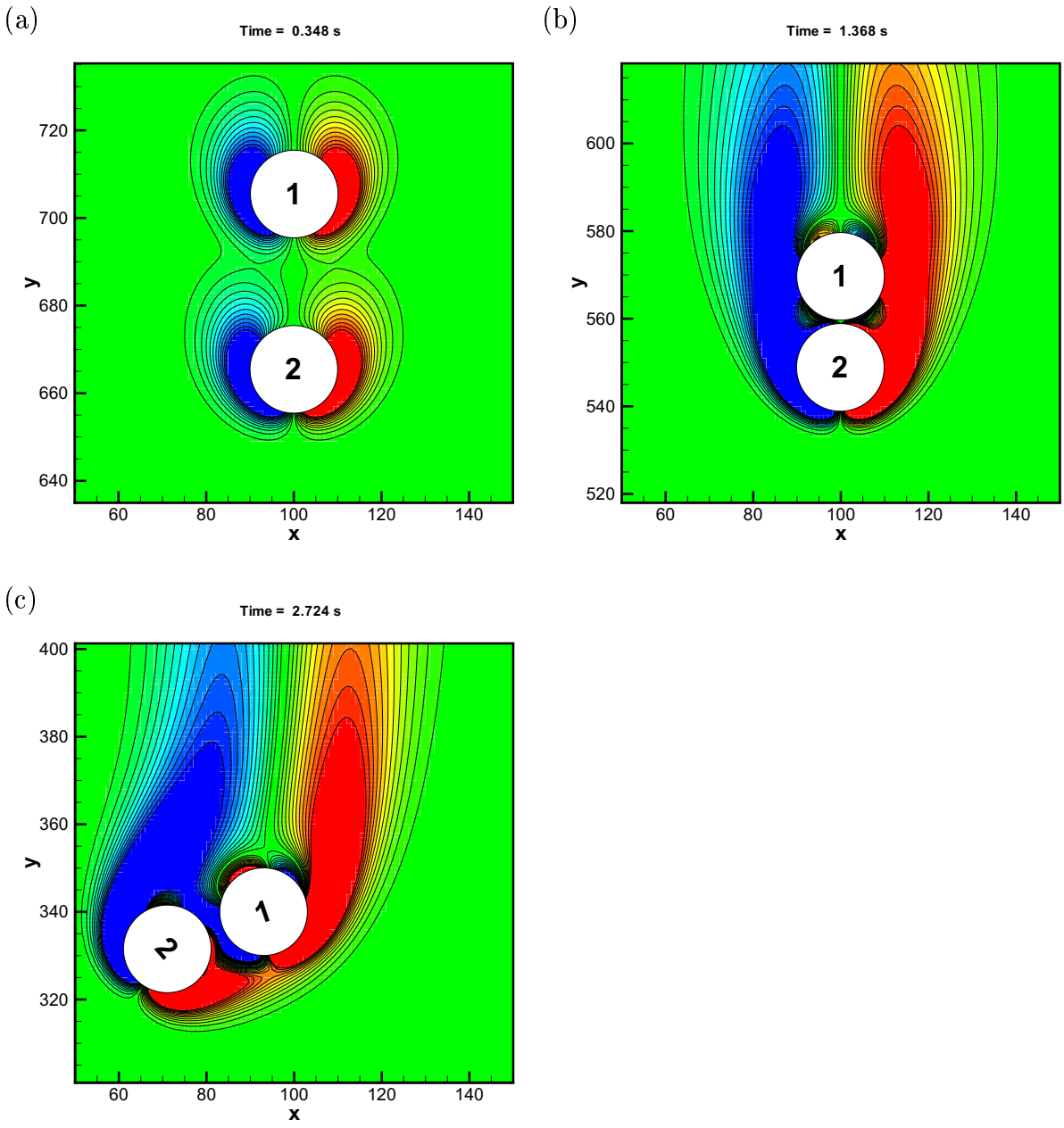

Figure B.1: Snapshots of vorticity contour and particle location of the two settling cylinder particles at times: (a) $t = 0.348s$, (b) $t = 1.368s$, and (c) $t = 2.724s$.

Figure B.1 shows the vorticity contour around the two sedimenting cylinders at different times. As in the 3D simulation, the "drafting, kissing, and tumbling" process is reproduced. The colors towards the red end denote positive vorticity, whereas the blue

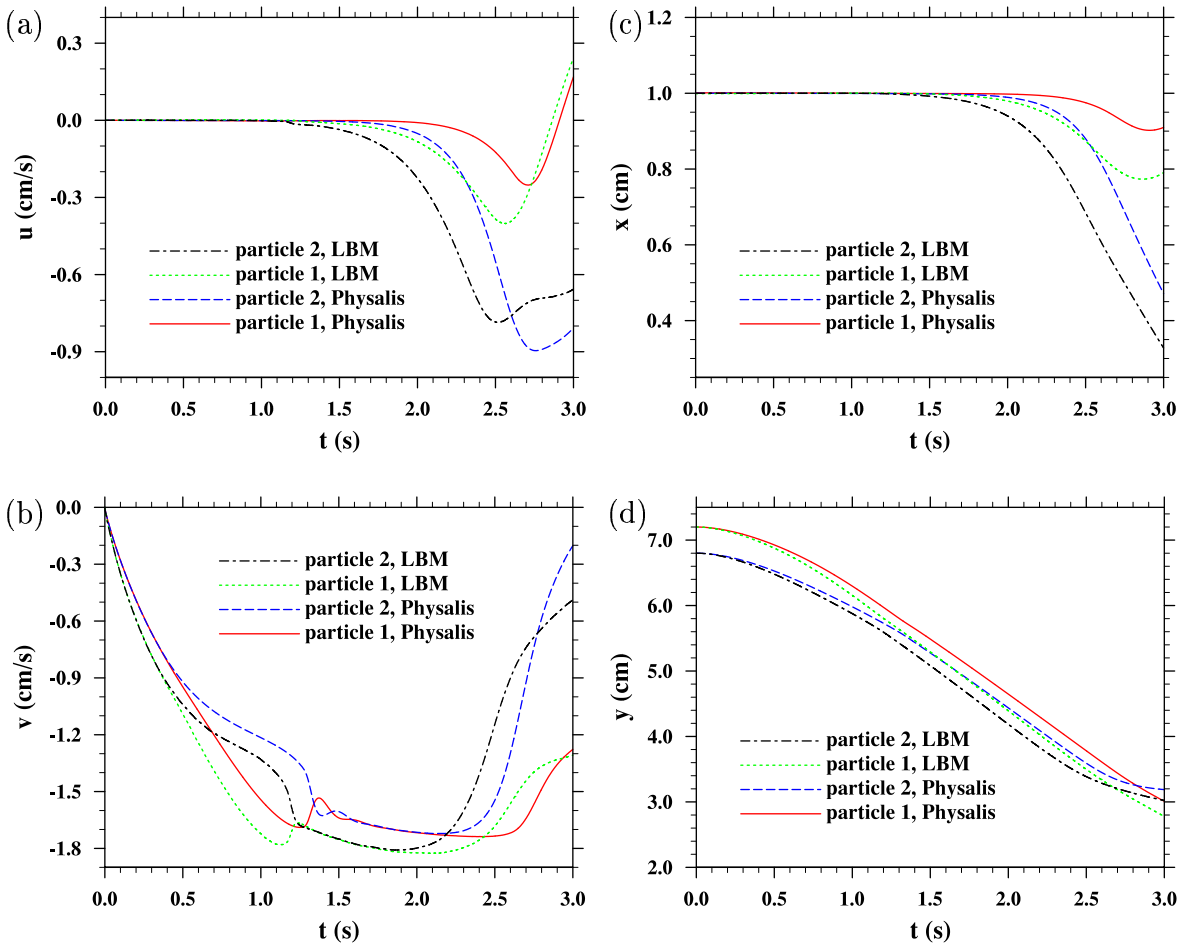

Figure B.2: Temporal evolution of particle velocity and location by both LBM and Physalis method: (a,b) velocity component in $x-$ and $y-$direction, respectively; (c,d) particle center location in in $x-$ and $y-$direction, respectively.

ones denote negative vorticity. The angular displacement of the particles is illustrated by the inclination of the particle indices. The maximum Reynolds number reached in the simulation is about 35, while the estimated value based on particle terminal velocity is about 44. This is because the simulation is performed in a finite domain with no-slip boundary conditions on both sides of the channel, so that the settling velocity can be lower than that of a free particle in an unbounded domain, hence the Reynolds number is reduced.

Figure B.2 shows the temporal evolution of the particle velocities and positions.

Again, the results from LBM and Physalis are in reasonable agreement. The discernible difference could be due to the force fluctuations present in both methods and sensitivity of the dynamic evolution of the physical configuration at early times.

Figure B.3 and Figure B.4 show another example for Physalis method. In this case the settling of a cluster of ten cylinders is illustrated by a sequence of snapshots depicting particle position and rotation. Here the channel has a width $16a$ and height $80a$. The particles have a radius of $a = 5mm$ and are initially configured in an upside down triangle-shaped symmetric array, as illustrated in Figure B.3(a) and Figure B.4(a). Vertically, the centers of the top row particles (No.1, 2, 3, 4) are set to be $4a$ apart from the top boundary of the domain. The second row (No.5, 6, 7) is shifted downward from the particle centers of the first row with another $4a$ distance, and similarly for the third and forth row. Horizontally, in each row, the center to center distance from one particle to its immediate neighborhood is $4a$ as well, with the No.1, 5, 8, 10 particle positioned $2a$, $4a$, $6a$, and $8a$ from the left wall, respectively. The liquid density and kinematic viscosity are $\rho_l = 1000kg/m^3$ and $\nu_l = 1.0 \times 10^{-4}m^2/s$, and the particle density $\rho_p = 1050kg/m^3$. The gravity is set to $g = 9.8m/s^2$ in the $y-$direction. Boundary conditions are identical to those for the simulation of two particle settling. The particle diameter is set to $2a/\Delta x = 16$. Time is normalized as $t^* = \nu t/a^2$.

The only difference between Figure B.3 and Figure B.4 lies in the initial arrangement of the particles. In Figure B.3, all the particles are completely symmetric about the centerline of the channel; whereas in Figure B.4, the No.6 particle is slightly shifted towards $x-$direction with a distance of $0.0125a$ to prompt the tumbling process. Clearly, in the former case, the particle arrangement remains symmetric about the centerline throughout the simulation, which implies an absense of bias in the numerics. In the latter case, however, symmetry is gradually lost after the occurrence of particle-particle short range interactions, as a consequence of the instability mentioned before.

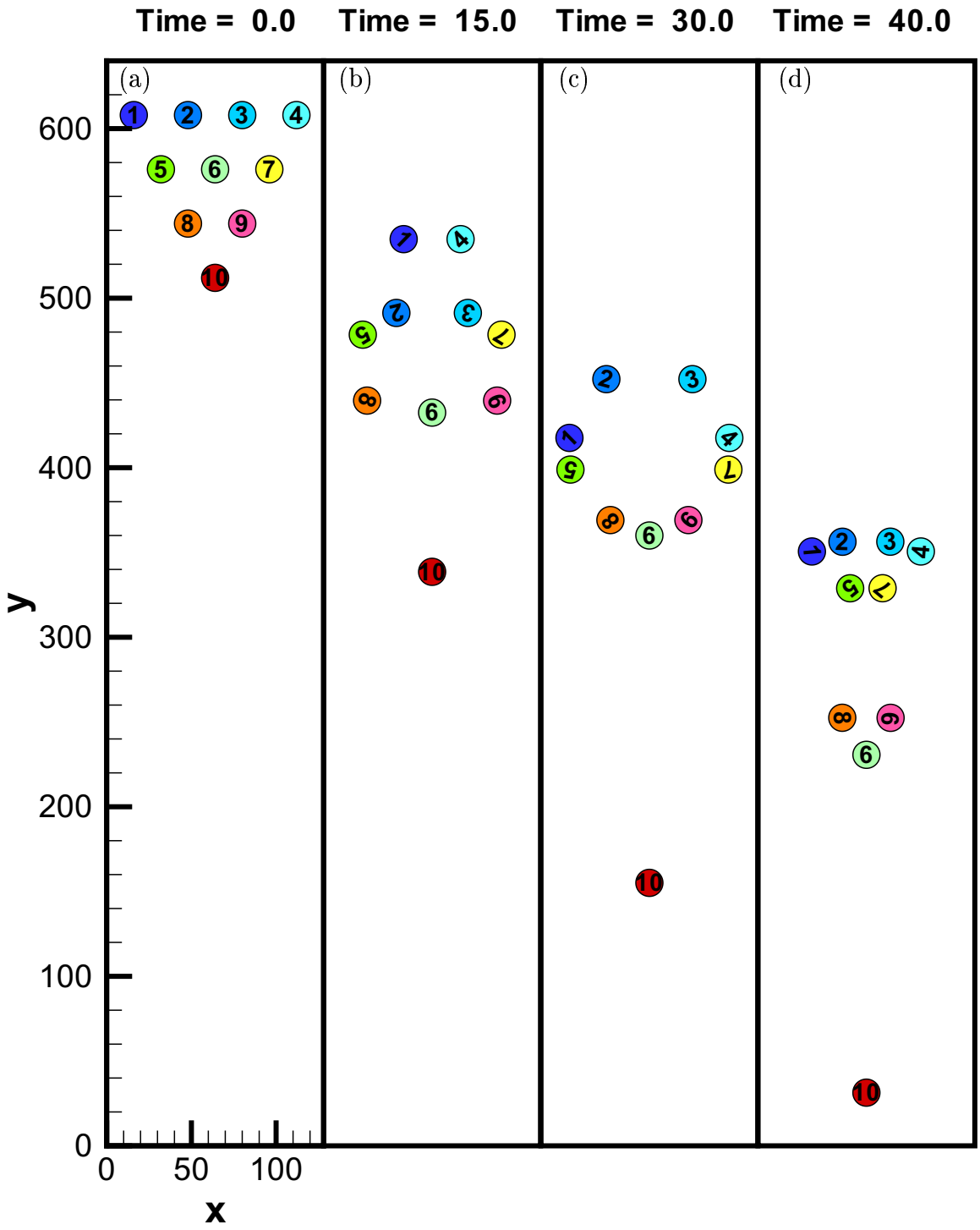

Figure B.3: Snapshots of settling of a cluster of 10 cylinder particles at times $t^* = \nu t/a^2$: (a) $t^* = 0$, (b) $t^* = 15.0$, (c) $t^* = 30.0$, and (d) $t^* = 40.0$. The initial particle arrangement is completely symmetric about the centerline of the channel.

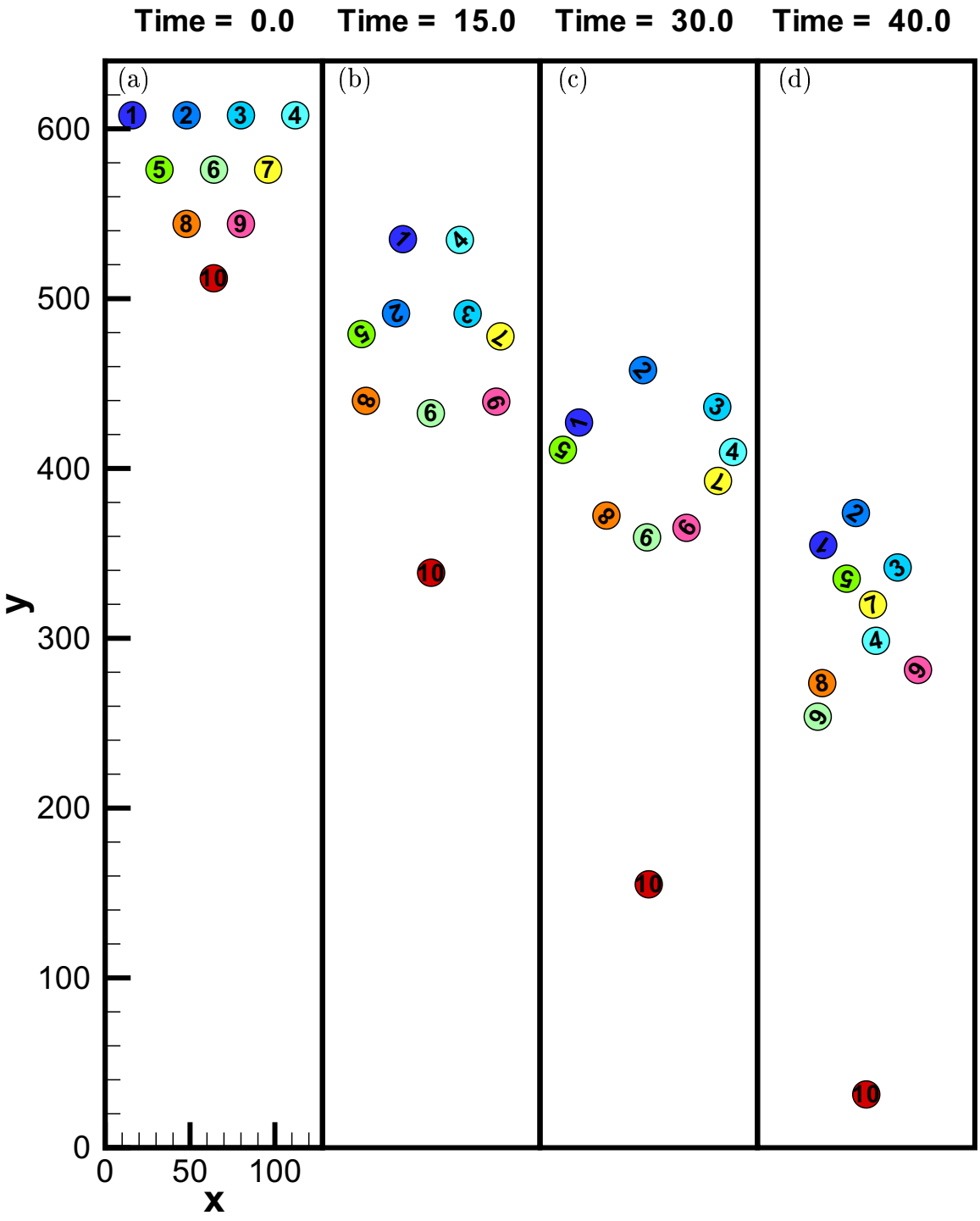

Figure B.4: Snapshots of settling of a cluster of 10 cylinder particles at times $t^* = \nu t/a^2$: (a) $t^* = 0$, (b) $t^* = 15.0$, (c) $t^* = 30.0$, and (d) $t^* = 40.0$. The initial particle arrangement is mostly symmetric about the centerline of the channel, except that the No.6 particle is shifted towards $x-$direction with a distance of $0.0125a$.

Appendix C

STRAIN RATE AND LOCAL DISSIPATION RATE CALCULATION BY LBM

The macroscopic strain rate is defined as

$$S_{ij} \equiv \frac{1}{2}\left(\frac{\partial u_i}{\partial x_j} + \frac{\partial u_j}{\partial x_i}\right) \tag{C.1}$$

and the local dissipation rate is

$$\varepsilon = 2\nu S_{ij} S_{ij}. \tag{C.2}$$

In the single-relaxation-time LBGK model, the shear stress is related to the nonequilibrium distribution as

$$2\nu S_{ij} = -\left(1 - \frac{1}{2\tau}\right)\sum_{\alpha=1}^{N}\left[f_\alpha\left(\mathbf{x},t\right) - f_\alpha^{eq}\left(\mathbf{x},t\right)\right]e_{\alpha i}e_{\alpha j} \tag{C.3}$$

where the relaxation time τ is connected with the macroscopic kinematic viscosity of the fluid

$$\nu = c_s^2\delta_t(\tau - \frac{1}{2}) = \frac{2\tau - 1}{6}. \tag{C.4}$$

The strain rate can then be computed as

$$S_{ij} = -\frac{3}{2\rho_0\tau}\sum_{\alpha=1}^{N}\left[f_\alpha\left(\mathbf{x},t\right) - f_\alpha^{eq}\left(\mathbf{x},t\right)\right]e_{\alpha i}e_{\alpha j} \tag{C.5}$$

In the MRT-LBE method, the strain rate can also be computed from the nonequilibrium moments defined as

$$m_\alpha^{(1)} \equiv m_\alpha - m_\alpha^{eq}, \qquad \alpha = 1, 2, \cdots, N \tag{C.6}$$

Yu *et al.* (2006) shows that for the D3Q19 model

$$S_{xx} \approx -\frac{1}{38\rho_0\delta_t}\left(s_1 m_1^{(1)} + 19 s_9 m_9^{(1)}\right) \tag{C.7}$$

$$S_{yy} \approx -\frac{1}{38\rho_0\delta_t}\left(s_1 m_1^{(1)} - 19 s_9 \frac{m_9^{(1)} - 3m_{11}^{(1)}}{2}\right) \tag{C.8}$$

$$S_{zz} \approx -\frac{1}{38\rho_0\delta_t}\left(s_1 m_1^{(1)} - 19 s_9 \frac{m_9^{(1)} + 3m_{11}^{(1)}}{2}\right) \tag{C.9}$$

$$S_{xy} = S_{yx} \approx -\frac{3s_9}{2\rho_0\delta_t} m_{13}^{(1)} \tag{C.10}$$

$$S_{yz} = S_{zy} \approx -\frac{3s_9}{2\rho_0\delta_t} m_{14}^{(1)} \tag{C.11}$$

$$S_{zx} = S_{xz} \approx -\frac{3s_9}{2\rho_0\delta_t} m_{15}^{(1)} \tag{C.12}$$

where

$$s_9 = \frac{2\delta_t}{6\nu/c^2 + \delta_t} = \frac{1}{\tau} \qquad \text{with} \quad c \equiv \delta_x/\delta_t.$$

Yu *et al.* (2006) noted that the diagonal components of the strain rate tensor is slightly different from those obtained from the LBGK counterpart due to the term $s_1 m_1^{(1)}$. The reason is that MRT-LBE accounts for the minor contribution related to $\nabla \cdot \mathbf{J}$, whereas it is often assumed $\nabla \cdot \mathbf{J} = 0$ in the LBGK model. Otherwise, it can be easily shown that the two methods are equilvalent.

Appendix D

ANALYTICAL REPRESENTATION OF TURBULENT KINETIC ENERGY AND DISSIPATION RATE BASED ON STOKES DISTURBANCE FLOW

The Stokes solution for creeping motion of a stream of speed U past a solid sphere of radius a can be written as

$$u_r = U\cos\theta\left(1+\frac{a^3}{2r^3}-\frac{3a}{2r}\right) \tag{D.1}$$

$$u_\theta = U\sin\theta\left(-1+\frac{a^3}{4r^3}+\frac{3a}{4r}\right) \tag{D.2}$$

$$u_\varphi = 0 \tag{D.3}$$

using spherical polar coordinates (r,θ,φ), where φ is the azimuthal angle. The kinetic energy for the disturbance flow averaged over a spherical shell is

$$\begin{aligned}\langle q^2\rangle &= \frac{1}{2}\frac{\int_0^{2\pi}\mathrm{d}\varphi\int_0^{\pi}\left(u_r^2+u_\theta^2+u_\varphi^2\right)r^2\sin\theta\,\mathrm{d}r\,\mathrm{d}\theta}{\int_0^{2\pi}\mathrm{d}\varphi\int_0^{\pi}\sin\theta r^2\,\mathrm{d}r\,\mathrm{d}\theta}\\ &= \frac{1}{2}\int_0^{\pi}\left(u_r^2+u_\theta^2+u_\varphi^2\right)\frac{\sin\theta}{2}\,\mathrm{d}\theta\\ &= \frac{1}{2}U^2\left[\frac{1}{3}\left(1+\frac{a^3}{2r^3}-\frac{3a}{2r}\right)^2+\frac{2}{3}\left(-1+\frac{a^3}{4r^3}+\frac{3a}{4r}\right)^2\right]\end{aligned} \tag{D.4}$$

Assume that for the particle-free turbulence $q_{ul}^2=\frac{1}{2}U^2$, a model for turbulent kinetic energy can be obtained

$$\frac{\langle q^2\rangle}{q_{ul}^2} = \frac{1}{3}\left(1+\frac{a^3}{2r^3}-\frac{3a}{2r}\right)^2+\frac{2}{3}\left(-1+\frac{a^3}{4r^3}+\frac{3a}{4r}\right)^2 \tag{D.5}$$

In spherical polar coordinates, the elements of the strain rate tensor for the Stokes disturbance flow take the form

$$S_{rr} = \frac{\partial u_r}{\partial r} = U\cos\theta\left(-\frac{3a^3}{2r^4} + \frac{3a}{2r^2}\right) \tag{D.6}$$

$$S_{\theta\theta} = \frac{1}{r}\frac{\partial u_\theta}{\partial \theta} + \frac{u_r}{r} = U\cos\theta\left(\frac{3a^3}{4r^4} - \frac{3a}{4r^2}\right) \tag{D.7}$$

$$S_{\varphi\varphi} = \frac{1}{r\sin\theta}\frac{\partial u_\varphi}{\partial \varphi} + \frac{u_r}{r} + \frac{u_\theta \cot\theta}{r} = U\cos\theta\left(\frac{3a^3}{4r^4} - \frac{3a}{4r^2}\right) \tag{D.8}$$

$$S_{\theta\varphi} = \frac{\sin\theta}{2r}\frac{\partial}{\partial\theta}\left(\frac{u_\varphi}{\sin\theta}\right) + \frac{1}{2r\sin\theta}\frac{\partial u_\theta}{\partial\varphi} = 0 \tag{D.9}$$

$$S_{\varphi r} = \frac{1}{2r\sin\theta}\frac{\partial u_r}{\partial\varphi} + \frac{r}{2}\frac{\partial}{\partial r}\left(\frac{u_\varphi}{r}\right) = 0 \tag{D.10}$$

$$S_{r\theta} = \frac{r}{2}\frac{\partial}{\partial r}\left(\frac{u_\theta}{r}\right) + \frac{1}{2r}\frac{\partial u_r}{\partial\theta} = -U\sin\theta\frac{3a^3}{4r^4} \tag{D.11}$$

Then the local dissipation rate is

$$\begin{aligned}\varepsilon &\equiv 2\nu S_{ij}S_{ij} \\ &= \frac{\nu U^2}{r^2}\left(\frac{3}{2}\right)^2\left\{\cos^2\theta\left[3\left(\frac{a}{r}\right)^2 - 6\left(\frac{a}{r}\right)^4 + 2\left(\frac{a}{r}\right)^6\right] + \left(\frac{a}{r}\right)^6\right\}.\end{aligned} \tag{D.12}$$

Similar to Eq. (D.4), the averaged dissipation rate can be calculated as

$$\begin{aligned}\langle\varepsilon\rangle &= \int_0^\pi \varepsilon\frac{\sin\theta}{2}\,\mathrm{d}\theta + \varepsilon_{ul} \\ &= \frac{3\nu U^2}{4r^2}\left[3\left(\frac{a}{r}\right)^2 - 6\left(\frac{a}{r}\right)^4 + 5\left(\frac{a}{r}\right)^6\right] + \varepsilon_{ul}\end{aligned} \tag{D.13}$$

where ε_{ul} is added to account for the contribution from the background turbulence. With ε_{ul} being defined as $\varepsilon_{ul} = 15\nu u'^2/\lambda^2$, where u' is the r.m.s. fluid velocity, λ is the Taylor microscale length, and assuming the slip velocity U is proportional to the r.m.s. velocity, i.e., $U = \beta u'$, we then have

$$\frac{\langle\varepsilon\rangle}{\varepsilon_{ul}} = \frac{\beta}{20}\left(\frac{\lambda}{r}\right)^2\left[3\left(\frac{a}{r}\right)^2 - 6\left(\frac{a}{r}\right)^4 + 5\left(\frac{a}{r}\right)^6\right] + 1. \tag{D.14}$$

Burton and Eaton (2005) provides the values of u' and λ in their Table 5, which allows us to verify our zeroth-order model as seen in Eq. (D.5) and Eq. (D.14). The results are shown in Figure 4.10 and Figure 4.18 in this work.